

BELLE NOTE 1486

Measurement of the decay
 $B^+ \rightarrow K^+ K^- \ell^+ \nu_\ell$ with B2BII

Matic Lubej

Ljubljana, 2018

⁶ Changelog

- ⁷ • 4. May: First submission of the note.
- ⁸ • 16. May: Added ROE validation section, Vub values to introduction

Contents

	Page
1 Introduction	1
2 Data and Monte-Carlo samples	6
2.1 Signal MC production	7
2.2 Control decay	9
3 B2BII conversion	11
3.1 Validation	12
4 Event reconstruction	13
4.1 Final state particles selection	13
4.2 Pre-selection of first B meson candidates	20
4.3 Loose neutrino reconstruction	22
4.4 Final stage optimization	26
4.5 Charge product categorization	29
4.6 Selection summary	31
5 Rest of event clean-up	32
5.1 Clusters clean-up	32
5.1.1 π^0 MVA training	33
5.1.2 γ MVA training	34
5.2 Tracks clean-up	36
5.2.1 Tracks from long-lived particles	38
5.2.2 Duplicate tracks	39
5.3 Belle clean-up	47
5.4 Clean-up results	48
5.5 ROE clean-up validation	53
6 Background suppression	57
6.1 Resonant background	57
6.2 Continuum suppression	58
6.2.1 Characteristic variables	59
6.2.2 MVA training	61

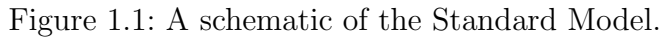
38	6.3	$B\bar{B}$ suppression	63
39	6.3.1	Boosting to uniformity	65
40	6.4	Selection optimization	66
41	6.5	Data and MC agreement	69
42	7	Signal extraction	73
43	7.1	Fit templates	74
44	7.1.1	Templates in signal fits	75
45	7.1.2	Templates in control fits	76
46	7.2	Adaptive binning algorithm	77
47	7.3	Signal MC fit results	79
48	7.3.1	Toy MC experiment	82
49	7.3.2	Toy MC linearity test	83
50	7.4	Control fit results	85
51	7.4.1	Smearing and offset parameters	85
52	7.4.2	Consistency of MVA cuts	87
53	7.4.3	Control decay branching ratio measurement	89
54	7.5	Signal fit to data	90
55	8	Systematics	91
56	8.1	Model uncertainty effects	91
57	8.2	PID efficiency correction	91
58	8.3	Bias	91

Chapter 1

Introduction

Particle physics is an established branch of physics with a rich history in theory and experiments ever since the beginning of the 20th century. So far the experimental and theoretical research have shown us hand in hand that the universe consists of particles and force carriers. Particles of matter, or elementary particles, are divided into two groups, quarks and leptons. The quarks that we know today are called u (up), d (down), s (strange), c (charm), b (bottom) and t (top). Leptons are further split into two groups; charged leptons e (electron), μ (muon), τ (tau lepton) and their corresponding neutrinos ν_e (electron neutrino), ν_μ (muon neutrino), ν_τ (tau neutrino). Particles of force are known as gauge bosons and they are γ (photon), g (gluons), W^\pm (charged weak bosons) and Z^0 (neutral weak boson). The theory also predicted the recently discovered Higgs boson (H), which is responsible for the mass of all particles. Some of the particles above also have a mirrored version of themselves, called antiparticles, which exhibit somewhat different properties as their un-mirrored versions.

Combinations of quarks such as $q_1 q_2 q_3$ (hadrons) or $q_1 \bar{q}_2$ (mesons) can make up heavier particles that we see today. Such particles are protons and neutrons, but also heavier particles which can be produced in processes involving very high energies. Such heavy particles are unstable and decay into lighter ones via forces of nature. Together with the elementary particles and force carriers, three out of four of these forces are joined in a theoretical model called the Standard Model (SM), which is shown in Figure 1.1. They are the electromagnetic, weak nuclear and strong nuclear force. Gravity is not included in the current version of the Standard Model due to its complex and weakly interacting nature. Researching such processes in large experiments enables us to study the mechanism of how elementary particles interact. By doing so we are able to learn secrets of the universe and how it all began.



One of the most important properties of the weak nuclear force is that it can change the flavor of particles. Flavor is a quantum number which is conserved for each type of quark, so changing a flavor of a quark means changing the quark itself. Such processes are forbidden for the electromagnetic and the strong nuclear force, but not for the weak one. All of the information regarding quark transitions and transition probabilities can be merged into a form of a complex matrix called the Cabibbo-Kobayashi-Maskawa (CKM) matrix [1, 2]

The CKM matrix is a unitary matrix and has only four free parameters which are not

described by theory. Its unitarity provides us with several mathematical identities, out of which the most famous one is

$$V_{ud}V_{ub}^* + V_{cd}V_{cb}^* + V_{td}V_{tb}^* = 0. \quad (1.2)$$

It can be represented by a triangle in the complex plane, called the unitarity triangle, shown in Figure 1.2. The sides and the angles of the unitarity triangle are closely connected to the free parameters of the CKM matrix. It is important to mention that all experimental measurements depend only on these four parameters, so it is possible to determine them by measuring the angles and sides of the unitarity triangle. This way the unitarity triangle offers us a unique way to test the consistency of the SM. The ultimate goal is to then join all such measurements and overconstrain the unitarity triangle to check if all the sides meet. By improving such measurements one can check whether the SM is consistent, or if there are some contributing physics processes that we do not yet understand. Such processes are commonly referred to as "new physics" (NP). The measurements of the sides and angles of the triangle are done by using different decays of which a large portion are B meson decays. Here lies another motivation for using B mesons in the analysis.



Figure 1.2: The unitarity triangle with λ , η , ρ and A (not shown) as free parameters of the CKM matrix.

In this analysis we focus on the V_{ub} CKM matrix element, which corresponds to $b \rightarrow u$ quark transitions. It has the smallest absolute value of all the CKM matrix elements and the largest error, so it offers the most room for improvement. Such quark transitions are present in charmless semi-leptonic B meson decays of the form

$$B^+ \rightarrow X_u^0 \ell^+ \nu_\ell, \quad (1.3)$$

where X_u^0 represents a charmless hadron with a u quark and ℓ is one of the charged leptons e , μ or τ . Measuring the decay rate of the B meson in such decays paves the way for the CKM matrix element determination. Decay rates are directly connected to the V_{ub} element as

$$d\Gamma \propto G_F^2 |V_{ub}|^2 |L^\mu \langle X_u | \bar{u} \gamma_\mu \frac{1}{2} (1 - \gamma_5) b | B \rangle|^2, \quad (1.4)$$

where Γ is the decay width, G_F is the Fermi coupling constant, L^μ is the leptonic current and the expression in the Dirac brackets is the hadronic current. The factor $|V_{ub}|^2$ represents the probability for the $b \rightarrow u$ quark transition. Measurement of the V_{ub} CKM matrix element can be performed in two possible ways. With the exclusive or the inclusive method, which are described below. Both methods require different experimental and theoretical techniques, so they provide largely independent determinations of $|V_{ub}|$. Currently both methods also have comparable accuracies.

In the exclusive method one studies the decays of B mesons to a specific charmless hadronic final state, such as $B \rightarrow \pi \ell \nu$. Clean determination of the V_{ub} is possible due to precise experimental measurement along with reliable theoretical calculations. However, theoretical calculations are more challenging for decays to a specific final state, since hadronization of quarks has to be taken into account. There are also two main experimental challenges in this method. One has to reduce the abundant background from $B \rightarrow X_c \ell \nu$ processes, since the $b \rightarrow c$ quark transition is much more common. The second experimental challenge is to separate the B meson decay with the specific charmless hadronic final state from other $B \rightarrow X_u \ell \nu$ decays, since it roughly populates the same regions of the phase-space as the signal decay.

In the inclusive method one studies the decays of B mesons to any charmless hadronic final state $B \rightarrow X_u \ell \nu$. In this case, the total decay rate for $b \rightarrow u \ell \nu$ can be calculated accurately, since hadronization does not have to be taken into account. The greater challenge with this method is again the experimental measurement of the total decay rate due to the $B \rightarrow X_c \ell \nu$ background. Experimental sensitivity to V_{ub} is highest where $B \rightarrow X_c \ell \nu$ decays are less dominant. Theory and experiment have to compromise and limit the V_{ub} determination to a region where the signal-to-background ratio is good. Theory takes this into account by reliably calculating the partial decay rate $\Delta\Gamma$, which is more challenging than the total decay rate. One possible and often used approach to reduce $b \rightarrow c$ background is to reject all events with K particles, or kaons, present in the final particle selection. The procedure is called a K -veto. Kaons consist of an s quark, which is mainly produced in $c \rightarrow s$ transitions. This means that if a kaon is found in the event, it is very likely that it originates from a particle with a c quark, indicating the $b \rightarrow c$ process.

If V_{ub} is determined with both these methods, the values can be compared. It turns out that consistency between these two results is only marginal, where the difference is at a level of 3σ . The current world averages [3] of the exclusive (from $B^0 \rightarrow \pi^- \ell^+ \nu$) and inclusive (GGOU collab. [4]) are

$$|V_{ub}|_{\text{excl.}} = (3.65 \pm 0.09 \pm 0.11) \times 10^{-3}, \quad (1.5)$$

$$|V_{ub}|_{\text{incl.}}^{\text{GGOU}} = (4.52 \pm 0.15 \pm_{-0.14}^{+0.11}) \times 10^{-3}, \quad (1.6)$$

where the first and the second errors are the experimental and the theoretical error, respectively. We see that inclusive measurements prefer higher values than exclusive ones. This is known as the V_{ub} puzzle. It is necessary to make further research as to

160 why this difference occurs. The reason could be an unknown experimental or theoretical
 161 error, or it is even possible that some NP contributions occur. This analysis will focus on
 162 a possible reason that could be hidden in the selection mentioned before. By performing
 163 a K -veto, one discards all events with kaons in the final state in order to suppress $b \rightarrow c$
 164 contributions. In this analysis we focus on the charged $B \rightarrow KK\ell\nu$ decay, which is
 165 very similar to the $B \rightarrow \pi\ell\nu$, except for a production of an $s\bar{s}$ quark pair, which then
 166 combines with final state quarks to form kaons, as shown in Figure 1.3. In this case,
 167 we have kaons in the final state where the B meson decayed via a $b \rightarrow u$ process. Such
 168 decays were discarded in previous V_{ub} determinations with the inclusive method, but in
 169 principle they contribute to the result and should be taken into account. The results of
 170 this analysis should help us make a step closer to solving the V_{ub} puzzle.

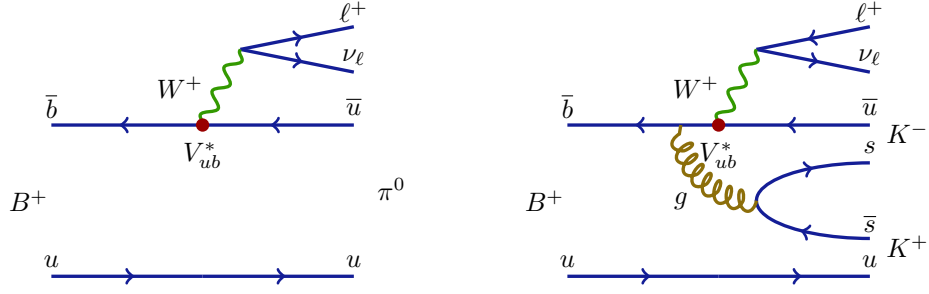


Figure 1.3: Feynman diagrams for the $B^+ \rightarrow \pi^0 \ell^+ \nu_\ell$ decay (left) and the $B^+ \rightarrow K^- K^+ \ell^+ \nu_\ell$ decay (right).

171 Specifically, we will be focusing on decays of the charged B mesons of the form $B^+ \rightarrow$
 172 $K^+ K^- \ell^+ \nu$, since it includes two charged kaons, as opposed to the case of the neutral B
 173 meson decay. The reason for this is a simpler decay chain and a higher reconstruction
 174 efficiency. All further occurrences of $B \rightarrow KK\ell\nu$ automatically imply decays of the form
 175 $B^+ \rightarrow K^+ K^- \ell^+ \nu$ and its charge conjugated counterpart.

Chapter 2

Data and Monte-Carlo samples

The Belle detector acquired a dataset of about $L_0 \approx 710 \text{ fb}^{-1}$ of integrated luminosity in its lifetime, which corresponds to about $771 \times 10^6 B\bar{B}$ meson pairs. Additionally, several streams of Monte-Carlo (MC) samples were produced, where each stream of MC corresponds to the same amount of data that was taken with the detector. The main focus of this and other similar analyses is to study a rare signal decay, which means that the amount of such decays in the existing MC is not abundant enough. In such cases, it is a common practice to produce specific samples of signal MC, where the abundance of signal decays is much larger, enabling us to study its properties in greater detail.

The following samples were used in this analysis

- data

- Belle on-resonance dataset of about L_0 integrated luminosity, measured at $\Upsilon(4S)$ resonance energy,
- Belle off-resonance dataset of about $1/10 \times L_0$ integrated luminosity, measured at 60 MeV below $\Upsilon(4S)$ resonance energy,

- signal MC, corresponding to about $400 \times L_0$,

- other MC

- generic on-resonance, 10 streams of $B\bar{B}$ (denoted as **charged** and **mixed**) and 6 streams of $q\bar{q}$ produced at $\Upsilon(4S)$ resonance energy, where each stream corresponds to L_0 ,
- generic off-resonance, 6 streams of $q\bar{q}$ produced at 60 MeV below $\Upsilon(4S)$ resonance energy, where each stream corresponds to $1/10 \times L_0$,
- $B \rightarrow X_u \ell \nu$ (denoted as **ulnu**), not included in previous MC samples, equal to an amount of $20 \times L_0$,

- other rare B meson decays (denoted as **rare**), not included in previous MC samples, equal to an amount of $50 \times L_0$.

2.1 Signal MC production

The signal MC sample of $B^+ \rightarrow K^+ K^- \ell \nu_\ell$ and the charge conjugated B^- decays was produced using the `mcproduzh` package for producing Belle MC. The package accepts a decay file, which describes the decays to be generated. The decay file used for signal MC generation was the same as for the `ulnu` sample, since it includes the decays of interest. An additional skim was applied in order to select only events of interest with at least 2 kaons and a light lepton, all coming from the same particle. This decreases the CPU consumption during the detector simulation and reconstruction.

The relevant processes which contribute to our signal decay are

- $B^+ \rightarrow a_{00} \ell^+ \nu_\ell$,
- $B^+ \rightarrow a_{20} \ell^+ \nu_\ell$,
- $B^+ \rightarrow f_2 \ell^+ \nu_\ell$,
- $B^+ \rightarrow f_0 \ell^+ \nu_\ell$,
- $B^+ \rightarrow X_u^0 \ell^+ \nu_\ell$,

where a_{00} , a_{20} , f_2 and f_0 are light unflavored states which include further decays into a $K^+ K^-$ pair, and X_u^0 represents a generic $u\bar{u}$ quark pair, which further hadronizes based on the PYTHIA quark hadronization model [5]. Figure 2.1 shows the invariant mass of the KK pair from various contributions of the MC generator. The light unflavored states have small contributions with resonant structures, while KK pairs from the X_u^0 state are more frequent and follow a wider and smoother distribution.



Figure 2.1: Invariant mass of the KK pair from various contributions of the MC generator. The light unflavored states have small contributions with resonant structure, while KK pairs from the X_u^0 state are more frequent and follow a wider and smoother distribution.

The produced signal MC sample contains decays of the form $B \rightarrow KK\ell\nu$ as well as $B \rightarrow KKX\ell\nu$, where X can be any hadron as long as it satisfies all the selection rules of the decay. It is possible to calculate the MC branching ratios for each channel by making combinations of the particles directly from the generator. Table 2.1 shows some of the most prominent channels, which are similar to our signal decay, as well as their relative fraction. It is clear that our signal decay is the most abundant one, with a relative contribution of about 28.14 %, while other channels contribute only up to about 8 % or less. Additionally, our signal decay is the cleanest, while other decays include neutral particles like π^0 , which are harder to reconstruct and suffer from decrease in efficiency due to reconstruction effects.

Channel	Ratio [%]	Channel	Ratio
$K^+ K^-$	28.14	$K^+ K^- \pi^0 \pi^0$	0.86
$K^+ K^- \pi^0$	8.94	$K^+ K^- \pi^+ \rho^-$	0.69
$K^+ \bar{K}^0 \pi^-$	8.71	$K^+ K^- \rho^+ \pi^-$	0.68
$K^0 K^- \pi^+$	8.70	$K^0 \bar{K}^0 \rho^0$	0.00
$K^+ K^- \pi^+ \pi^-$	4.15	$K \bar{K}$ pair with η	7.08
$K^0 \bar{K}^0$	3.32	$K \bar{K}$ pair with ω	5.33
$K^0 \bar{K}^0 \pi^0$	3.26	Other	14.53
$K^+ K^- \rho^0$	1.93		
$K^+ \bar{K}^0 \rho^-$	1.84		
$K^0 K^- \rho^+$	1.83		

Table 2.1: Relative branching ratios of $B \rightarrow KKX\ell\nu$ decays by channel.

We generate about 1.3×10^9 events of the form $B \rightarrow X_u \ell \nu$, which corresponds to an integrated luminosity of about $L = 400 \times L_0$, where this value was obtained by normalizing the signal MC to the amount of signal in the $B \rightarrow X_u \ell \nu$ MC sample. This amounts to a total of about 9.37×10^6 generated signal events, and to a branching ratio

$$\mathcal{B}(B^+ \rightarrow K^+ K^- \ell^+ \nu_\ell)_{MC} = 1.53 \times 10^{-5}, \quad (2.1)$$

where ℓ is e or μ . During analysis the abundant signal MC sample is scaled down to correspond to the amount of data taken with the Belle detector.

2.2 Control decay

In this analysis we are also able to define another B meson decay which occupies almost the same phase space as our signal decay. This process can be used for the monitoring of our analysis steps, which are applied to both measured and simulated data. Any kind of difference between the two might indicate our procedure to be fine-tuned to simulated data, or some other similar problem.

We define a control decay of the form

$$B^+ \rightarrow \bar{D}^0 \ell^+ \nu, \quad D^0 \rightarrow K^+ K^-,$$

which is much more abundant and, most importantly, easy to suppress, since it only populates a very narrow region in the kaon invariant mass spectrum. Due to no extra particles in the D^0 decay, the kaon invariant mass is equal to $m_{KK} \approx m_{D^0}$ up to very good precision. By excluding this narrow region we discard the majority of the

249 control candidates, while discarding only a small amount of the signal candidates. A
250 more quantitative description of suppressing control and other background candidates
251 is written in Chapter 6.

Chapter 3

B2BII conversion

The predecessor of the Belle II experiment was the Belle experiment, which finished its data taking run of 10 years at end of 2010 after collecting a dataset of about 1 ab^{-1} . That year the Belle detector was shut down and the Belle II experiment was born from the ashes, where even some of the old detector components were reused. This moved focus from Belle analyses and Belle Analysis Framework (BASF) to the construction of the Belle II detector and the development of Belle II Analysis Framework (BASF2), which was written completely from scratch, making the BASF2 software incompatible with Belle data. This resulted in gradual loss of knowledge on the maintenance and operation of the BASF software. The construction of the Belle II detector today is still an ongoing process, although first collisions were already recorded in April 2018. By the year 2025 it is foreseen that Belle II will have recorded about 50 ab^{-1} of data, which is about 50 times more than in case of Belle.

However, this is still in the distant future and in principle we need to wait for data in order to start doing analyses. On the other hand, even though the Belle experiment finished collecting data, the data itself is still relevant and has the potential for interesting physics analyses today. In the Belle II Collaboration, a task force was created in order to convert Belle data into Belle II format (B2BII). The B2BII package was developed as a part of BASF2 in order to convert data and MC of the Belle experiment and make it available within BASF2. In addition to the convenience of Belle data being processed in the more intuitive and advanced BASF2 framework, B2BII allows for estimation and validation of performances of various advanced algorithms being developed for Belle II. The conversion itself, however, is considered non-trivial. Although the conversion of the raw detector data would be possible, the reconstruction algorithms of BASF2 are optimized for Belle II and cannot be effectively applied to Belle data. To bypass this problem, reconstructed objects from PANTHER tables, a custom solution of the Belle collaboration based on C/C++ and Fortran, are mapped to their corresponding representations in BASF2. In this analysis we use the developed converter package in order to analyze Belle data with the Belle II software.

The conversion in the B2BII package is divided into three BASF2 modules. The first

283 module opens the Belle input files and reads the events into memory in the form of
284 **PANTHER** tables. This module consists predominantly of reused BASF code. The second
285 module applies various calibration factors, such as experiment and run dependent factors,
286 to the beam energy, particle identification information, error matrices of the fitted tracks,
287 etc. The module also applies some low-level cuts to reproduce removing background
288 events as done within BASF. The actual conversion and the mapping of reconstructed
289 objects is done in the last module. For more information see [6].

290 3.1 Validation

291 In order to make sure the conversion was successful and without errors, a thorough
292 validation should be performed. This is done by comparing histograms of all physical
293 quantities of the reconstructed objects on simulated and recorded events, processed with
294 BASF and BASF2. Figures X and X show some of the physical properties of the neutral
295 and charged particles, obtained with BASF and BASF2, and their difference. The plots
296 indicate that the conversion is successful and we can proceed with the analysis in the
297 framework of BASF2.

298 PLOT

299 PLOT

Chapter 4

Event reconstruction

In this chapter the procedure for event reconstruction of the B meson decay $B \rightarrow KK\ell\nu$ is shown, starting with final state particle selection and then combining them to obtain B meson candidates.

4.1 Final state particles selection

Since the neutrino escapes detection, we can only reconstruct the charged tracks in the decay, which are the two charged kaons (K) and the light lepton, which is the electron (e) or muon (μ). These are some of the particles which are commonly referred to as final state particles (FSP). Final state particles have a long lifetime and are usually the particles that we detect when they interact with the material in the detector.

It is important to limit our selection of FSP particles in order to cut down the number of particle combinations, and consequentially computation time and file sizes.

At this point of the analysis, we do not apply any intelligent cuts yet, which results in a large number of available particles and their combinations. In order to minimize this effect, we perform this part of the study on a smaller subset of the available generic MC, experiment no. 23 and 31, which correspond to an integrated luminosity of 6.273 fb^{-1} and 17.725 fb^{-1} , respectively. We chose these two experiments to get closer to the appropriate ratio of SVD1 and SVD2 data in the full Belle MC.

Leptons

Figures 4.1 and 4.2 show the impact parameters d_0 and z_0 , the momentum in $\Upsilon(4S)$ center-of-mass system (CMS), and the PID information for true and fake electrons and muons, where an extra category for true electrons/muons from the signal decay is shown.

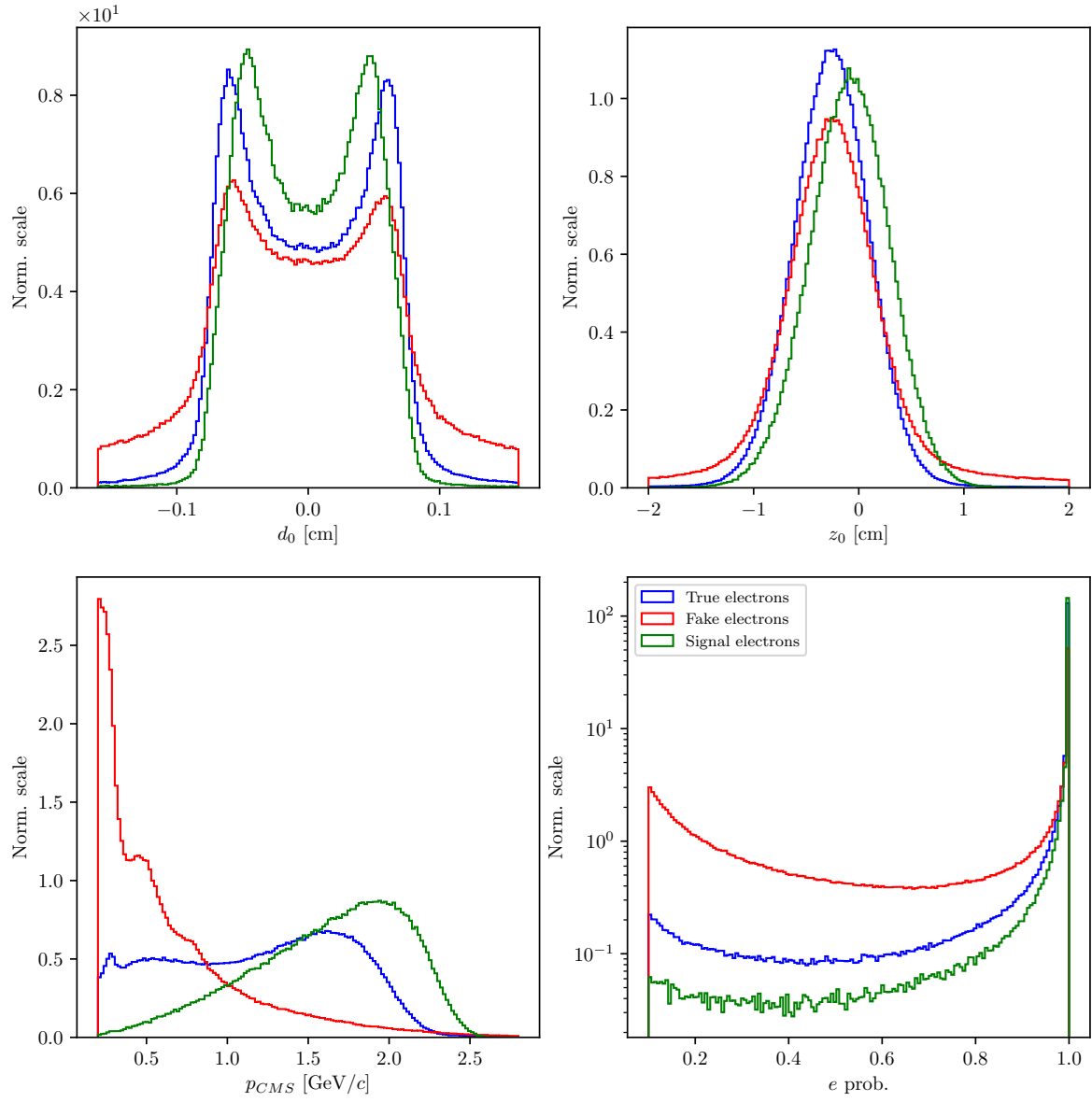


Figure 4.1: Normalized properties of true (blue), fake (red) and true electrons from signal B candidates (green).

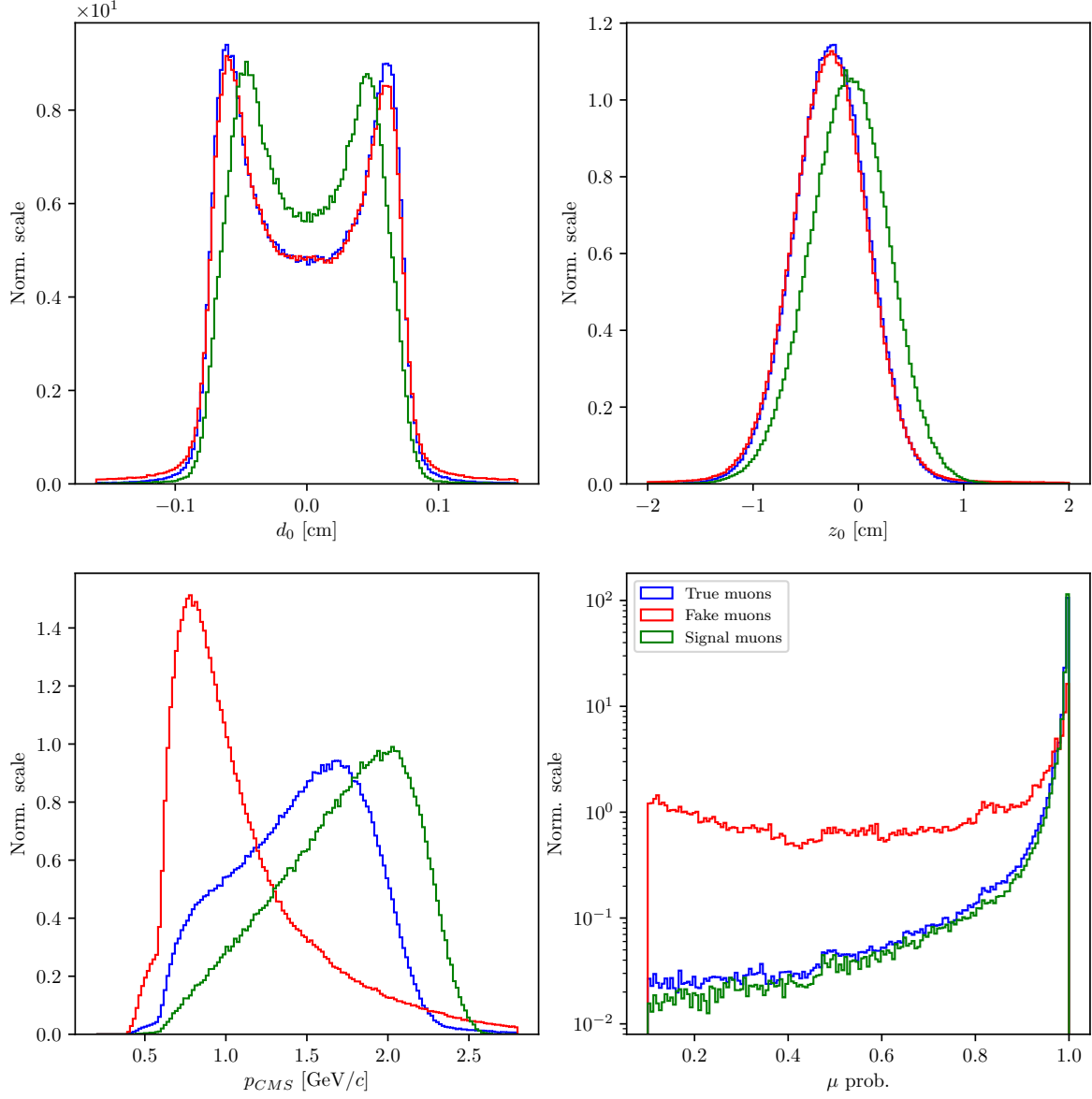


Figure 4.2: Normalized properties of true (blue), fake (red) and true muons from signal B candidates (green).

Based on these distributions, we can define a set of cuts

- $|d_0| < 0.1$ cm,
- $|z_0| < 1.5$ cm,
- $p_{CMS} \in [0.4, 2.6]$ GeV/ c for electrons,
- $p_{CMS} \in [0.6, 2.6]$ GeV/ c for muons.

After this selection we can determine the optimal PID cuts for electrons and muons, where we optimize the selection by maximizing the standard definition of *figure of merit* (FOM), defined in Eq. (4.1)

$$\text{FOM} = \sqrt{\mathcal{E}\mathcal{P}} \propto \frac{S}{\sqrt{S+B}}, \quad (4.1)$$

where the argument in the square root is the product of the efficiency (\mathcal{E}) and the purity (\mathcal{P}) function. The definitions of signal (S) and background (B) are somewhat fluid throughout the analysis and need to be defined for each FOM separately. In this section we define two representations of S and B . In FOM_1 the signal S represents correctly reconstructed final state particles, while in FOM_2 the signal S represents correctly reconstructed final state particles which also come from a correctly reconstructed B meson candidate. In both cases B represents all other particle candidates which do not satisfy the conditions of S .

The FOM plots are shown in Figures 4.3 and 4.4. The cut values are based on PID cuts used for PID efficiency calibration. The optimal value for the PID cuts is equal to the largest available value, regardless of the leptons coming from signal decays or not. The optimized PID cuts for leptons are

- e prob. > 0.9 for electrons,
- μ prob. > 0.97 for muons.

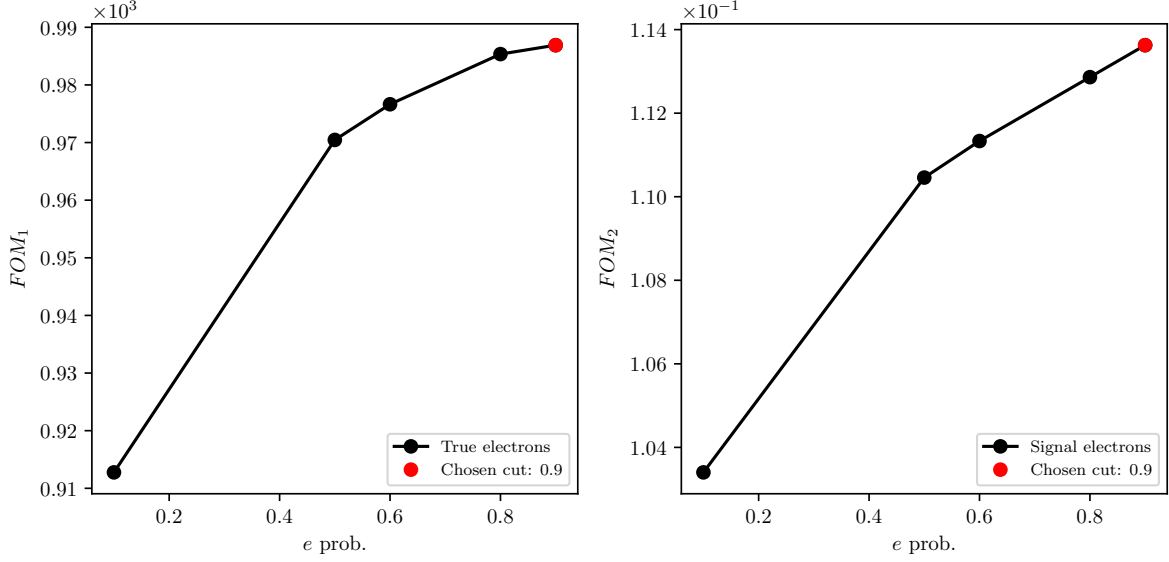


Figure 4.3: FOM optimizations of the PID probability cuts for true electrons (left) and true electrons from signal B candidates (right).

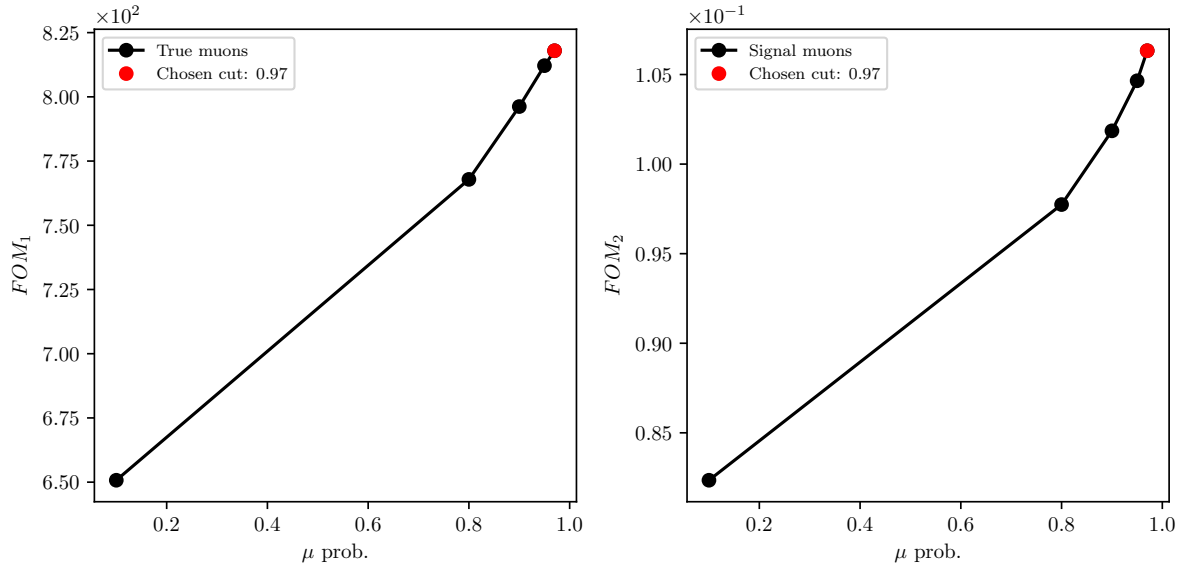


Figure 4.4: FOM optimizations of the PID probability cuts for true muons (left) and true muons from signal B candidates (right).

345 Kaons

346 We repeat the procedure for both kaons. Figure 4.5 shows the impact parameters d_0 and
 347 z_0 , the momentum in $\Upsilon(4S)$ center-of-mass system (CMS), and the PID information for
 348 true and fake kaons, where an extra category for true kaons from the signal decay is
 349 shown.

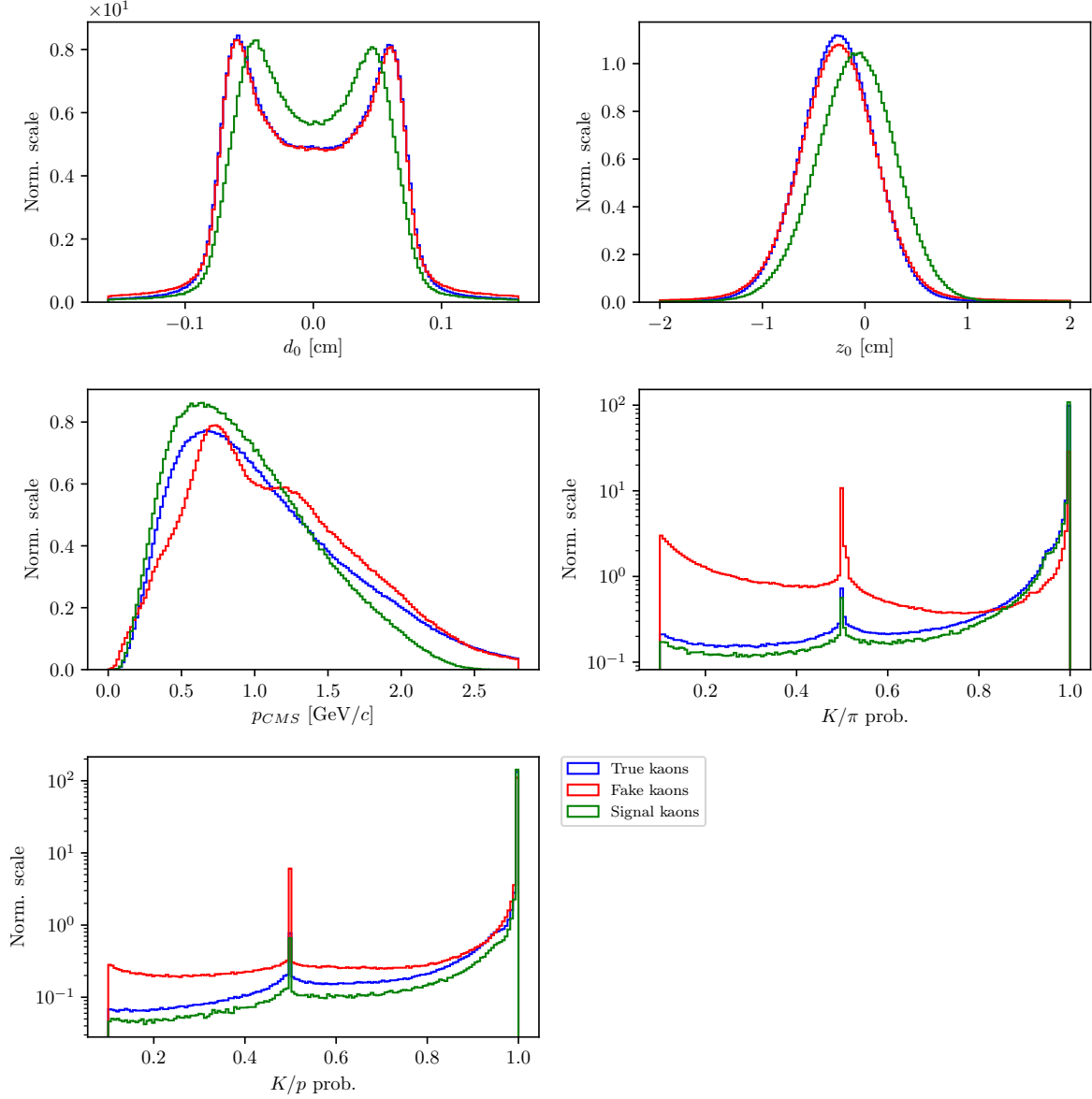


Figure 4.5: Normalized properties of true (blue), fake (red) and true kaons (green) from signal B candidates.

We define the kaon cuts in the same manner as in the case for leptons

- $|d_0| < 0.15$ cm,
- $|z_0| < 1.5$ cm,
- $p_{CMS} \in [0, 2.5]$ GeV/ c .

The PID optimization in this case is taken in two steps. First we optimize the cut on

355 K/π , and after that the K/p separation probability. Figure 4.6 shows the optimization
 356 procedure for PID cuts on kaon candidates.

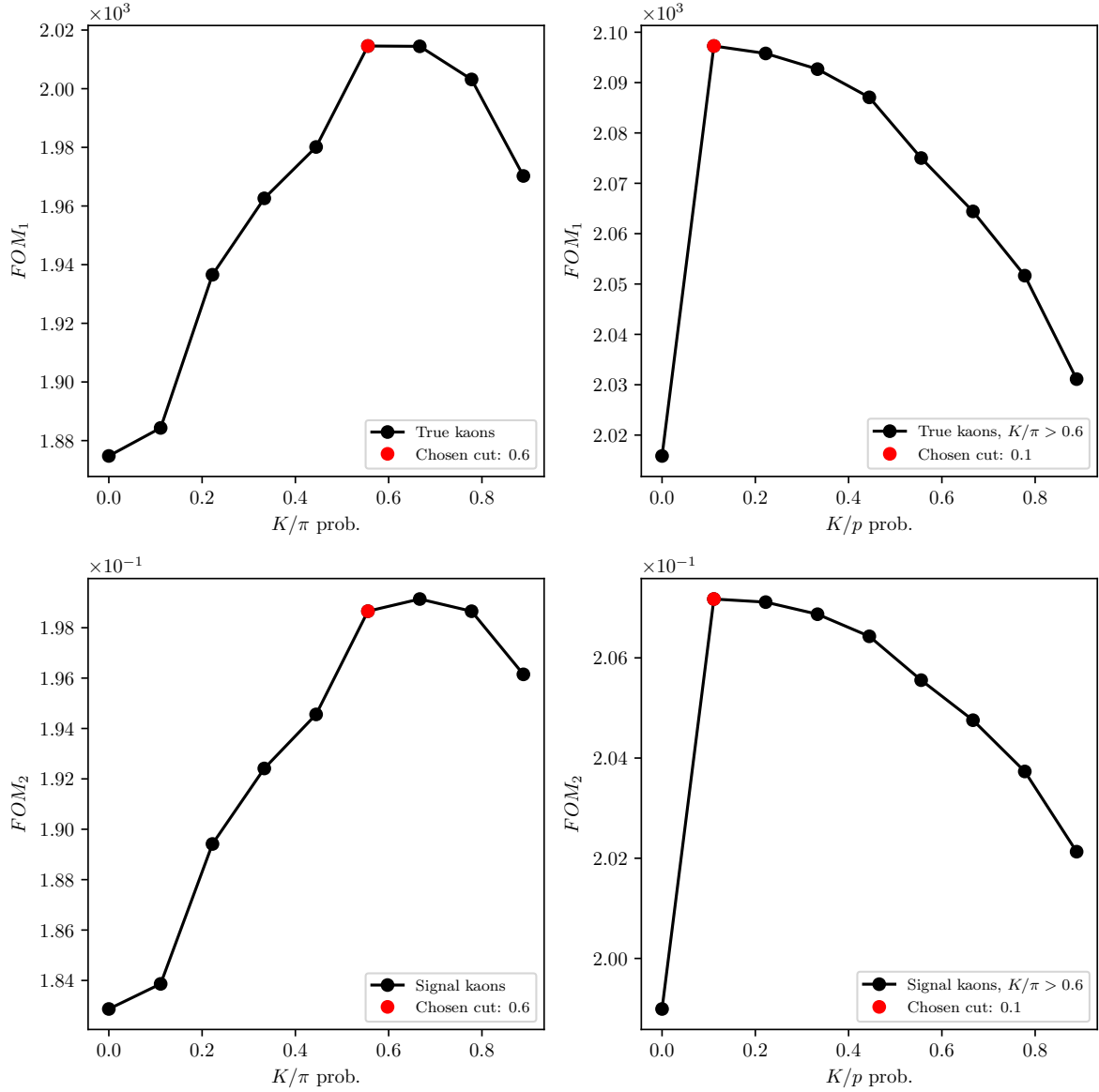


Figure 4.6: FOM optimizations of the PID probability cuts for true kaons (top) and true kaons from signal B candidates (bottom). The plots on the left show the optimization of the first step for the K/π probability cut, and the plot on the right the K/p probability cut.

357 The optimized PID cuts for kaons are

- 358 • $K/\pi > 0.6$,

- $K/p > 0.1$.

4.2 Pre-selection of first B meson candidates

In this section we use the charged particle candidates from the previous section to make particle combinations, which correspond to B meson candidates. When a B meson candidate is selected, additional features can be calculated and used for background rejection. Since we are still performing this part of the study on a smaller subset of the full available MC sample, we will perform under-optimized cuts based on the FOM optimization in order to optimize them later on the full Belle MC sample.

Since the missing neutrino escapes detection, we reconstruct the B mesons in the following two channels

$$\begin{aligned} B^+ &\rightarrow K^+ K^- e^+, \\ B^+ &\rightarrow K^+ K^- \mu^+, \end{aligned}$$

and similarly for B^- . When an arbitrary combination is obtained, we perform a vertex fit of the three tracks in order to discard combinations with a low probability of tracks coming from the same point. B mesons have a relatively long lifetime and decay along the z axis of the detector in the direction of the boost, so the vertex fit is enforced with an IPTUBE constraint, which constrains the vertex to an elongated ellipsoid along beam direction. We demand that the fit converged and apply a cut on the minimal fit probability. The fit probability for signal and background B meson candidates is shown in Figure 4.7 (left). We perform a FOM cut optimization of this variable, which is shown in Figure 4.7 (right) for the subset of the Belle MC sample. In this and in the following cases, the definition of S from Eq. (4.1) are correctly reconstructed B meson candidates with a missing neutrino which are not coming from a $b \rightarrow c$ transition.

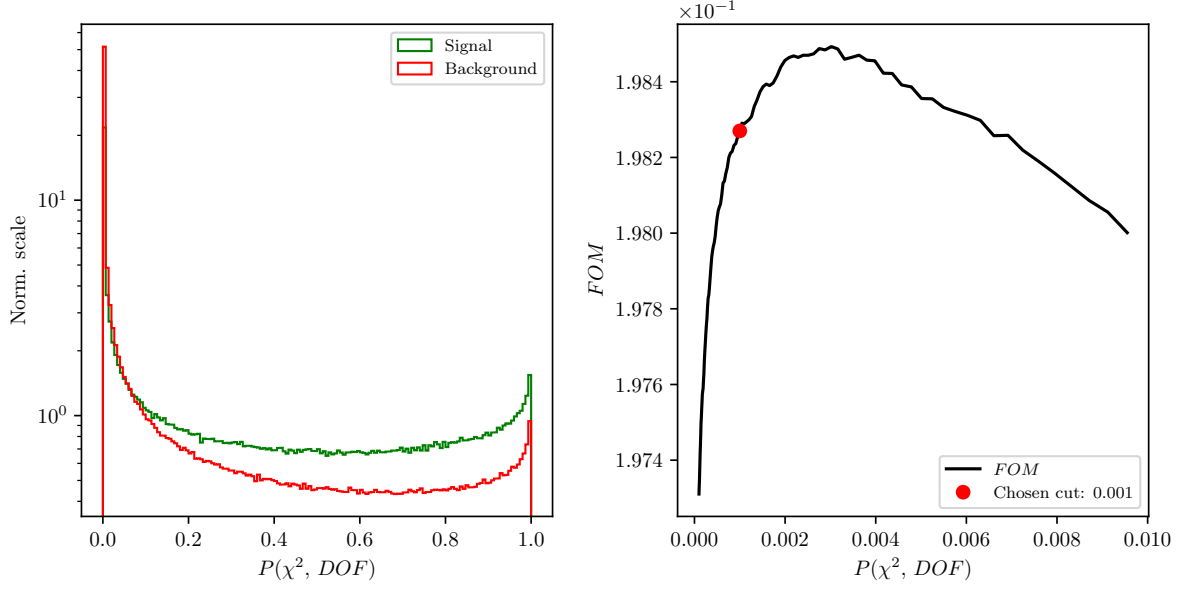


Figure 4.7: Normalized vertex fit probability distribution for signal and background B meson candidates in logarithmic scale(left) and FOM optimization of the vertex fit probability (right) for the subset of the full Belle MC sample.

The chosen pre-cut on the fit probability is

- $P(\chi^2, NDF) > 1.0 \times 10^{-3}$.

With the neutrino being the only missing particle on the reconstructed side, it is possible to determine the angle between the direction of the reconstructed B (denoted as $Y \rightarrow KK\ell$) and the nominal B , as

$$p_\nu = p_B - p_Y, \quad (4.2)$$

$$p_\nu^2 = m_\nu^2 = m_B^2 + m_Y^2 - 2E_BE_Y + 2\vec{p}_B \cdot \vec{p}_Y \approx 0, \quad (4.3)$$

$$\cos(\theta_{BY}) = \frac{2E_BE_Y - m_B^2 - m_Y^2}{2|\vec{p}_B||\vec{p}_Y|}, \quad (4.4)$$

where all the energy and momenta above are calculated in the CMS frame. The mass of the neutrino is equal to 0 to a very good precision, so we use it in Eq. (4.3). In addition, we can substitute the unknown energy and momentum magnitude, E_B and $|\vec{p}_B|$, of the B meson in Eq. (4.4), with quantities from the well known initial conditions

$$E_B = E_{CMS}/2, \quad (4.5)$$

$$|\vec{p}_B| = p_B = \sqrt{E_B^2 - m_B^2}, \quad (4.6)$$

where E_{CMS} is the total energy of the e^+e^- collision in the CMS frame and m_B is the nominal mass of the B meson.

For the correctly reconstructed candidates, this variable lies in the $[-1, 1]$ region, though only to a certain precision, due to the finite detector resolution. Background candidates, however, populate also the non-physical regions, as shown in Figure 4.8 (left).

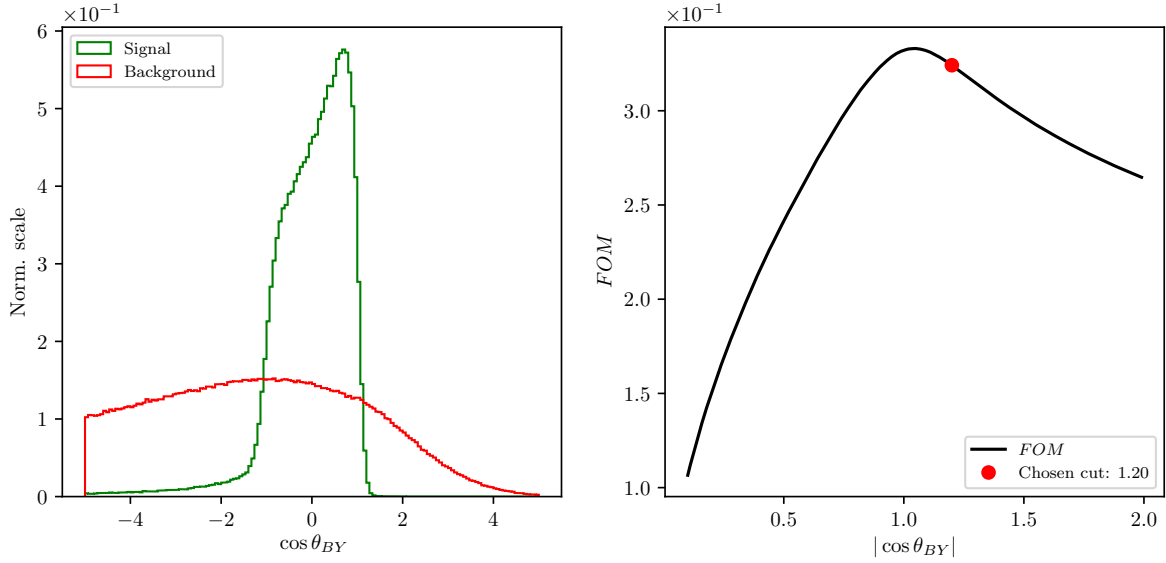


Figure 4.8: Normalized $\cos \theta_{BY}$ distribution for signal and background B meson candidates (left) and FOM optimization of the $\cos \theta_{BY}$ variable (right) for the subset of the full Belle MC.

We again impose an under-optimized cut on this variable from Figure 4.8 (right) to discard a large amount of background on this subset of the full Belle MC

- $|\cos(\theta_{BY})| < 1.20$.

4.3 Loose neutrino reconstruction

The signal-side neutrino escapes detection, so we cannot directly determine its four-momentum. However, due to the detectors geometry, which almost completely covers the full solid angle, and due to well known initial conditions of the $\Upsilon(4S)$ meson, it is possible to determine the kinematics of the missing neutrino via indirectly reconstructing

the companion B meson by summing up the four-momenta of all the FSP particles in the event which were not used in the reconstruction of the signal side B meson. This is known as the *untagged* method since we are not using any kind of tagging method to reconstruct the companion B meson. The particles used in the indirect companion B meson reconstruction are also said to belong to the *rest of the event* (ROE).

Due to the beam background in the detector, material interactions, or other processes, random tracks and clusters enter our event and get reconstructed as part of the physics process we want to study. These tracks and clusters are not interesting and further spoil the data we measure. In order to remedy this, we perform an extensive clean-up of the tracks and clusters in the ROE side before calculating the four-momentum of the missing part of the event. Here we see the motivation for the ROE clean-up, since our signal candidate reconstruction depends on tracks and clusters in the ROE side. The clean-up procedure is performed separately on tracks and clusters and uses multiple steps with multivariate analysis (MVA) algorithms in order to separate good tracks and clusters from the bad ones, which populate the ROE. Then, for each ROE object, a ROE mask is created for tracks and clusters, which narrates the use of this object in the final calculations of the ROE four-momentum. From this point on we assume the ROE to be efficiently cleansed of extra tracks and clusters. A more detailed description of the ROE clean-up can be found in Chapter 5.

The total missing four-momentum in the event can be determined as

$$p_{miss} = p_{\Upsilon(4S)} - \sum_i^{\text{Event}} (E_i, \vec{p}_i), \quad (4.7)$$

$$p_{miss} = p_{\Upsilon(4S)} - \left(p_Y - \sum_i^{\text{Rest of event}} (E_i, \vec{p}_i) \right), \quad (4.8)$$

where the summation runs over all charged and neutral particles in the defined set with

$$p_i^{\text{neutral}} = (p_i, \vec{p}_i) \quad \text{and} \quad p_i^{\text{charged}} = \left(\sqrt{m_i^2 + p_i^2}, \vec{p}_i \right), \quad (4.9)$$

where we assumed all neutral particles to be massless photons. For charged tracks in the ROE a mass hypothesis needs to be defined in order to determine the track's energy. After the ROE clean-up we make the following procedure of choosing the mass hypothesis

1. e , if e prob. $> \mu$ prob. and e prob. > 0.9 ,
2. otherwise μ , if μ prob. $> e$ prob. and μ prob. > 0.97 ,
3. otherwise K , if K/π prob. > 0.6 ,
4. otherwise π .

We define the square of the missing mass, m_{miss}^2 , which is consistent with zero, if signal-side neutrino is the only missing particle in the event, as shown in Eq. (4.11).

$$p_\nu = p_{miss} = (E_{miss}, \vec{p}_{miss}), \quad (4.10)$$

$$m_{miss}^2 = p_{miss}^2 = p_\nu^2 = m_\nu^2 \approx 0. \quad (4.11)$$

Since the detector is not perfect, the distribution of the m_{miss}^2 variable has a non-zero width. Additionally, a tail is introduced due to missing particles like neutrinos, other neutral undetected particles such as K_L^0 , or simply missing tracks due to detection failure. Figure 4.9 shows the distribution of m_{miss}^2 as defined with the missing four-momentum in Eq. (4.10). Correctly reconstructed candidates, which come from events where the other B meson decayed via a hadronic decay mode, peak at zero. If this is not the case, candidates are shifted to larger values of this variable, even if the event in question is a signal event. For this purpose we define a subset of all signal candidates, which come from events where the companion B meson decayed hadronically and all of its particles were taken into account correctly. We only allow for missing photons, since they are frequently irradiated due to brehmsstrahlung effects and they do not have such a big impact on the 4-momentum of the final candidate. We denote this subset as *perfect* signal.

Due to this fact, we impose a cut on the m_{miss}^2 variable in order to partially discard candidates with spoiled properties, even if it was in principle a correct combination of FSP particles on the signal side. The cut was chosen based on the optimization of FOM, where in this case the definition of S were perfectly reconstructed signal candidates. The chosen cut value is

$$\bullet \quad |m_{miss}^2| < 3.0 \text{ GeV}/c^2,$$

which is also under-optimized at this point due to the same reasons as in the cases above.

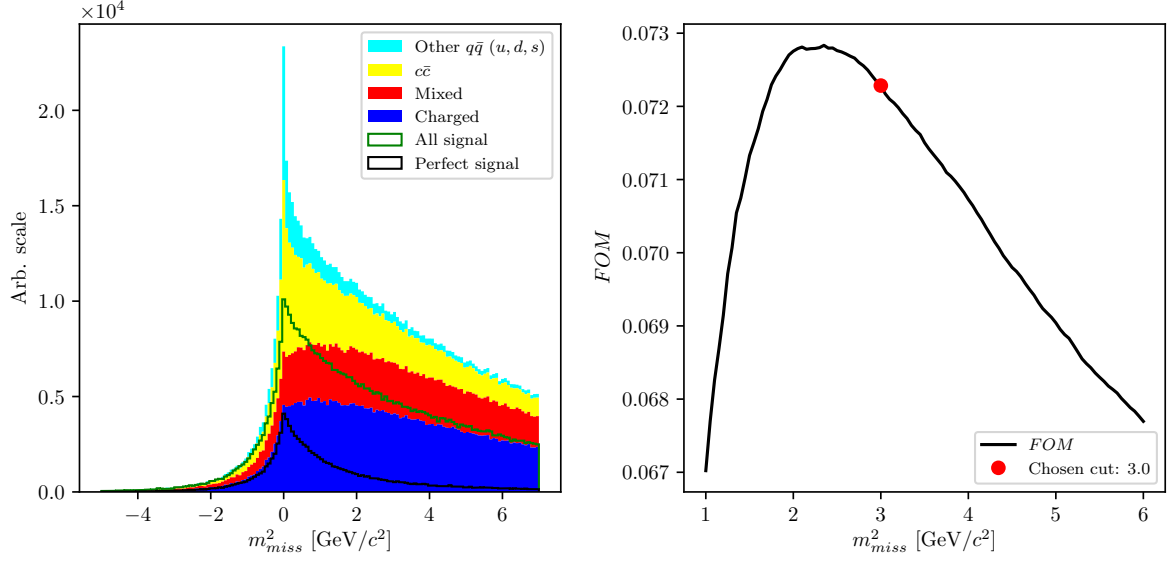


Figure 4.9: Squared missing mass distribution for signal and various types of background. All signal (green) and perfect signal (black) are scaled up equally.

The main uncertainty of the neutrino four-momentum, defined in Eq. (4.10), comes from energy uncertainty. It is a common practice to substitute the missing energy with the magnitude of the missing momentum, since the momentum resolution from the measurement is much better, thus redefining the neutrino four-momentum to

$$p_\nu = (|\vec{p}_{miss}|, \vec{p}_{miss}), \quad (4.12)$$

which fixes the neutrino mass to 0 GeV/c².

The newly defined neutrino four-momentum can be added to the four-momentum of the $Y(KK\ell)$ candidate to obtain the full B meson four-momentum and calculate the traditional M_{BC} and ΔE variables

$$\Delta E = E_B - E_{CMS}/2, \quad (4.13)$$

$$M_{BC} = \sqrt{(E_{CMS}/2)^2 - |\vec{p}|^2}. \quad (4.14)$$

Since the final fit will be performed over ΔE and M_{BC} , we define the fit region

- $M_{BC} \in [5.1, 5.295] \text{ GeV}/c^2$,
- $\Delta E \in [-1.0, 1.3] \text{ GeV}$.

Figure 4.10 shows the distributions of ΔE (left) and M_{BC} (right) for signal and major types of background after the pre-cuts. Both signal components are scaled up with

respect to the background components, but are in proper scale one to another. The effects of missing particles are clearly seen based on the shape difference between all and perfect signal.

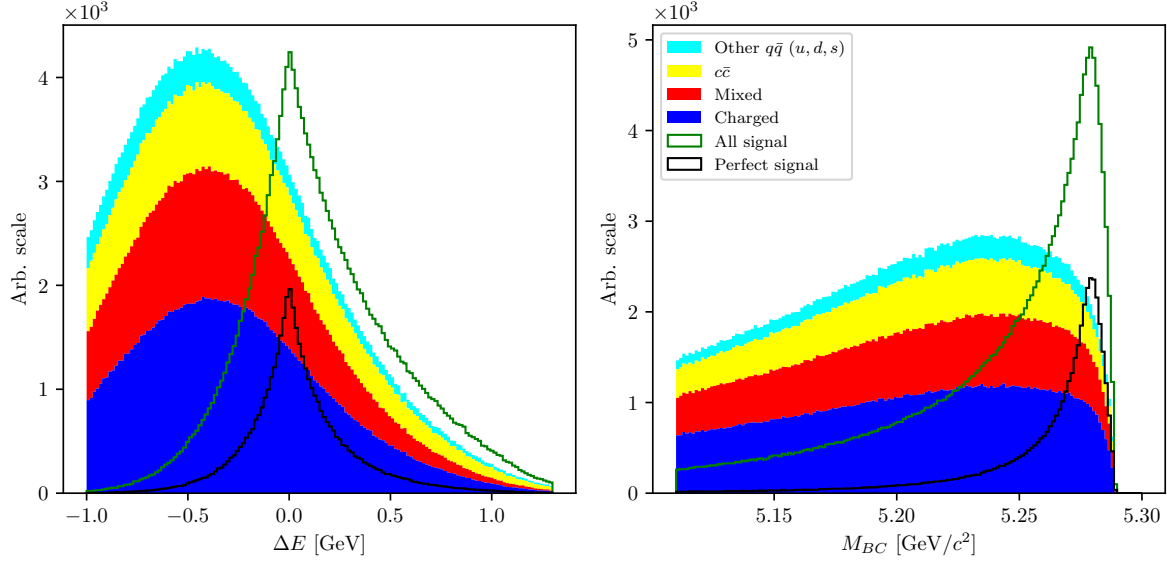


Figure 4.10: Distributions of ΔE (left) and M_{BC} (right) for signal and major types of background after the precuts. Both signal components are scaled up with respect to the background components, but are in proper scale one to another. The perfect signal has a much better resolution in both distributions, since the event is perfectly reconstructed.

4.4 Final stage optimization

With the charge particle selection and a rough selection of the B meson particles in place, we can now afford to run the reconstruction procedure over all 10 streams of the full available Belle generic MC. After obtaining the full reconstructed sample, the first task is to optimize the under-optimized cuts from the pre-selection stage. Repeating the procedure on the full sample results in the FOM shapes shown in Figure 4.11, while the optimal cut values are

- $P(\chi^2, NDF) > 6.0 \times 10^{-3}$,

- $|\cos(\theta_{BY})| < 1.05$.

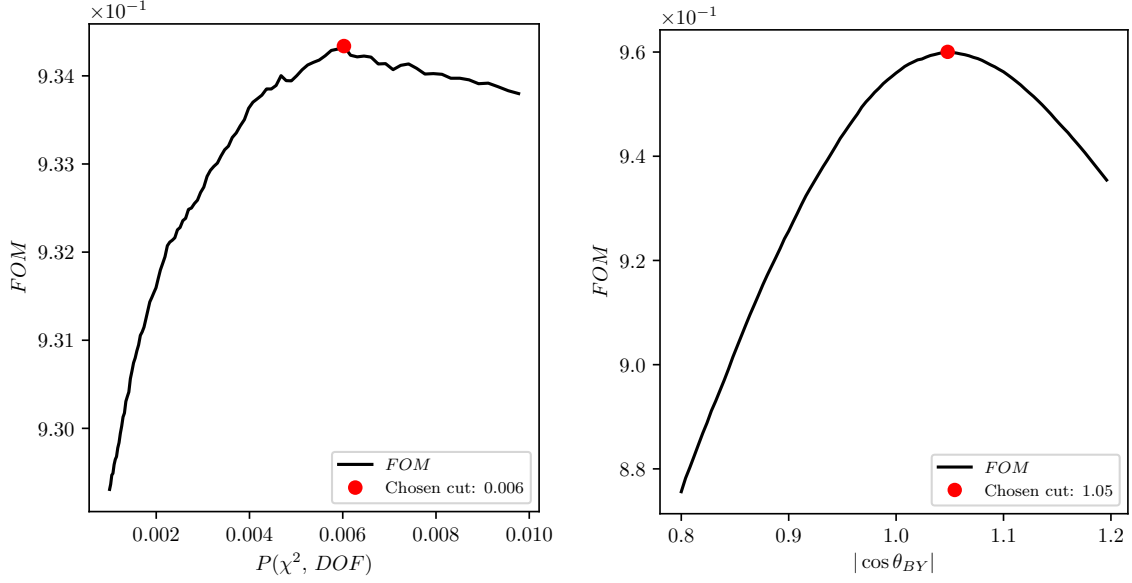


Figure 4.11: FOM optimization of the vertex fit probability (left) and the $\cos \theta_{BY}$ variable (right) for the full Belle MC sample.

With further optimizations we will be fine tuning the signal to background ratio. The most prominent and distinguishable part of our signal is the perfectly reconstructed signal. For this purpose we define a signal region in ΔE and M_{BC} , where most of our perfectly reconstructed candidates lie. We use this region for all of the following optimization steps in this chapter and also in the background suppression chapter 6. The 2D FOM optimization of the optimal ΔE and M_{BC} signal region is shown in Figure 4.12.

The signal region is defined as

- $M_{BC} > 5.271 \text{ GeV}/c^2$,
- $|\Delta E| < 0.126 \text{ GeV}$.

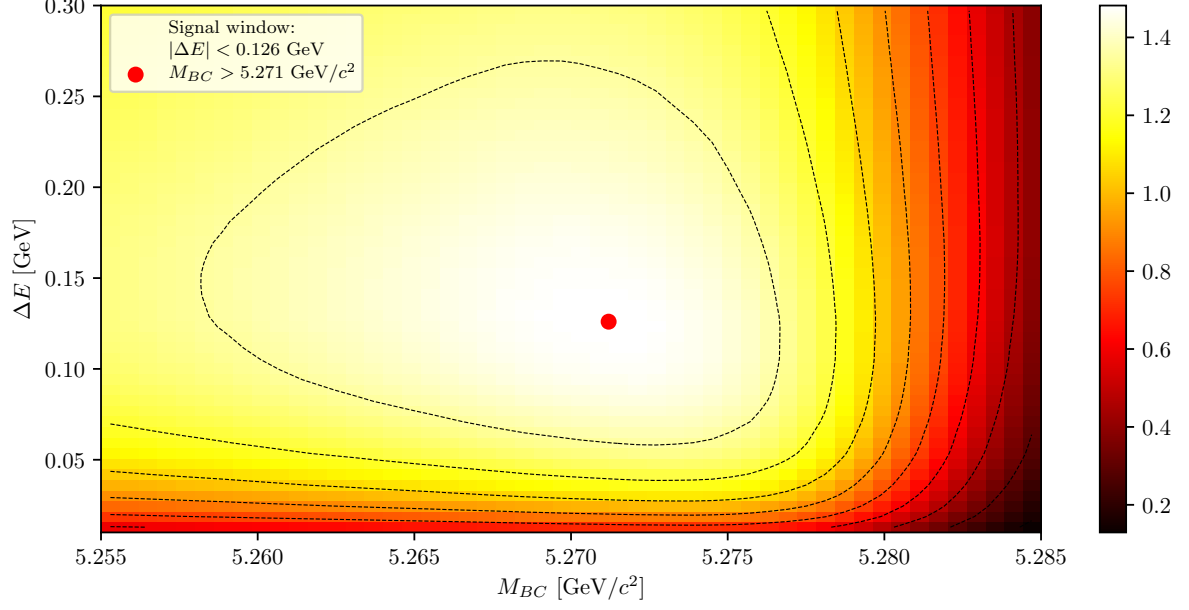


Figure 4.12: 2D FOM optimization of the signal region definition, where the signal in the optimization was represented by perfectly reconstructed candidates.

476 With the signal window defined, we can tighten the cut on m_{miss}^2 , which we intentionally
 477 left loose before the signal categorization. With the FOM optimization of perfectly
 478 reconstructed candidates inside the signal region, shown in Figure 4.13, the optimal cut
 479 on m_{miss}^2 is

480 • $|m_{miss}^2| < 0.975 \text{ GeV}/c^2$.

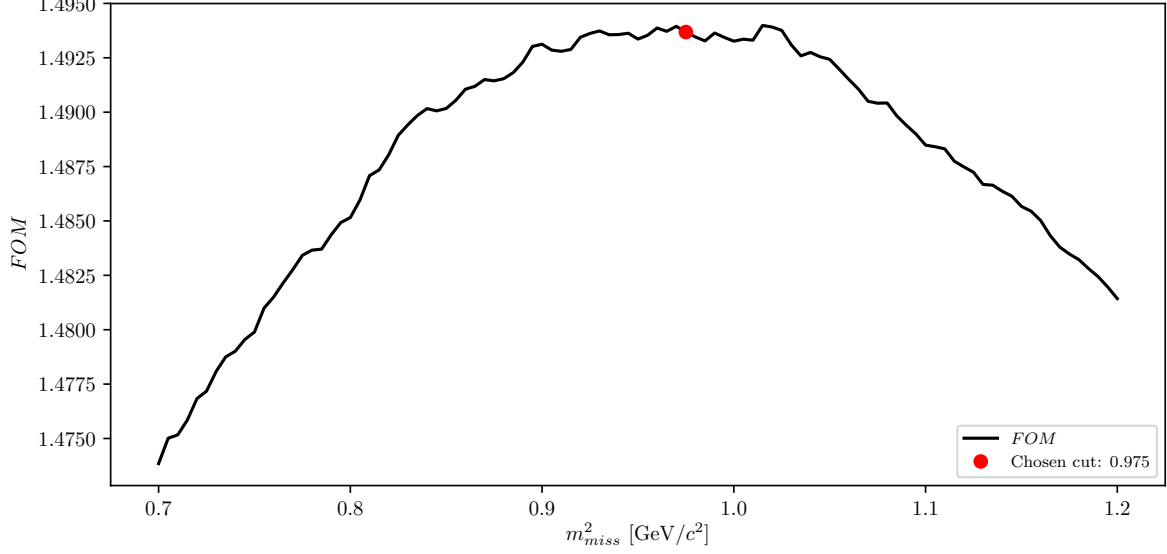


Figure 4.13: FOM optimization of the optimal m_{miss}^2 cut in the signal region.

4.5 Charge product categorization

The missing information due to an escaping neutrino in our reconstructed channel is replaced by information from the companion B meson. Since this is an untagged reconstruction, the quality of the companion B meson affects the properties of signal candidate. Perfect reconstruction of a hadronically decayed companion B meson results in pronounced peaks at $\Delta E \approx 0$, $m_{miss}^2 \approx 0$ and $M_{BC} \approx m_B$, while imperfect reconstruction due to any kind of missing particles produces tails, shift or simply a worse resolution of the mentioned distributions. These effects are undesired, since they make it harder to separate signal from background.

To remedy this, we look at the charge product of the reconstructed B meson and the ROE object. For correctly reconstructed events, this should have a value of

$$q_{B^\pm} q_{B^\mp} = -1, \quad (4.15)$$

however, this value is distributed due to missing charged particles in the reconstruction. Figure 4.14 shows various signal distributions of ΔE and M_{BC} in arbitrary (left) and normalized (right) scales, with the relative ratios of 67.86 % and 32.14 % for correct and wrong values of the charge product, respectively. We see that correctly reconstructed events represent the majority of signal and also have the best resolution in ΔE and M_{BC} , so we proceed with the analysis by imposing the cut in Eq. 4.15.

While this cut introduces a drop in the signal efficiency of about 32.14 %, it improves the resolution of our signal ΔE and M_{BC} distributions and also the signal to background ratio, where the latter changes from 0.95×10^{-3} to 1.09×10^{-3} .

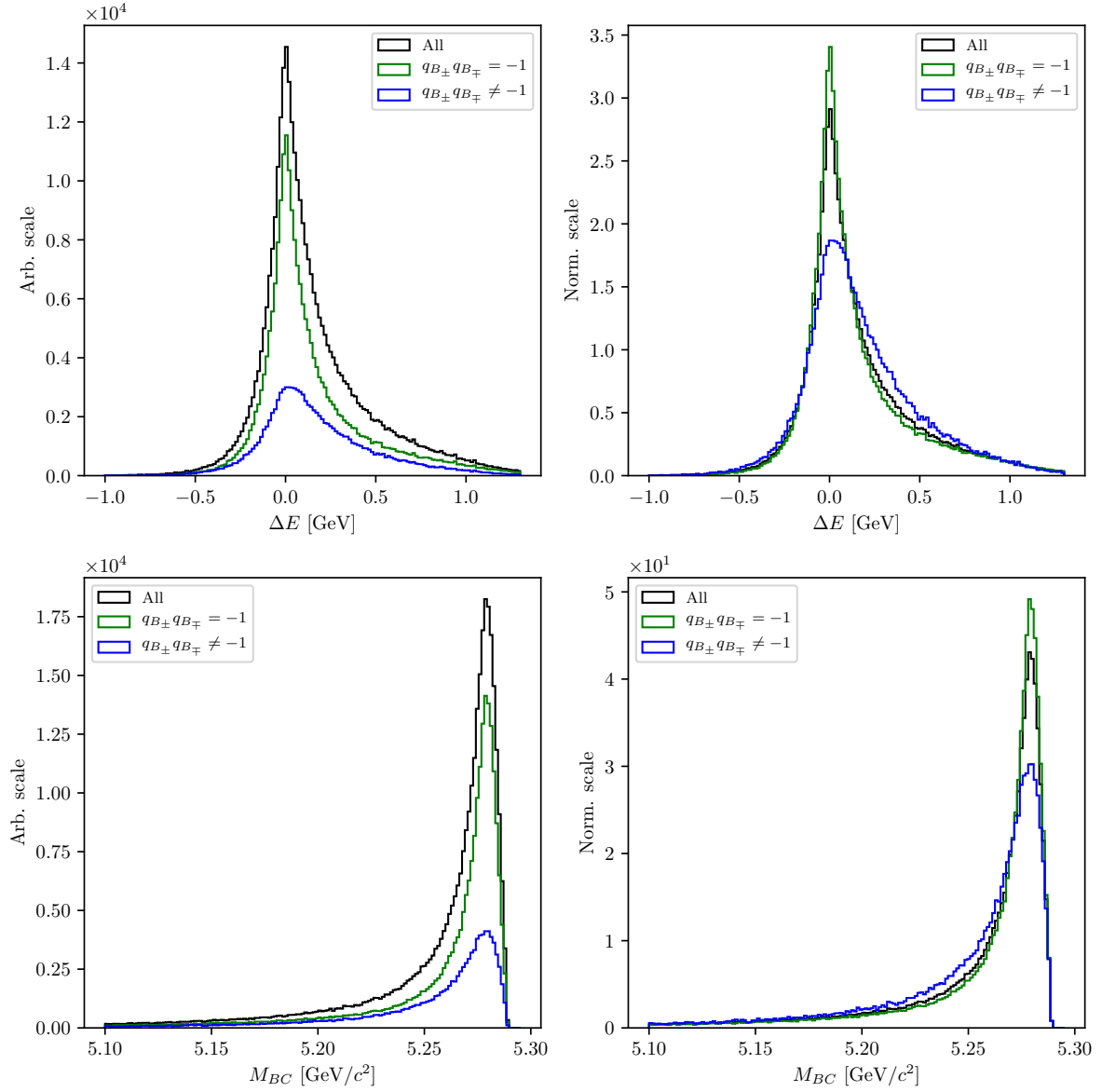


Figure 4.14: Signal distributions of ΔE and M_{BC} based on the charge product of both B mesons in the event. The plot on the left shows the distributions in an arbitrary scales, while the plot on the right shows the normalized distributions.

4.6 Selection summary

In this section one can find the full summary of all final selection cuts in the event reconstruction, from FSP particles up to the B meson.

- FSP particles:

- electrons: $|d_0| < 0.1$ cm, $|z_0| < 1, 5$ cm, $p > 0.6$ GeV/ c ,
 $p_{CMS} \in [0.4, 2.6]$ GeV/ c , $eID > 0.9$,

- muons: $|d_0| < 0.1$ cm, $|z_0| < 1, 5$ cm, $p_{CMS} \in [0.6, 2.6]$ GeV/ c ,
 $\mu ID > 0.97$,

- kaons: $|d_0| < 0.15$ cm, $|z_0| < 1, 5$ cm, $p_{CMS} < 2.5$ GeV/ c ,
 $K/\pi ID > 0.6$, $K/p ID > 0.1$,

- B meson candidates:

- standard cuts: $P(\chi^2, DOF) > 6 \times 10^{-3}$, $|\cos \theta_{BY}| < 1.05$, $|m_{miss}^2| < 0.975$ GeV/ c^2 ,

- fit region cuts: $\Delta E \in [-1.0, 1.3]$ GeV, $M_{BC} \in [5.1, 5.295]$ GeV/ c^2 ,

- signal region cuts: $|\Delta E| < 0.126$ GeV, $M_{BC} > 5.271$ GeV/ c^2 ,

- charge categorization: $q_{B^\pm} q_{B^\mp} = -1$.

Chapter 5

Rest of event clean-up

Continuing from Section 4.3, the description of the ROE clean-up process is described here.

Training the MVA classifiers follows the same recipe for all the steps in this chapter. For each step we run B meson reconstruction on Signal MC with a generic companion B meson. This way the produced weight files are less likely to be signal-side dependent and can be used also for untagged analyses of other decays. For every correctly reconstructed signal B meson we save the necessary information for each MVA step (i.e. properties of ROE clusters). Only correctly reconstructed B candidates are chosen here, to prevent leaks of information from the signal side to the ROE side.

5.1 Clusters clean-up

Photons originate from the IP region, travel to the ECL part of the detector in a straight line and produce a cluster. The direction of the photon is determined via the location of the cluster hit in the ECL and the energy of the photon is directly measured via the deposited energy. This way the four-momentum of photons is determined and used in Eq. (4.8).

Most of the photons in events with B mesons come from $\pi^0 \rightarrow \gamma\gamma$ decays. However, a lot of hits in the ECL are also created by photons coming from beam-induced background or secondary interactions with the detector material. Such photons add extra energy and momentum which spoils our measured quantities.

In the first step of the clusters clean-up we train an MVA which recognizes good π^0 candidates. The output of this classifier is then applied to photons and represents a sort of a π^0 origin probability, which is used as an additional classifier variable in the next step of the clean-up.

5.1.1 π^0 MVA training

The training dataset of π^0 candidates contains

- 183255 target candidates,
- 200000 background candidates,

where the definition of target is that both photon daughters that were used in the reconstruction of the π^0 are actual photons and real daughters of the π^0 particle. We use π^0 candidates from the converted Belle particle list and select those with invariant mass in the range of $M \in [0.10, 0.16]$ GeV. After that we perform a mass-constrained fit on all candidates, keeping only the ones for which the fit converged.

The input variables used in this MVA are

- p and p_{CMS} of π^0 and γ daughters,
- fit prob. of the mass-constrained fit, invariant mass and significance of mass before and after the fit,
- angle between the photon daughters in the CMS frame,
- cluster quantities for each daughter photon
 - E_9/E_{25} ,
 - theta angle,
 - number of hit cells in the ECL,
 - highest energy in cell,
 - energy error,
 - distance to closest track at ECL radius.

The classifier output variable is shown in Figure 5.1.

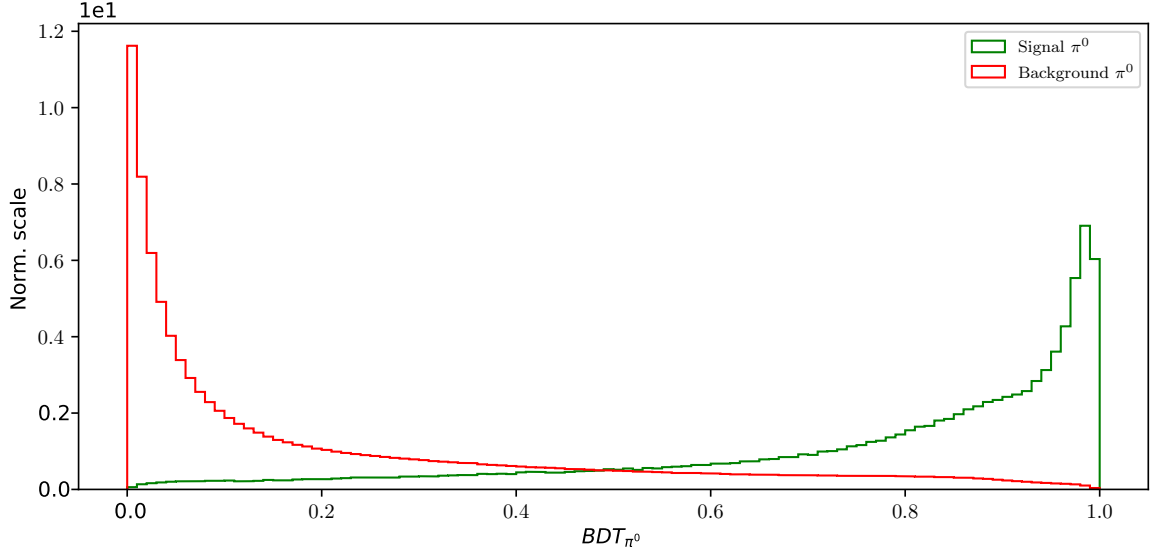


Figure 5.1: Classifier output of the π^0 training for signal and background π^0 candidates.

The distributions for all input variables and their correlations for signal and background candidates can be found in Appendix A for all steps of the ROE clean-up.

5.1.2 γ MVA training

In this MVA training we take the π^0 classifier output of the previous training as an input in order to train a classifier to distinguish between good and bad photons. The π^0 probability information from the previous step is applied to all photon pairs which pass the same π^0 cuts as defined in the previous step. Since it's possible to have overlapping pairs of photons, the π^0 probability is overwritten in the case of a larger value, since this points to a greater probability of a correct photon combination. On the other hand, some photon candidates fail to pass the π^0 selection, these candidates have a fixed value of π^0 probability equal to zero.

The training dataset of γ candidates contains

- 171699 target candidates,
- 177773 background candidates,

where the definition of target is that the photon is an actual photon which is related to a primary MC particle. This tags all photon particles from secondary interactions as background photons. We use the converted γ candidates from the existing Belle particle

580 list.

581 The input variables used in this MVA are

- 582 • p and p_{CMS} of γ candidates,
- 583 • π^0 probability,
- 584 • cluster quantities
 - 585 – E_9/E_{25} ,
 - 586 – theta angle,
 - 587 – number of hit cells in the ECL,
 - 588 – highest energy in cell,
 - 589 – energy error,
 - 590 – distance to closest track at ECL radius.

591 The classifier output variable is shown in Figure 5.2.

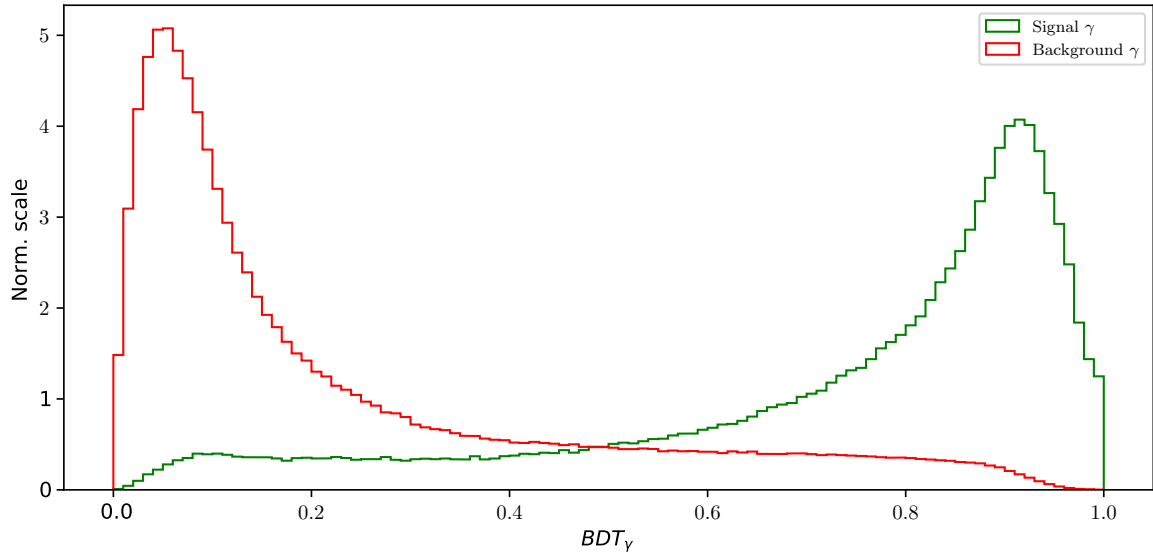


Figure 5.2: Classifier output of the γ training for signal and background γ candidates.

592 With the final weights for photon classification in hand, we apply them to the photon
593 particle list. The cut optimization is shown in Figure 5.3 (left), with the optimal cut on

the γ classifier output at

- $BDT_\gamma > 0.5045$.

Figure 5.3 (right) shows the LAB frame momentum of the photons before and after the cut in logarithmic scale. The signal efficiency and background rejection at this clean-up cut are

- Signal efficiency: $\epsilon_{SIG} = 83.2 \%$,
- Background rejection: $1 - \epsilon_{BKG} = 81.2 \%$.

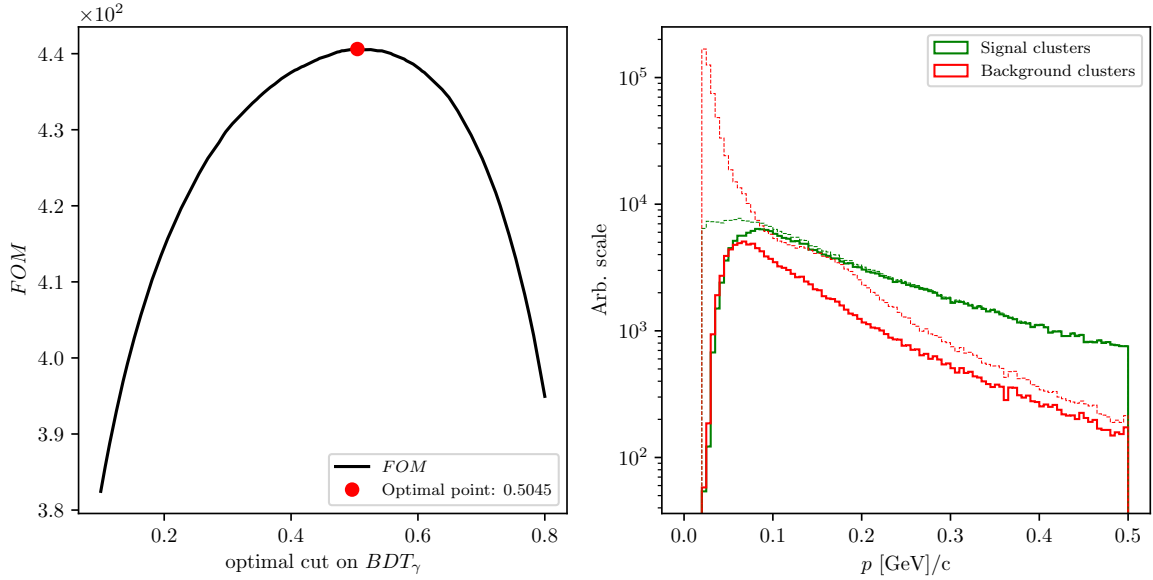


Figure 5.3: The FOM of the classifier output optimization (left) and momentum magnitude in the LAB frame of signal and background photon candidates before and after the optimal cut (right).

The event is now considered to be clean of extra clusters.

5.2 Tracks clean-up

Charged particles leave hits in the detector, which are then grouped into tracks by advanced tracking algorithms. The track is fitted and the track momentum is determined. With the help of particle identification information (PID), we are able to make an intelligent decision about the mass hypothesis of the particle and thus reconstruct the charged particle's four-momentum, which is then added in the loop in Eq. (4.8).

Most of the quality (good) tracks, which come from physics event of interest, come from the IP region, where the collisions occur. Cleaning up the tracks is a more complex procedure than cleaning up the clusters. The following facts need to be taken into account

- (a) good tracks can also originate away from the IP region, due to decays of long-lived particles, such as $K_S^0 \rightarrow \pi^+ \pi^-$,
- (b) charged particles from background sources produce extra tracks, or duplicates,
- (c) low momentum charged particles can curl in the magnetic field and produce multiple tracks,
- (d) secondary interactions with detector material or decays of particles in flight can produce "kinks" in the flight directory, resulting in multiple track fit results per track.

Schematics of all the cases mentioned above are shown in Figure 5.4.

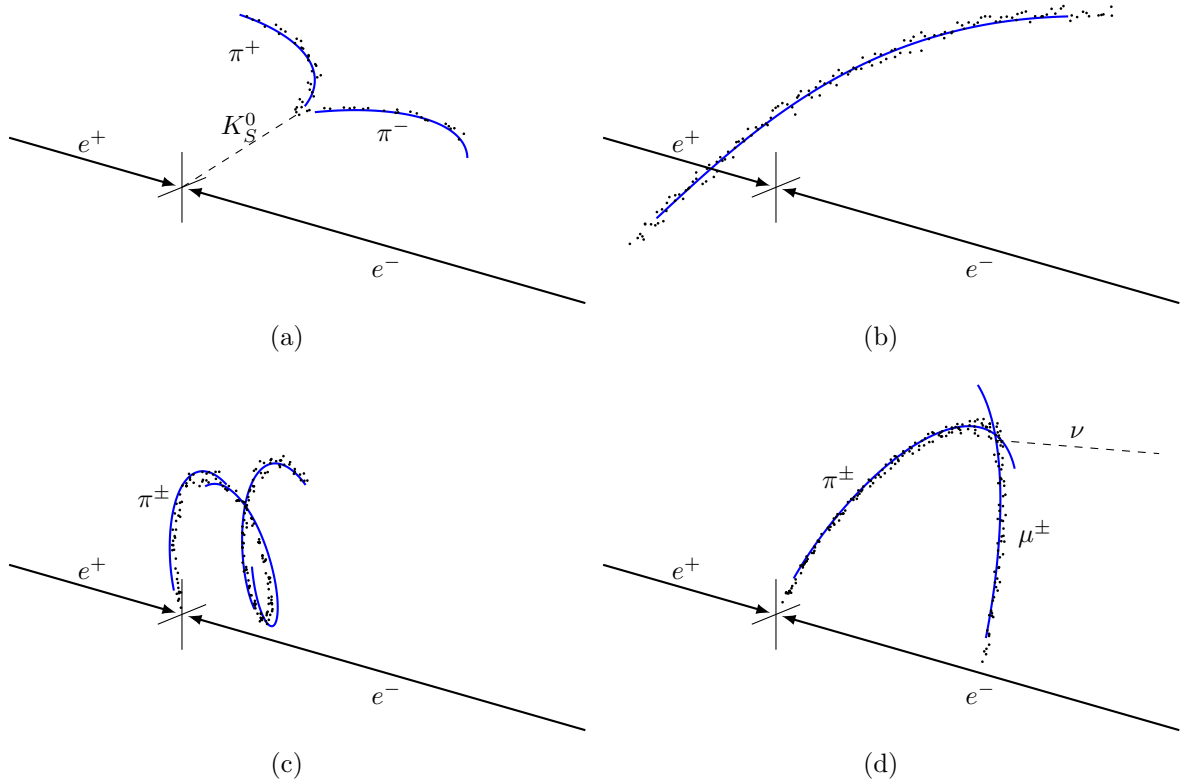


Figure 5.4: (a) Tracks from long-lived neutral particles, which decay away from the IP region, (b) Random tracks from background which are reconstructed, (c) Low-momentum particles which curl in the magnetic field, (d) in-flight decays of particles, which produce a kink in the trajectory.

It is obvious that tracks from the same momentum source should only be taken into account once, or, in case of background tracks, not at all. Such tracks will from this point on be denoted as *extra* tracks, because they add extra four-momentum to our final calculations in Eq. (4.8). At the same time, we have to take care that we don't identify *good* tracks as *extra* tracks. Both of these cases have negative impacts on the final resolution of all variables which depend on information from ROE.

5.2.1 Tracks from long-lived particles

The first step in tracks clean-up is taking care of tracks from long-lived particles. Here we only focus on K_S^0 , since they are the most abundant. This step is necessary because the π^\pm particles, coming from the K_S^0 decays, have large impact parameters, which is usually a trait of background particles. In order to minimize confusion from the MVA point-of-view, these tracks are taken into account separately.

We use the converted K_S^0 candidates from the existing Belle particle list and use a pre-trained Neural Network classifier result in order to select only the good K_S^0 candidates. Figure 5.5 shows the distribution of the K_S^0 invariant mass for signal and background candidates, before and after the classifier cut. The momentum of selected K_S^0 candidates is added to the ROE, while the daughter tracks are discarded from our set.

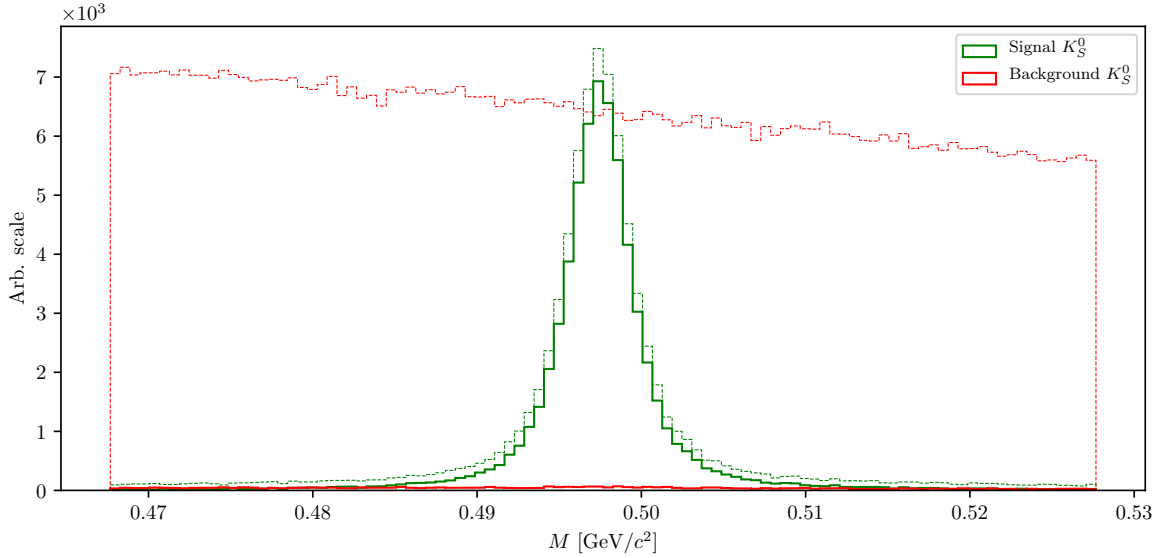


Figure 5.5: Invariant mass of the K_S^0 candidates before (dashed lines) and after (solid lines) the cut on the Neural Network classifier for signal (green) and background candidates (red). Signal peaks at nominal K_S^0 mass, while background covers a wider region.

638 The signal efficiency and background rejection for K_S^0 candidates after this cut and on
639 the full range are

- 640 • Signal efficiency: $\epsilon_{SIG} = 80.7 \%$,
- 641 • Background rejection: $1 - \epsilon_{BKG} = 99.4 \%$.

642 5.2.2 Duplicate tracks

643 All good tracks at this point should be coming from the IP region, since we took care of
644 all the good tracks from long-lived particle decays, therefore we apply a cut on impact
645 parameters for all the remaining tracks

- 646 • $|d_0| < 10 \text{ cm}$ and $|z_0| < 20 \text{ cm}$

647 and proceed with the clean-up of track duplicates.

648 Defining a duplicate track pair

649 In this step we wish to find a handle on secondary tracks from low momentum curlers
650 and decays in flight. The main property for these cases is that the angle between such
651 two tracks is very close to 0° or 180° , since tracks deviate only slightly from the initial
652 direction, but can also be reconstructed in the opposite way. Figure 5.6 shows the
653 distribution of the angle between two tracks in a single pair for random track pairs and
654 duplicate track pairs, where the latter were reconstructed as two same-sign or opposite-
655 sign tracks.

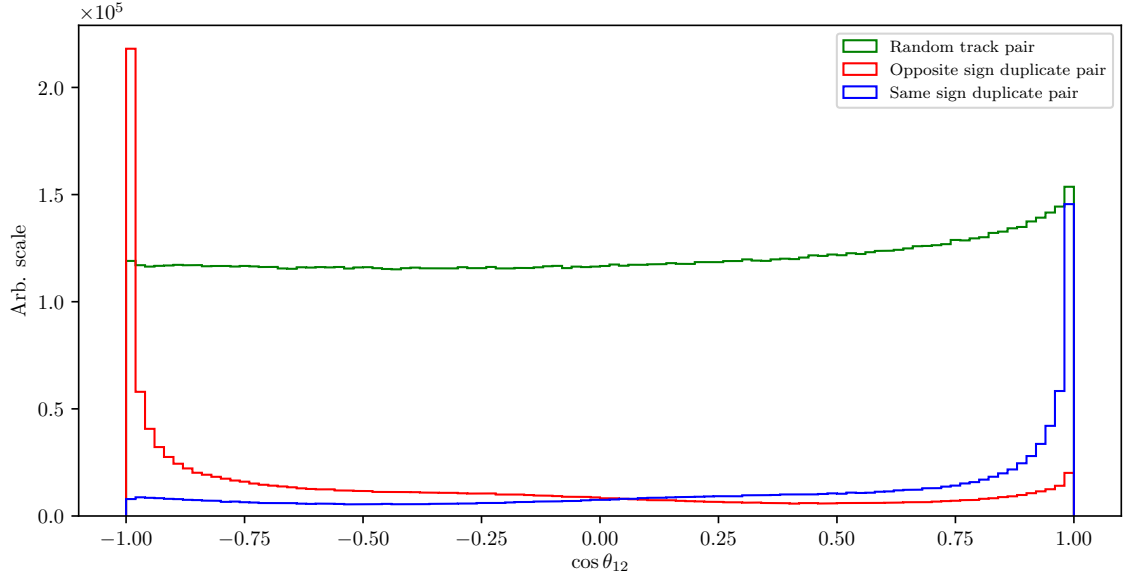


Figure 5.6: Distribution of the angle between two tracks in a single pair for random track pairs (green) and duplicate track pairs, where the latter were reconstructed as two same-sign (blue) or opposite-sign tracks (red).

If the particle decayed mid-flight or produced multiple tracks due to being a low-momentum curler, then, as the name suggests, these particles most likely had low momentum in the transverse direction, p_T . Since both tracks originate from the same initial particle, the momentum difference should also peak at small values. Figure 5.7 shows the momentum and momentum difference of tracks which belong to a random or a duplicate track pair.

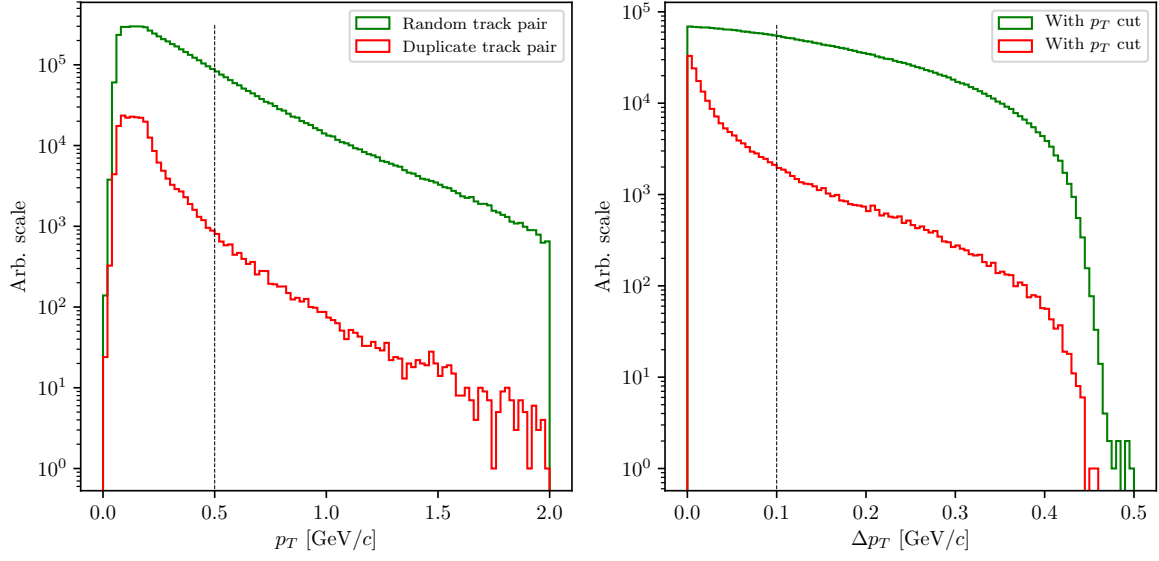


Figure 5.7: Distribution of transverse momentum p_T (left) and transverse momentum difference Δp_T (right) for all tracks coming from random (green) or duplicate track pairs (red). The plot on the right already includes the cut on p_T from the plot on the left.

We impose a cut of

- $p_T < 0.5 \text{ GeV}/c$,
- $|\Delta p_T| < 0.1 \text{ GeV}/c$,

in order to cut down the number of random track pairs, while retaining a high percentage of duplicate track pairs. After all the cuts defined in this chapter, the final distribution of the angle between two tracks is shown in Figure 5.8.

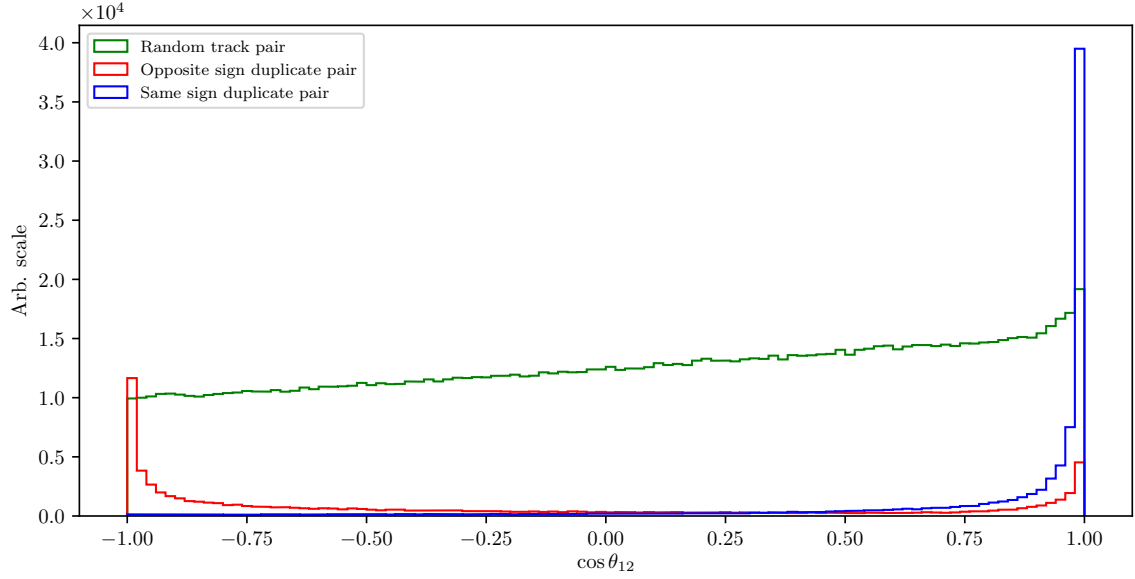


Figure 5.8: Distribution of the angle between two tracks in a single pair after applying the selection cuts defined in this subsection. The distributions are shown for random track pairs (green) and duplicate track pairs, where the latter were reconstructed as two same-sign (blue) or opposite-sign tracks (red).

Training the duplicate track pair MVA

This final sample of track pairs is now fed into an MVA, which is trained to recognize duplicate track pairs over random ones. The training dataset contains

- 113707 target candidates,
- 190314 background candidates,

where the definition of target is that the track pair is a duplicate track pair.

The input variables used in this MVA are

- angle between tracks,
- track quantities
 - impact parameters d_0 and z_0 ,
 - transverse momentum p_T ,

- helix parameters and helix parameter errors of the track,
- track fit p -value,
- number of hits in the SVD and CDC detectors

The classifier is able to distinguish between random and duplicate track pairs in a very efficient manner, as shown in Figure 5.9.

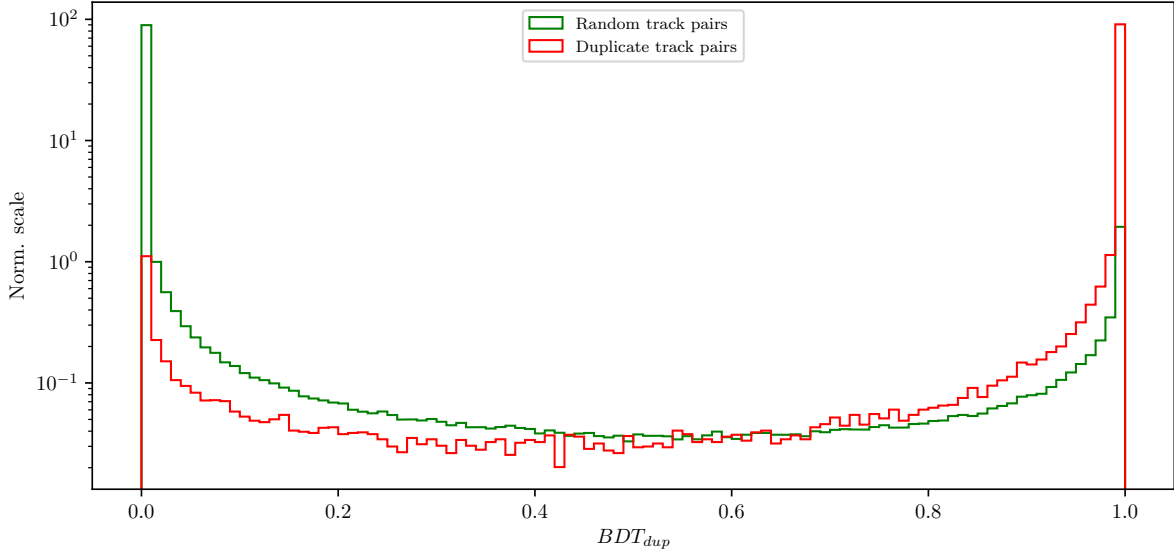


Figure 5.9: Classifier output of the track pair training for random track pairs and duplicate track pairs.

The FOM function for optimal cut selection is shown in Figure 5.10 (left), along with the angle between the two tracks before and after the optimal cut (right). The optimal cut for duplicate track selection is

- $BDT_{duplicate} > 0.9985$.

The signal efficiency and background rejection for duplicate pair candidates after this cut is

- Signal efficiency: $\epsilon_{SIG} = 87.2 \%$,
- Background rejection: $1 - \epsilon_{BKG} = 98.8 \%$,

where signal and background represent duplicate and random track pairs, respectively.

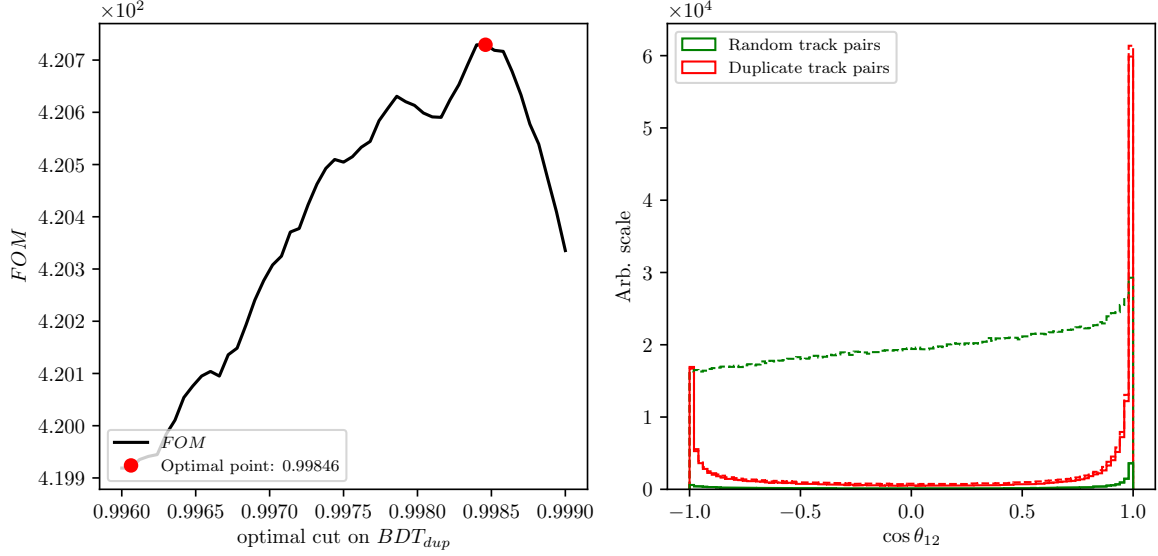


Figure 5.10: The optimization of the FOM function for the cut on classifier output (left) and distribution of the angle between two tracks in a single pair before (dashed) and after (solid) applying the optimal cut on the output classifier for random and duplicate track pairs (right).

Defining duplicate tracks

What remains now is to decide which track from the duplicate track pair to keep and which to discard. For this purpose we apply duplicate pair-level information to each track in the pair in the form of

$$\Delta f = f_{this} - f_{other}, \quad (5.1)$$

where f is an arbitrary variable from the list of track quantities in Subsection 5.2.2. From the point-of-view of *this* track, a track is more *duplicate*-like if the following is true

- $\Delta d_0, \Delta z_0 > 0$ (*this* track further away from the IP region),
- $\Delta p_T, \Delta p_Z < 0$ (*this* track has lower momentum),
- $\Delta N_{SVD}, \Delta N_{CDC} < 0$ (*this* track has less hits in the SVD and CDC),

703 Additionally we define an MC truth variable

$$\Delta\chi^2 = \chi_{this}^2 - \chi_{other}^2, \quad \chi^2 = \sum_{i=x,y,z} \frac{(p_i - p_i^{MC})^2}{\sigma(p_i)^2}, \quad (5.2)$$

704 where we compare all components of track momentum to the true values. If $\Delta\chi^2 >$
 705 0, then *this* track has a higher probability of being a duplicate track and should be
 706 discarded.

However, it turns out that solving this problem is not as simple as discarding one track and keeping the other one. An additional complication here is that we can have more than one extra track from the same initial particle, which leads to track pairs where both tracks are track duplicates. For example, if we have the following case

$$\begin{aligned} t_1 &: \text{good track,} \\ t_2 &: \text{extra track,} \\ t_3 &: \text{extra track,} \\ \text{pair}_1 &: (t_1, t_2), \\ \text{pair}_2 &: (t_1, t_3), \\ \text{pair}_3 &: (t_2, t_3), \end{aligned}$$

where t_1 is the original track and t_2 and t_3 are extra tracks, with t_3 being even more duplicate-like with respect to t_2 . Here tracks t_2 and t_3 should be discarded while t_1 should be kept. We can achieve this if we overwrite existing pair-level information in the tracks for cases where the variable difference Δf is more duplicate-like. If we follow the same example, we could fill information about the property f in six different orders.

$$\begin{aligned} 1. & (t_1, t_2*) \rightarrow (t_1, t_3*) \rightarrow (t_2*, t_3*), \\ 2. & (t_1, t_2*) \rightarrow (t_2*, t_3*) \rightarrow (t_1, t_3*), \\ 3. & (t_1, t_3*) \rightarrow (t_2, t_3*) \rightarrow (t_1, t_2*), \\ 4. & (t_1, t_3*) \rightarrow (t_1, t_2*) \rightarrow (t_2*, t_3*), \\ 5. & (t_2, t_3*) \rightarrow (t_1, t_3*) \rightarrow (t_1, t_2*), \\ 6. & (t_2, t_3*) \rightarrow (t_1, t_2*) \rightarrow (t_1, t_3*), \end{aligned}$$

707 where the "*" symbol denotes when a track is recognized as a duplicate track with respect
 708 to the other track. We see that no matter the order, both t_2 and t_3 get recognized as
 709 duplicate tracks correctly.

710 Training the duplicate track MVA

711 The training procedure is similar as before. The sample of tracks from duplicate track
 712 pairs is now fed into an MVA, which is trained to distinguish duplicate tracks from good
 713 tracks. The training dataset contains

714 • 84339 target candidates,

715 • 68280 background candidates,

716 where the definition of target is that the track is a duplicate track.

717 The input variables used in this MVA are

718 • theta angle of the track momentum,

719 • track quantities

720 – impact parameters d_0 and z_0 and their errors,

721 – CMS frame momentum p_{CMS} and momentum components p_T and p_z

722 – number of hits in the SVD and CDC detectors

723 – track fit p -value,

724 • pair-level information

725 – $\Delta d_0, \Delta z_0, \Delta N_{CDC}, \Delta N_{SVD}, \Delta p_T, \Delta p_z, \Delta p$ -value.

726 The weights from this training are applied to the tracks, where now each track has a
727 certain probability of being a duplicate track. We then compare these values between
728 both tracks in each track pair as

$$\Delta BDT_{final} = BDT_{final}^{this} - BDT_{final}^{other}, \quad (5.3)$$

729 which is again applied to all track pairs and overwritten for tracks which are more
730 duplicate-like. The classifier output and the classifier output difference for each track is
731 shown in Figure 5.11.

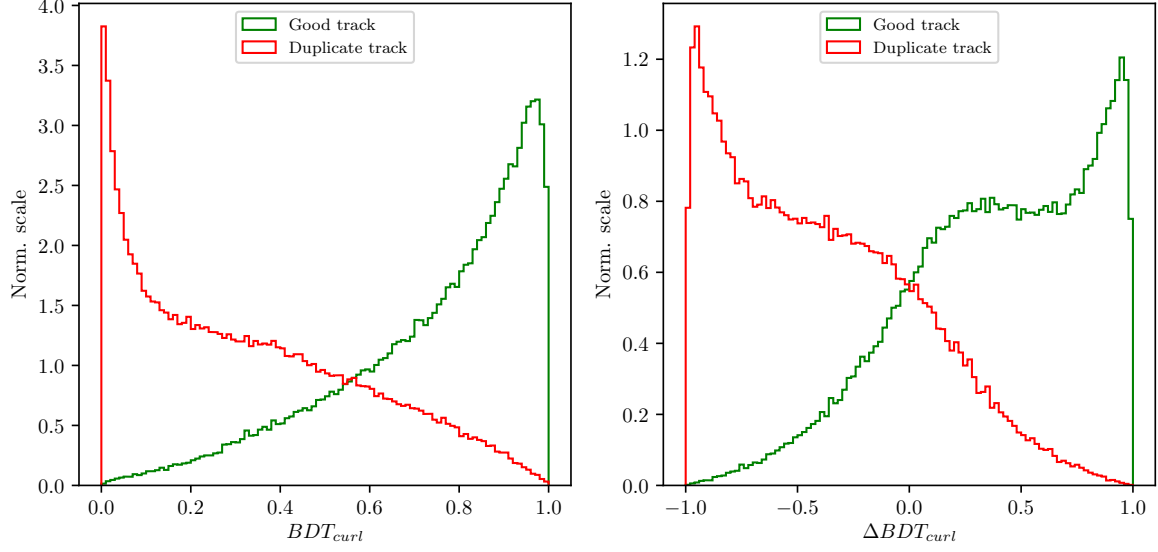


Figure 5.11: Classifier output of the MVA training for curling track recognition (left) and difference of the classifier output, calculated for each track in a track pair (right).

Finally, we select all duplicate tracks which survive the cut

$$\Delta BDT_{final} > 0 \quad (5.4)$$

and discard them from our ROE. We can check the performance of our duplicate track classifier by applying the procedure on a validation sample of duplicate track pairs and compare the predicted result with the truth, based on Eq. (5.2). Table 5.1 shows the performance of the duplicate track recognition in the form of percentages of correctly and incorrectly identified duplicate and original tracks. The model seems to perform well and the event is now considered to be clean of duplicate tracks.

	Predicted duplicate track	Predicted good track
Duplicate track	83.07 %	22.62 %
Good track	16.93 %	77.38%

Table 5.1: Ratios of correctly classified and misclassified tracks.

5.3 Belle clean-up

The clean-up, used standardly at Belle, is much simpler and relies only on a set of rectangular cuts for neutral particles as well as charged ones. In case of photons, a

single cut on photon energy is applied, depending on the region where the photon hit the relevant part of the detector. The photon cuts are summarized in Table 5.2.

	$17^\circ < \theta < 32^\circ$	$32^\circ < \theta < 130^\circ$	$130^\circ < \theta < 150^\circ$
E_γ	$> 100 \text{ MeV}$	$> 50 \text{ MeV}$	$> 150 \text{ MeV}$

Table 5.2: Photon selection for the Belle clean-up procedure. Different cuts are applied on photons in different parts of the detector

In case of tracks, pairs are selected which satisfy the following criteria:

- $p_T < 275 \text{ MeV}/c$,
- $\Delta p = |\mathbf{p}_1 - \mathbf{p}_2| < 100 \text{ MeV}/c$,
- $\cos \theta(\mathbf{p}_1, \mathbf{p}_2) < 15^\circ$ for same sign,
- $\cos \theta(\mathbf{p}_1, \mathbf{p}_2) > 165^\circ$ for opposite sign.

Of the two tracks, the one with a larger value of formula in Eq. 5.5 is discarded. The remaining tracks in the event then need to satisfy the conditions described in Table 5.3.

$$(\gamma|d_0|)^2 + |z_0|^2, \quad \gamma = 5. \quad (5.5)$$

	$p_T < 250 \text{ MeV}/c$	$250 \text{ MeV}/c < p_T < 500 \text{ MeV}/c$	$p_T > 500 \text{ MeV}/c$
$ d_0 $	$< 20 \text{ cm}$	$< 15 \text{ cm}$	$< 10 \text{ cm}$
$ z_0 $	$< 100 \text{ cm}$	$< 50 \text{ cm}$	$< 20 \text{ cm}$

Table 5.3: Photon selection for the Belle clean-up procedure. Different cuts are applied on photons in different parts of the detector

5.4 Clean-up results

In this section the results of the ROE clean-up are shown. It is obvious that cleaning up the event affects the shape of various distribution, especially ΔE and M_{BC} , which we are most interested in. Since the reconstruction procedure includes cuts on the cleaned-up variables, the clean-up also affects the efficiency of the reconstructed sample, not only the resolution.

We compare the clean-up setup, defined in this analysis, to the standard clean-up used by Belle, and to a default case, where no clean-up was applied at all. We apply the clean-up procedure to our signal MC sample with all the applied cuts, defined in 4.6, except

760 for the signal categorization cuts. Figure 5.12 (left) shows signal candidate distributions
 761 of ΔE and M_{BC} for various clean-up setups. Focusing on the ROE clean-up, we see an
 762 improvement in resolution in both observed variables and an overall decrease in efficiency.
 763 The efficiency decrease is expected, since the cleaned-up variables are able to better
 764 isolate the perfectly reconstructed candidates and discard the non-perfect candidates.
 765 In fact, the efficiency of the perfectly reconstructed candidates increases after the ROE
 766 clean-up, as shown in Figure 5.12 (right). The signal MC sample after in case of the Belle
 767 clean-up also shows a slight improvement in the resolution, but looking at the perfectly
 768 reconstructed candidates we see that this clean-up procedure is not optimal. Table 5.4
 769 shows ratios of efficiencies and $FWHM$'s of the clean-up procedures for the perfect
 770 signal with respect to the default case, based on the ΔE distribution. While both the
 771 Belle and ROE clean-up improve the resolution, ROE clean-up performs significantly
 772 better and also increases the amount of the perfectly reconstructed candidates in the
 773 final sample.

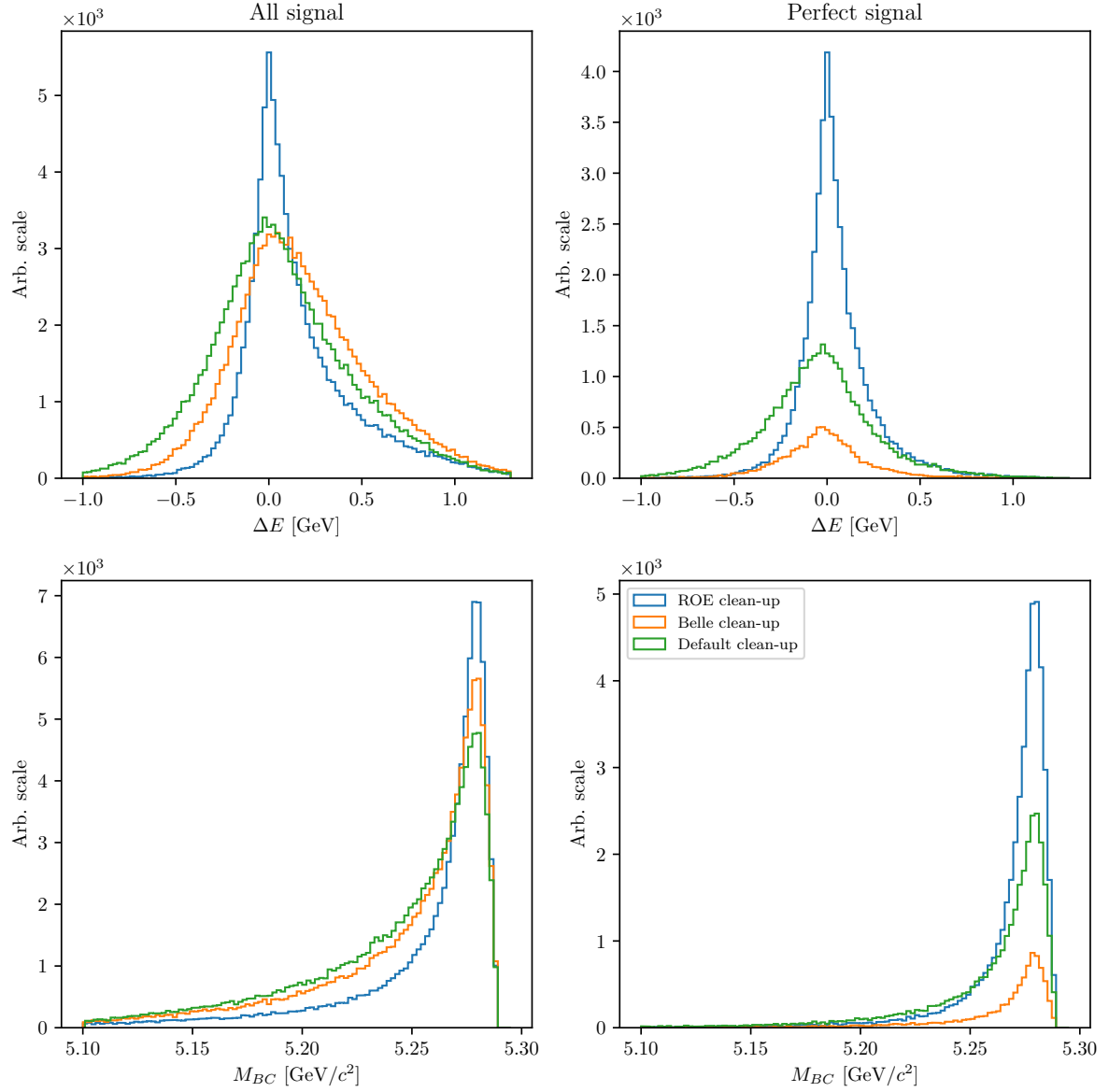


Figure 5.12: ΔE and M_{BC} distributions for various types of clean-up procedures. The figures on the left are shown for the full signal sample after the stated cuts, while the figures on the right are shown for the perfectly reconstructed signal candidates. For ROE clean-up, the procedure seems to improve resolution as well as increase the amount of perfectly reconstructed candidates, relative to the default case.

	Efficiency ratio	FWHM ratio
Belle clean-up	28.5 %	75.0 %
ROE clean-up	140.1 %	35.0 %

Table 5.4: Comparison of efficiencies and $FWHM$'s of ROE and Belle clean-up setups with respect to the default case (no clean-up).

Another variable which heavily depends on the clean-up is the charge product of the signal and companion B meson candidate, already defined in Eq. (4.15), shown in Figure 5.13 for various clean-up procedures. The figure shows an improved resolution of the distribution, which means that candidates migrate to the correct value of the charge product after the clean-up. Looking at the perfectly reconstructed candidates we again see the increase in the bin corresponding to the correct charge product. As a cross-check, we can also look at ΔE and M_{BC} variables for each value of the charge product. These plots are shown for the full signal MC sample in Figure 5.14 and they show a clear resolution improvement for the correct value of the charge product in the case of the ROE clean-up. For other values of the charge product there also seems to be a small improvement for both cases of clean-up, but it is negligible compared to the plots in the second column. This supports our choice of signal categorization, defined in Section 4.5, where we select only candidates with the correct value of the charge product.

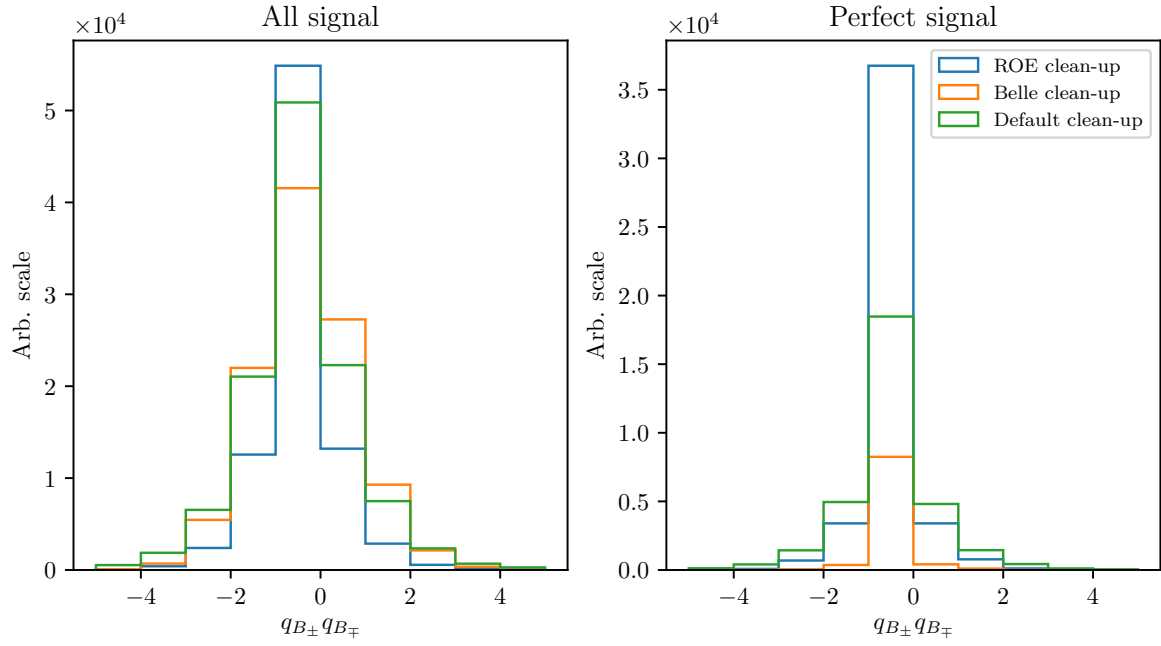


Figure 5.13: Distribution of the charge product of both B mesons for various types of clean-up procedures, shown on the full signal MC (left) and for the perfectly reconstructed signal candidates (right). For ROE clean-up, the procedure seems to increase the number of perfectly reconstructed candidates.

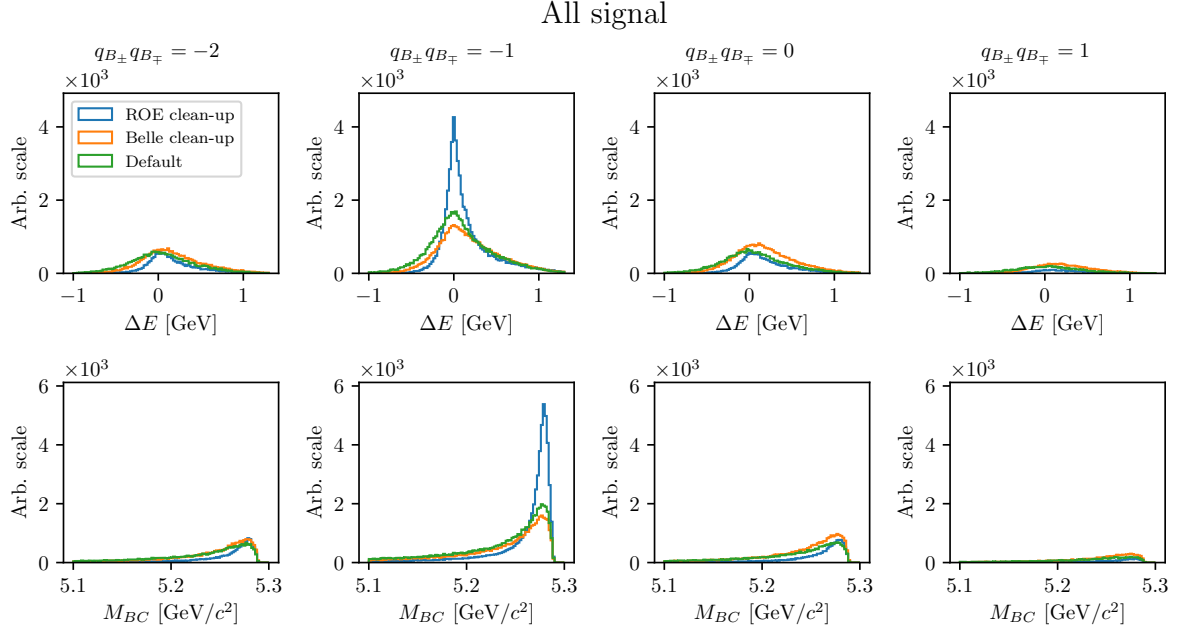


Figure 5.14: Distributions of ΔE (top) and M_{BC} (bottom) for various types of clean-up procedures, split by specific values of the charge product, shown for the full signal MC. There is a significant improvement in resolution after ROE-cleanup for the case of the correct value of the charge product.

5.5 ROE clean-up validation

The ROE clean-up seems to perform well on signal MC based on the results in the previous section. However, it is necessary to make sure that this procedure performs as well on other simulated and measured data, which is done in this section. The clean-up procedure is validated on the control sample,

$$B^+ \rightarrow \bar{D}^0 \ell^+ \nu, \quad D^0 \rightarrow K^+ K^-,$$

which was already defined in Section 2.2. The control candidates are reconstructed in the same manner as the signal candidates. In addition to the same cuts applied as in the previous section we also apply a selection to make the control sample more significant. We discard all candidates which fail to pass the cut on invariant mass of the two kaons

$$1.852 \text{ GeV}/c^2 < m_{KK} < 1.876 \text{ GeV}/c^2 \quad (5.6)$$

as shown in Figure 5.15.

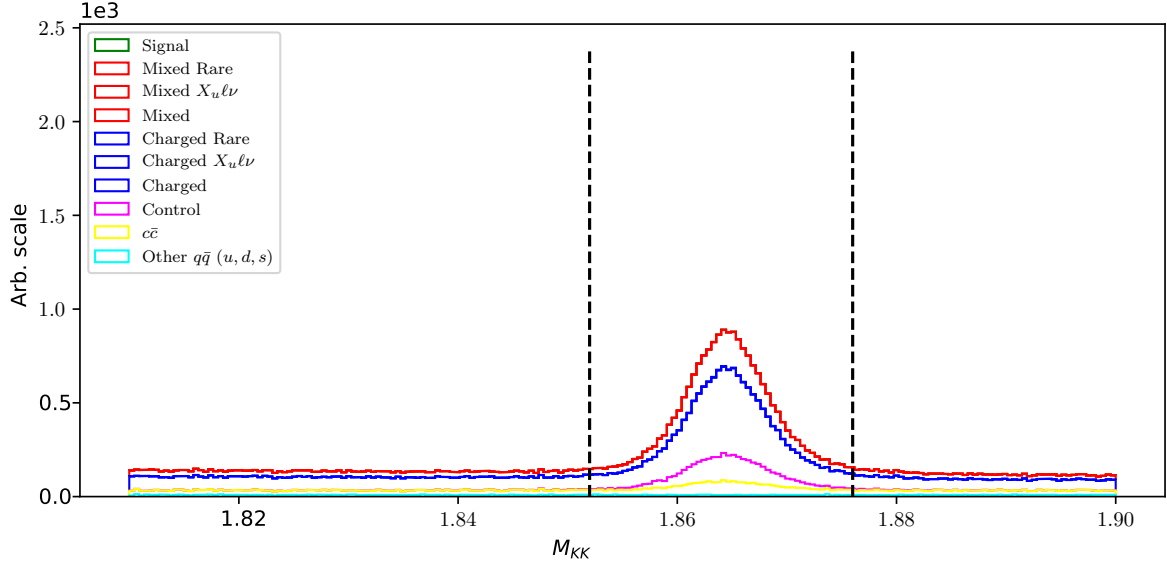


Figure 5.15: Distributions of m_{KK} for the full MC dataset. The black lines represent the cut on region in the m_{KK} distribution where the control sample is enhanced.

With the control sample selection determined, we now run the reconstruction with and without the ROE clean-up procedure on MC and data. For the purpose of this validation we only run the reconstruction over experiment no. 43, which corresponds to about 56.2 fb^{-1} .

The affects of the ROE clean-up are shown in Figure 5.16. We see that data and MC agree well, and evidently even better after the clean-up procedure. The control sample resolution seems very poor in the case without the clean-up, but it improves significantly if the clean-up procedure is applied, as expected. The simulated background also seems to gain an improvement in the resolution, but this is likely due to the background consisting of similar candidates as the control sample. This means that the clean-up performs as expected due to the nature of the decays and does not arbitrarily shape the background to be more signal like. Additionally, it should be pointed out that, after the clean-up, the simulated background resolution is worse compared to the control decay resolution, while this is not the case if the clean-up procedure is not performed.

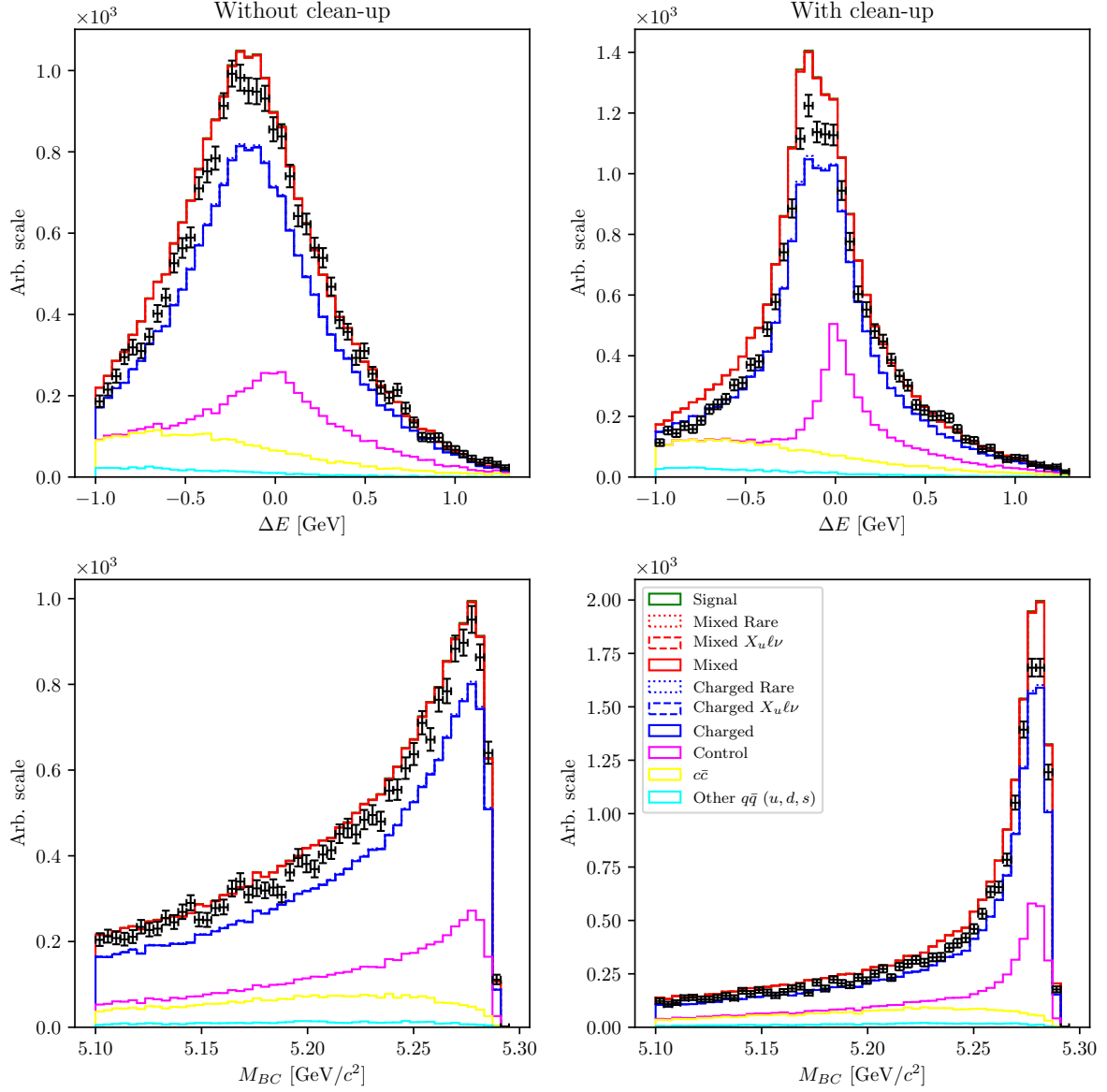


Figure 5.16: Distributions of ΔE (top) and M_{BC} bottom for the case without (left) and with ROE clean-up (right). The resolution of the control sample is improved and the MC and data agree well in all aspects. While the simulated background resolution is also improved, it is worse compared to the resolution of the control sample.

To perform the clean-up validation in greater detail we also compare the data and MC agreement in bins of the charge product of the two B mesons. Figure ?? shows the cleaned-up versions of ΔE and M_{BC} for each charge product bin in the same manner as shown in the previous section. We see that the MC and data agreement persists in all

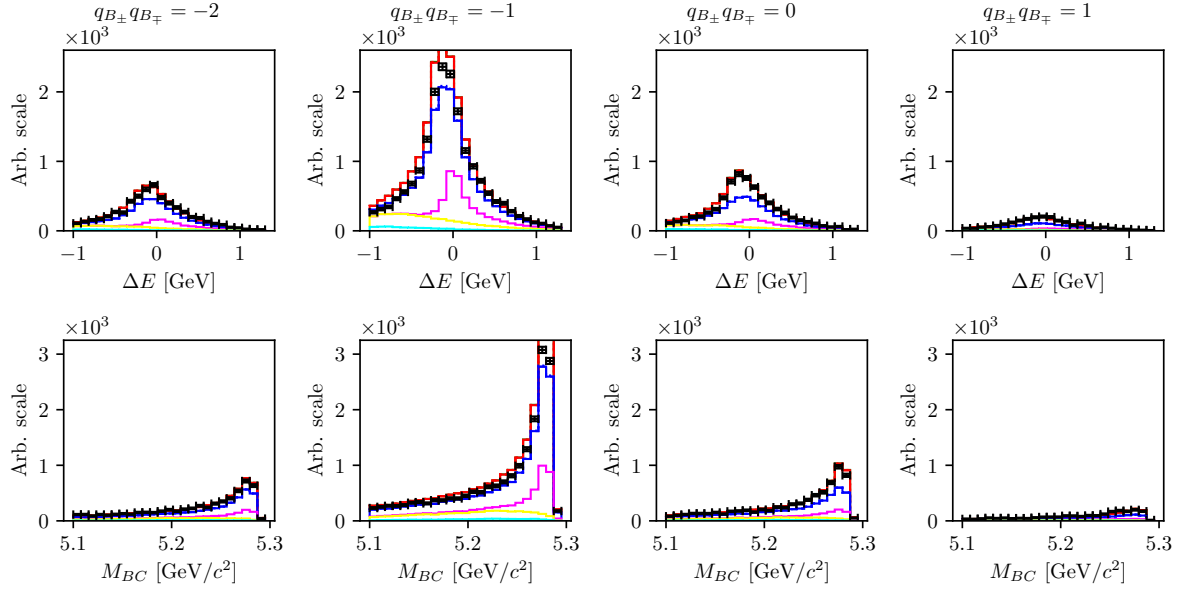


Figure 5.17: Distributions of ΔE (top) and M_{BC} (bottom) split in bins of the charge product of the two B mesons.

812 The ROE clean-up procedure seems to perform well. It significantly improves the resolu-
 813 tion of the signal/control candidates and increases the amount of perfectly clean events.
 814 The clean-up procedure was also applied to data and no disagreement with respect to
 815 the simulated MC samples was found. This means that the procedure does not differ
 816 between MC and data and does not affect them differently. The procedure was therefore
 817 validated in great detail and is suitable to be used in this analysis.

Chapter 6

Background suppression

This chapter shows the procedure in suppressing various kinds of background by applying cuts on MVA classifier outputs.

6.1 Resonant background

In this analysis we study decays with kaons in the final state. This means that standard procedures in $b \rightarrow u$ analyses in order to suppress $b \rightarrow c$ backgrounds, such as K -veto, are not possible. As a consequence, our final sample consists of combinations of K pairs coming also from $b \rightarrow c$ sources, such as $D^0 \rightarrow K^+ K^-$. Such candidates usually have resonance-like properties in the two-kaon invariant mass spectrum. Figure 6.1 shows this invariant mass spectrum of two kaons, m_{KK} , where obvious resonant structures are present from sources like

- $\phi \rightarrow K^+ K^-$ (sharp resonance at $\sim 1.019 \text{ GeV}/c^2$),
- $D^0 \rightarrow K^+ K^-$ (sharp peak at $\sim 1.864 \text{ GeV}/c^2$),
- $D^0 \rightarrow K^+ \pi^-$ (wide, shifted peak, due to kaon miss-identification).

In order to suppress these resonant backgrounds, while studying the signal or control decay, we impose a set of the following cuts

- Signal cut: $|m_{KK} - m_\phi| > \Delta_\phi$, $|m_{KK} - m_{D^0}| > \Delta_{D^0}$, $|m_{K\pi} - m_{D^0}| > \Delta_{D^0}$,
- Control cut: $|m_{KK} - m_{D^0}| \leq \Delta_{D^0}$, $|m_{K\pi} - m_{D^0}| > \Delta_{D^0}$,

where $m_\phi \approx 1.019 \text{ GeV}/c^2$ and $m_{D^0} \approx 1.864 \text{ GeV}/c^2$ are nominal masses of the ϕ and D^0 mesons, and $\Delta_\phi \approx 8 \times 10^{-3} \text{ GeV}/c^2$ and $\Delta_{D^0} \approx 1.5 \times 10^{-2} \text{ GeV}/c^2$ are symmetric cut widths around the nominal mass values for the ϕ and D^0 mesons, respectively. By imposing the signal or control cut on our data, we are able to efficiently isolate the

desired subset, which is very useful for further studies of the control decay. Table 6.1 shows the subsample efficiency after applying either of the cuts.

	$\epsilon(\text{Signal cand.})$	$\epsilon(\text{Control cand.})$	$\epsilon(\phi \text{ resonance cand.})$
Signal cut	95.4%	4.0%	13.6%
Control cut	1.9%	96.0%	0.0%

Table 6.1: Various subset efficiencies after imposing the signal or control cut on the KK invariant mass.

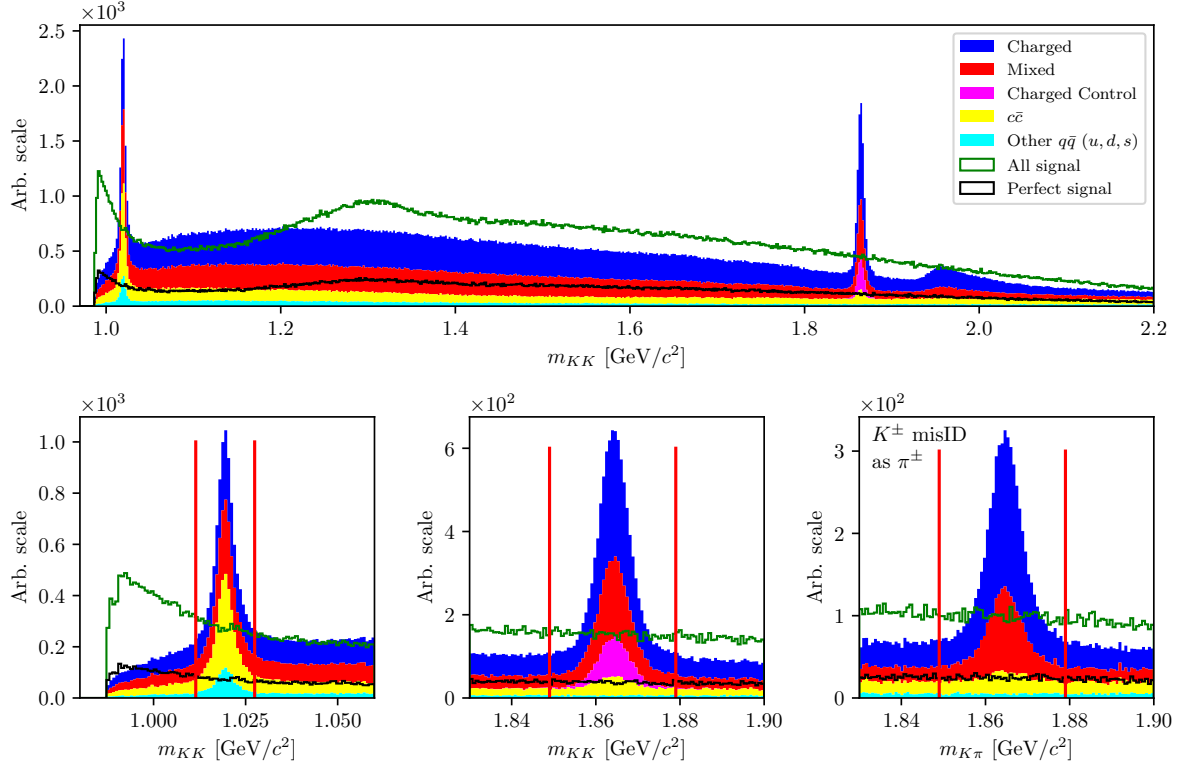


Figure 6.1: Invariant mass of two correctly reconstructed kaons (left) and invariant mass of two kaons, where one was misidentified as a pion (right). Signal (green) and perfect signal (black) are equally scaled up.

6.2 Continuum suppression

Continuum background are physics processes where continuum states are produced in electron and positron collisions

$$e^+e^- \rightarrow q\bar{q},$$

where $q = u, d, s$ or c , and are a sizable contribution to $B\bar{B}$ events. Additionally to kinematic constraints to separate $e^+e^- \rightarrow \Upsilon(4S) \rightarrow B\bar{B}$ decays from $e^+e^- \rightarrow q\bar{q}$, properties of the "event shape" are also often used, because phase-space distributions of decayed particles differ for these two processes. Continuum background events are generated in a back-to-back way in the CMS frame, so hadrons produced in the quark fragmentation possess only a small transverse momentum compared to the initial momentum magnitude. This leads to a spatially confined, jet-like structure. On the other hand B mesons from $B\bar{B}$ events are produced almost at rest in the CMS frame. Their decay products from an isotropic distribution in the detector, which yields a spherical event shape.

6.2.1 Characteristic variables

Information on the phase-space distribution of decay particles is obtained in a number of different ways. In this subsection different characteristic variables are presented which are used in the MVA training. They all focus on kinematic and shape differences between the two processes, which we want to discriminate.

Thrust and related variables

It is possible to define a thrust axis \mathbf{T} for a collection of N momenta p_i as a unit vector along which their total projection is maximal. Thrust axis \mathbf{T} can be obtained by maximizing the expression

$$\mathbf{T} = \frac{\sum_i |\mathbf{T} \cdot \mathbf{p}_i|}{\sum_i |\mathbf{p}_i|}. \quad (6.1)$$

In this case, a related variable is $|\cos \theta_T|$, where θ_T is the angle between the thrust axis of the momenta from B meson decay particles, and the thrust axis of all particles in the ROE. Since both B mesons in $B\bar{B}$ events are produced at rest, their decay particles, and consequentially their thrust axes, are uniformly distributed in the range $[0, 1]$. On the other hand, decay particles from continuum events follow the direction of the jets in the event. As a consequence, the thrusts of both the B meson and the ROE are strongly directional and collimated, which results in a large peak at $|\cos \theta_T| \approx 1$. Additionally, one can also use the variable $|\cos \theta_{TB}|$, which is the thrust axis between the B candidate and the beam axis. For B candidates from $B\bar{B}$, this distributions is again uniformly distributed, while for candidates from continuum events this distribution follows the distribution of the jets with the function $1 + \cos^2 \theta_{T,B}$. Figure 6.2 shows the distributions of $|\cos \theta_T|$ (left) and $|\cos \theta_{T,B}|$ (right) for different B meson candidates.

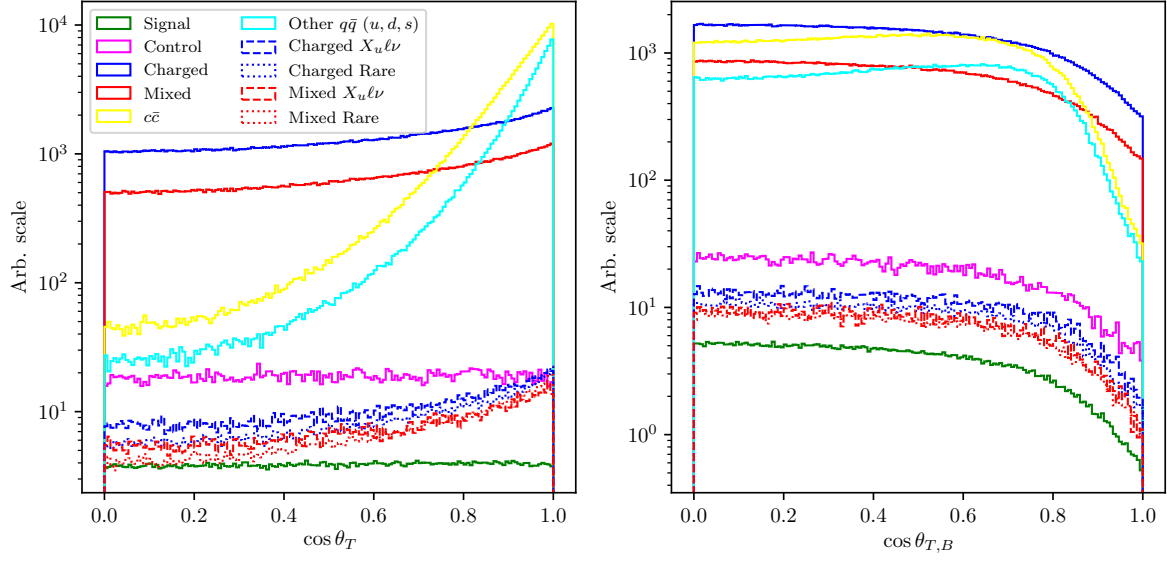


Figure 6.2: Distributions of $|\cos \theta_T|$ (left) and $|\cos \theta_{T,B}|$ (right) for different B meson candidates.

875 CLEO cones

876 CLEO cones have been introduced by the CLEO collaboration [7] and are an additional
877 specific tool to provide optimal background discrimination. They are nine variables
878 corresponding to the momentum flow around the thrust axis of the B meson candidate,
879 binned in nine cones of 10° around the thrust axis, as illustrated in Figure 6.3.

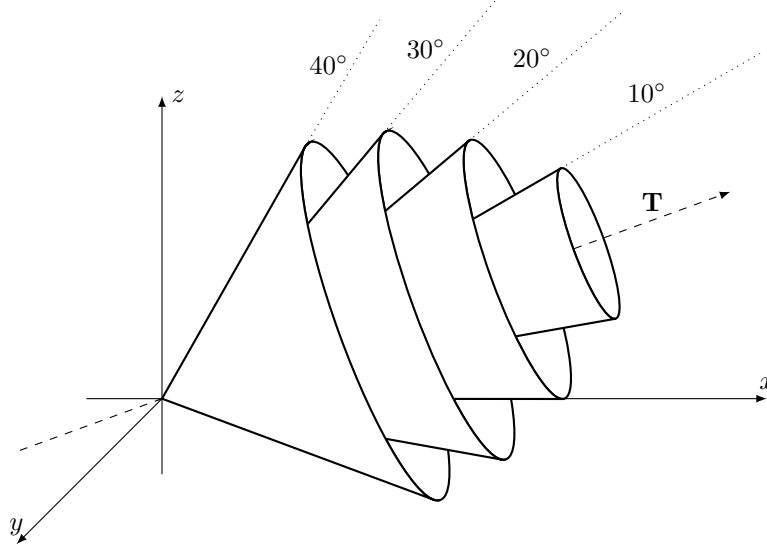


Figure 6.3: Concept of CLEO cones. \mathbf{T} denotes the thrust axis of the B meson candidates in the event. Each variable corresponds to a momentum flow around the thrust axis in steps of 10° .

KSFW moments

Fox-Wolfram moments are another useful parametrization of phase-space distribution of energy flow and momentum in an event. For a collection of N momenta p_i , the k -th order normalized Fox-Wolfram moment R_k is defined as

$$R_k = \frac{H_k}{H_0} = \frac{1}{H_0} \sum_{i,j} |p_i| |p_j| P_k(\cos \theta_{ij}), \quad (6.2)$$

where θ_{ij} is the angle between p_i and p_j , and P_k is the k -th order Legendre polynomial. For events with two strongly collimated jets, R_k takes values close to 0 (1) for odd (even) values of k , so these moments provide a convenient discrimination between $B\bar{B}$ and continuum events.

Belle developed a refined generation of Fox-Wolfram moments, called Kakuno-Super-Fox-Wolfram (KSFW) moments to further suppress the continuum background. There are 17 different KSFW moments which are grouped into R_k^{so} , R_k^{oo} and R_k^{ss} [8]. The latter ones are excluded due to correlations with B meson specific variables.

6.2.2 MVA training

Most of the characteristic variables, described in subsection 6.2.1, were taken together in order to train a single MVA classifier for continuum suppression. All characteristic

variables were checked for possible q^2 correlation. Variables with significant correlation or complex shapes in the 2D plot were discarded from the training set, since they would have introduced unwanted dependence on the unreliable model, ISGW2, used for signal MC generation. Additionally, all of the characteristic variables in our set do not depend on the signal mode, they only differ in the kinematic and topological aspects of $B\bar{B}$ and continuum background events.

The training dataset consisted of 2×10^5 candidates, where 50 % of the candidates are correctly reconstructed signal events, 25 % are $u\bar{u}$, $d\bar{d}$ and $s\bar{s}$ background with expected proportions, and 25 % is $c\bar{c}$ background. Since the full Belle dataset is experiment dependent, we construct the training dataset by proportionally sampling each MC dataset, corresponding to the appropriate experiment number.

The training variable set consisted of

- B meson direction and thrust related variables
 - magnitude of thrust axes of B and ROE ,
 - cosine of angle between thrust axis of B and thrust axis of ROE ,
 - cosine of angle between thrust axis of B and beam direction,
 - reduced Fox-Wolfram moment R_2 ,
- all 9 CLEO Cones
- KSFW Moments
 - $R_{01}^{so}, R_{02}^{so}, R_{03}^{so}, R_{04}^{so}$,
 - $R_{10}^{so}, R_{12}^{so}, R_{14}^{so}$,
 - $R_{20}^{so}, R_{22}^{so}, R_{24}^{so}$,
 - $R_0^{oo}, R_1^{oo}, R_2^{oo}, R_3^{oo}, R_4^{oo}$,
- FlavorTagging variables
 - qp of e, μ, ℓ ,
 - qp of intermediate e, μ, ℓ ,
 - qp of $K, K/\pi$, slow pion, fast hadron,
 - qp of maximum P^*, Λ , fast-slow-correlated (FSC),

• Other

– $\Delta z, \Delta t$.

Figure 6.4 shows the classifier output for various types of background, all in expected MC proportions. B meson candidates from continuum background are dominant at lower values, while candidates from $B\bar{B}$ events populate the region with higher values.

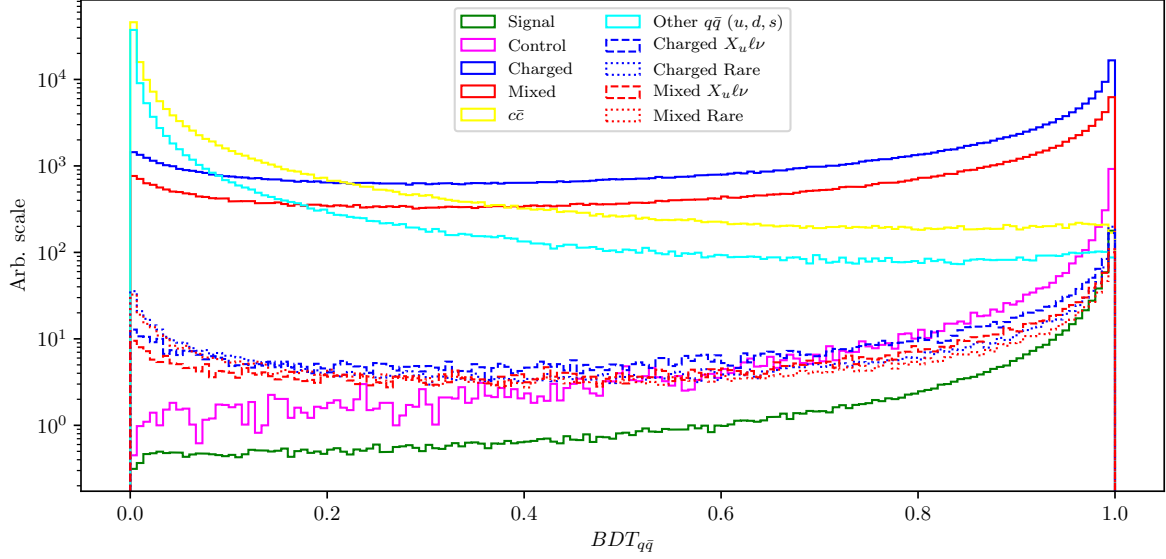


Figure 6.4: Continuum suppression classifier output for signal and various types of background. B candidates from continuum events dominate the lower region, while candidates from $B\bar{B}$ dominate in the upper region of the classifier output.

6.3 $B\bar{B}$ suppression

After separating continuum background from $B\bar{B}$ events, the next step is to train an MVA classifier to recognize our signal candidates amongst the candidates of other $B\bar{B}$ background. $B\bar{B}$ background consists of

- $b \rightarrow c\ell\nu$ background,
- $b \rightarrow u\ell\nu$ background,
- Other rare decays (radiative, penguin, rare 2- and 3-body decays, ...).

Similarly as before, the training dataset for this classifier consisted of 2×10^5 candidates, where 50 % of the candidates are correctly reconstructed signal events. The remaining

part of the training dataset consists of all background, not including the control sample, because we are not interested in suppressing it directly. The background part of the dataset consists of 75 % charged and neutral $B\bar{B}$ events in equal proportions, whereas the remaining 25 % is equally populated with charged and neutral $B\bar{B}$ events from $b \rightarrow u\ell\nu$ and other rare decays. The training dataset was proportionally sampled in the same manner as described in subsection 6.2.2.

In order to separate this kind of background, we must be careful not to introduce correlations with the fit variables (ΔE , M_{BC}) or any kind of model dependence (correlation with q^2). This means that we can not use any information of the decay particles or the candidate, which is of kinematics nature, such as decay particles momenta, decay angles or other variables with such behavior.

The training variable set consisted of

- fit probability of $P(\chi^2, DOF)$ of the signal candidate and the ROE side, separately,
- $\cos \theta_{BY}$ from Eq. (4.4),
- \cos of the angle between momentum and vertex of X , where $X \in [KK, KK\ell, KK\ell\nu]$,
- FlavorTagger variables for the two signal-side kaons,
- number of kaons, tracks and distant tracks in ROE,
- θ angle of the ROE momentum in CMS frame,
- ξ_Z from [9]
- Δz ,
- m_{miss}^2 from Eq. (4.11),
- $B \rightarrow D^*\ell\nu$ veto variables,

where distant tracks are all tracks in ROE which satisfy the condition of $|d_0| > 10.0$ cm or $|z_0| > 20.0$ cm. The last entry, $B \rightarrow D^*\ell\nu$ veto variables, are a set of variables where we partially reconstruct the D^* candidate 4-momentum via a linear combination of the π_s^\pm 4-momentum in the $D^* \rightarrow D\pi_s^\pm$ decay. It helps discard the most dominant $B \rightarrow D^*\ell\nu$ background. It is most efficient in the $B^0 \rightarrow D^{*-}\ell^+\nu$ decay, where D^{*-} further decays via $D^{*-} \rightarrow \bar{D}^0\pi_s^-$. Other decays do not contain a charged π_s particle and are harder to reconstruct with good precision. This results in larger suppression of the neutral $B\bar{B}$ background only. Figures 6.5 shows the veto variable with a partial reconstruction of a charged π_s^\pm .

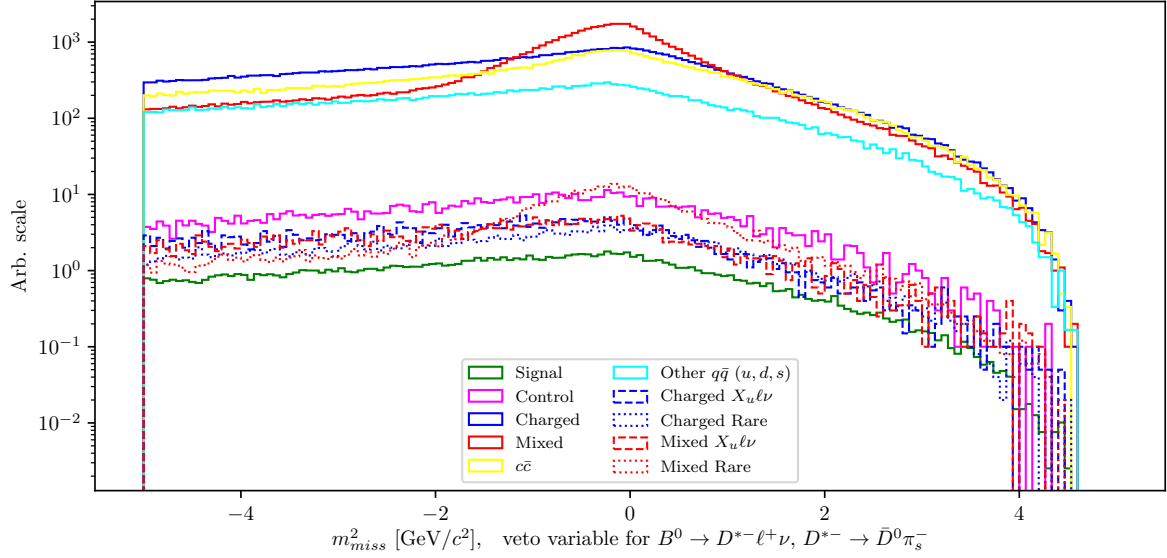


Figure 6.5: Distribution of m_{miss}^2 for partially reconstructed $B^0 \rightarrow D^{*-} \ell^+ \nu$ decays, which serves as a veto.

When the training is finished and hyper-parameters of the classifier are optimized, the classifier output, shown in Figure 6.6 (left), can be used for background suppression. B meson candidates from $B\bar{B}$ background are dominant at lower values, while candidates from $B\bar{B}$ events populate the region with higher values. Since the differences between signal and background $B\bar{B}$ events are smaller than $B\bar{B}$ and $q\bar{q}$ events, the resulting classifier has a smaller separation power than in previous section.

6.3.1 Boosting to uniformity

The selection approach with standard classifiers is optimal for counting experiments, as it by construction produces the optimal selection for observing an excess of signal over background events. Today's BDT algorithms, which work in this way, produce non-uniform selection efficiencies and may, as a consequence, shape background distributions to look like signal. In order to minimize such behavior, it is possible to discard variables, which are correlated with the variable of interest (in our case ΔE and M_{BC}), from the training set. This, however, decreases the classifiers discriminating power. Another approach is to use a novel boosting method, uBoost, which is trained to optimize an integrated FOM under the constraint that the BDT selection efficiency for the desired class must be uniform. The uBoost algorithm balances the biases to produce the optimal uniform selection [10].

The training set used in this training is the same as described in the beginning of this chapter, along with the same set of training variables. It will be seen later that the

standard BDT classifier shapes the background to look like signal mostly in the M_{BC} picture, therefore we train the uBDT classifier with a uniformity constraint in the M_{BC} variable for background candidates with the uBoost algorithm. The resulting classifier output is shown in Figure 6.6 (right). For this classifier, the separation power between signal and background seems worse, however, the shapes of backgrounds can differ and the final conclusion will be shown only after the signal extraction.

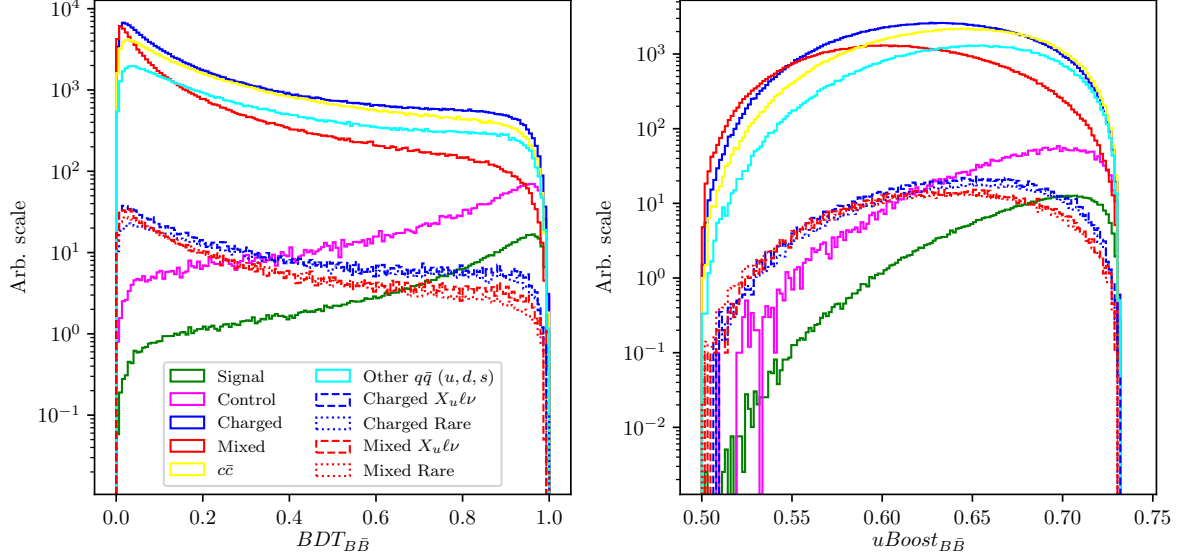


Figure 6.6: $B\bar{B}$ suppression classifier output for signal and various types of background for the standard BDT classifier (left) and the uBDT classifier (right). B candidates from $B\bar{B}$ background events dominate the lower region, while signal and control candidates dominate in the upper region of the classifier output.

6.4 Selection optimization

Instead of two separate $q\bar{q}$ and $B\bar{B}$ FOM optimizations, it is more efficient to do a simultaneous 2D FOM optimization, since the two classifiers are not completely uncorrelated. In the same manner as before, FOM is optimized for perfectly reconstructed signal candidates in the signal window, after all the pre-cuts, signal categorization, and after cutting out the background resonances and the control decay. The FOM plot with the optimal point for both $B\bar{B}$ MVA classifiers is shown in Figure 6.7.

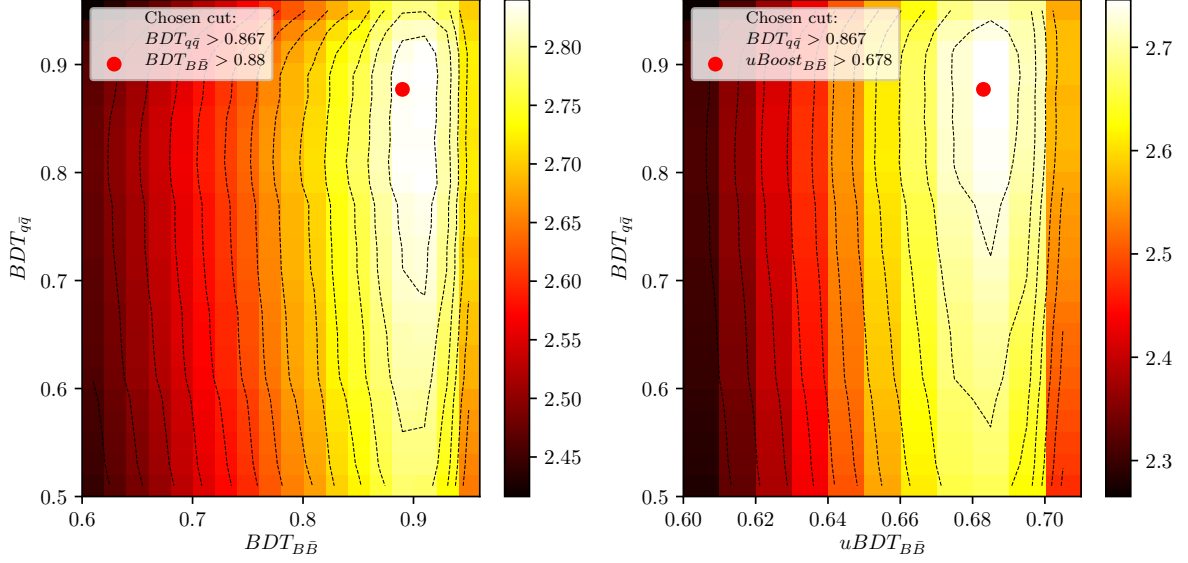


Figure 6.7: 2D FOM optimization of continuum suppression classifier and the standard BDT (left) and uBDT (right) $B\bar{B}$ suppression classifier.

We can compare signal and major background distributions of ΔE and M_{BC} after the 2D FOM optimization for both classifiers. Figure 6.8 shows the arbitrary (left) and normalized scale (right) for ΔE (top) and M_{BC} (bottom) for the final sample optimized with the standard BDT classifier, while Figure 6.9 shows similarly for the final sample optimized with uBDT classifier. We can see that there is considerably more background in the latter case, however, also shapes of background and signal distributions differ greatly. The biggest change seems to be in the shape of the M_{BC} distribution, where the background component is much more signal like in the final sample optimized with the standard BDT classifier than in the other case. The total numbers of expected signal candidates and the signal-to-noise ratios for both classifiers are:

- Standard BDT: $N_{sig} = 177.40$, $N_{sig}/N_{bkg} = 4.81 \%$,
- uBDT: $N_{sig} = 260.55$, $N_{sig}/N_{bkg} = 1.34 \%$.

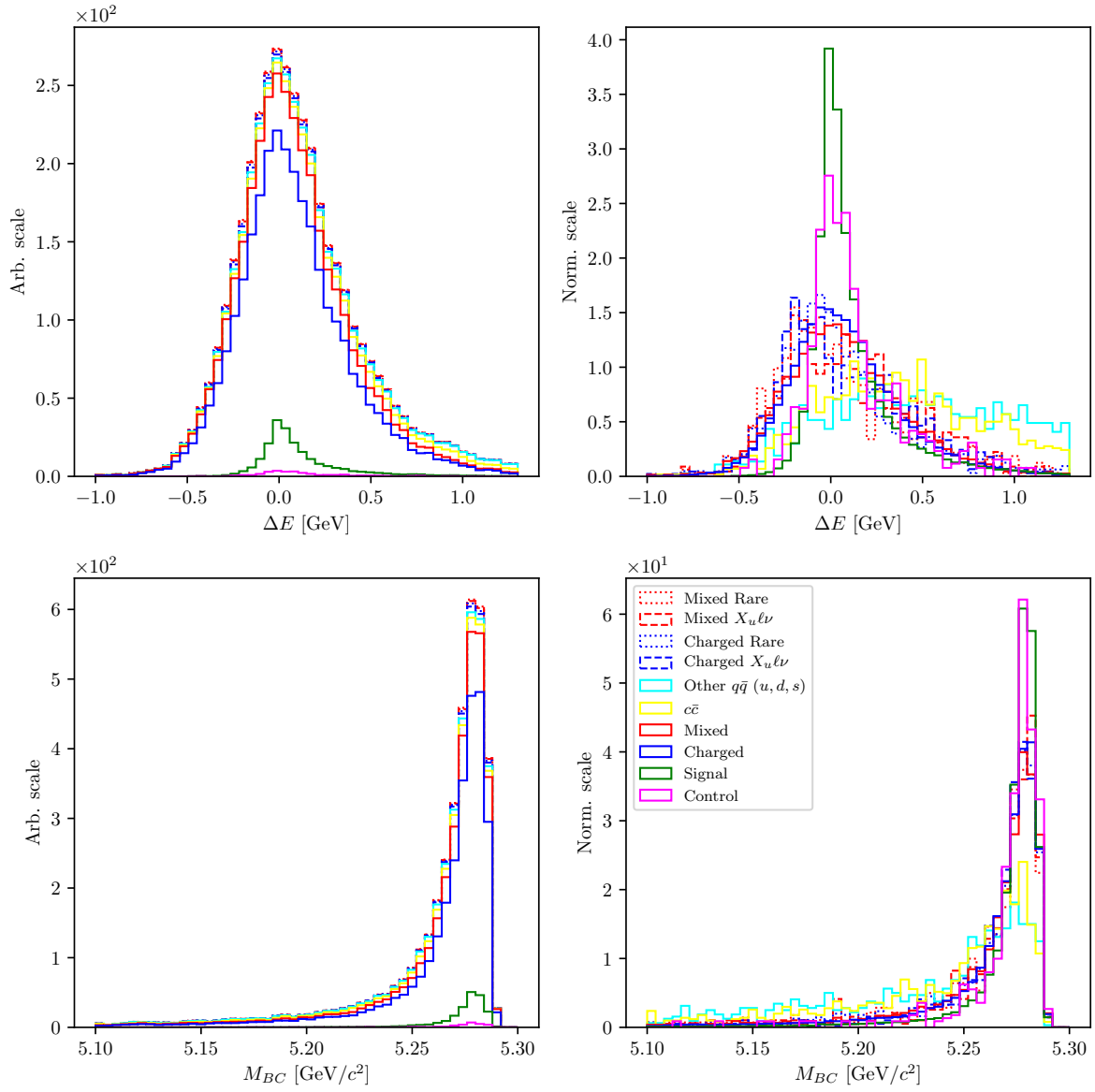


Figure 6.8: Arbitrary (left) and normalized scale (right) for ΔE (top) and M_{BC} (bottom) for the final sample optimized with the standard BDT classifier.

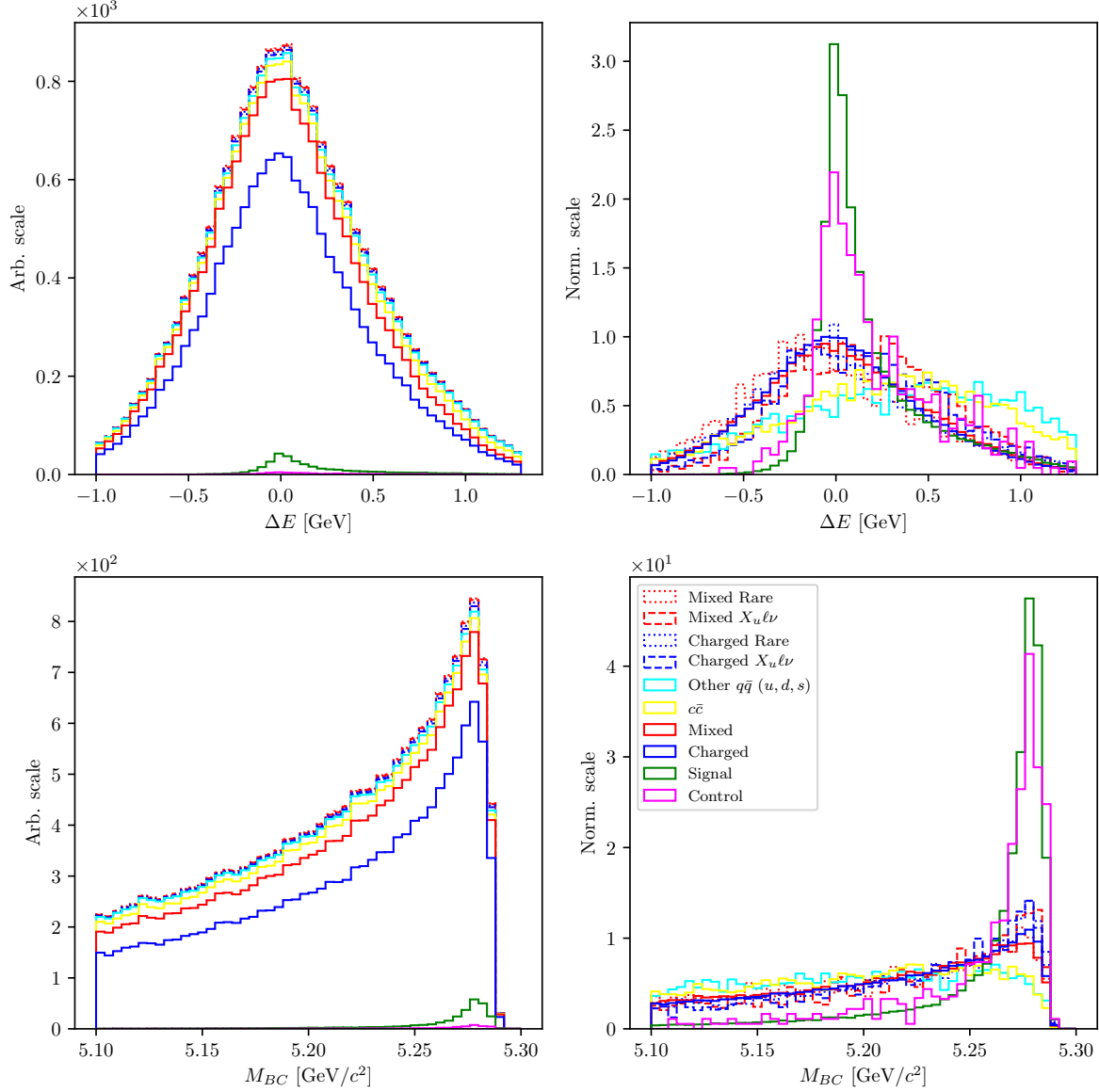


Figure 6.9: Arbitrary (left) and normalized scale (right) for ΔE (top) and M_{BC} (bottom) for the final sample optimized with the uBDT classifier.

6.5 Data and MC agreement

With the final selection in place, we can check the data and MC agreement by checking the control decay region in on- and off- resonance data. Off-resonance samples provide the ability to check the agreement of the $q\bar{q}$ background component, while on-resonance samples can be used to check the validity of the control MC sample and, consequentially,

the signal MC sample.

The off-resonance data were collected at 60 MeV below the $\Upsilon(4S)$ resonance peak energy in order to determine the non- $B\bar{B}$ background. It therefore offers a direct view of the $q\bar{q}$ background data sample, which we can compare to the off-resonance MC sample. Figure 6.10 shows ΔE , M_{BC} and the $q\bar{q}$ classifier output, $BDT_{q\bar{q}}$, for off-resonance data and MC in the control region, before any MVA cuts, where the MC sample was scaled down by a factor of 6, due to having more streams of MC. Figures show a slight and a consistent under-estimation of the $q\bar{q}$ MC sample. However, looking at the shapes of the fit distributions, the only difference seems to be the normalization factor, so the distribution shapes can be left as they are, since the normalization will be automatically set in the template fit. There also seems to be a difference in the classifier performance for the continuum background suppression on data and MC. This leads to further differences between data and MC in the $q\bar{q}$ sample after the classifier cut, but we estimate that these differences are negligible, since a relatively small amount of continuum background passes the selection, compared to other background types.

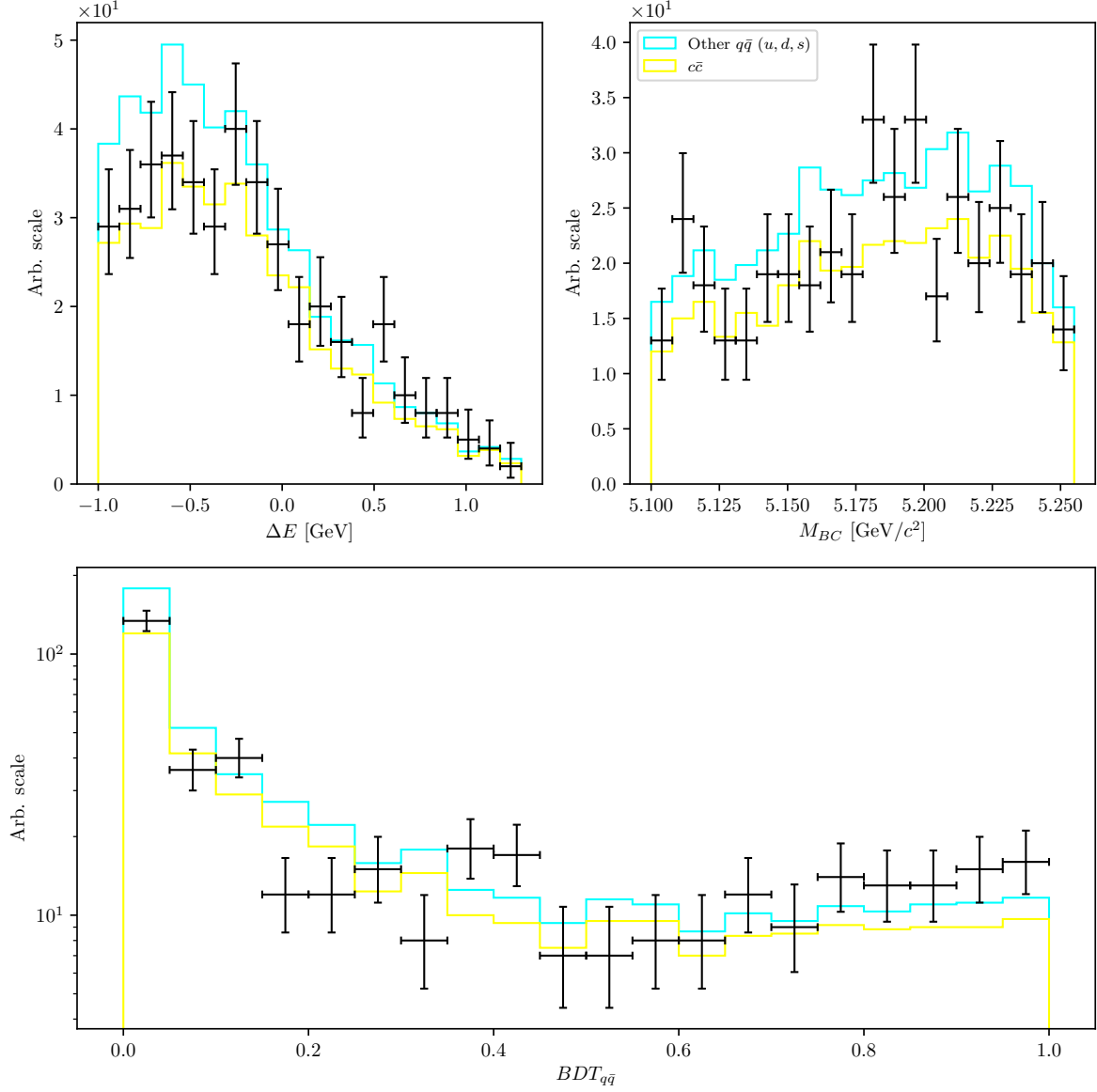


Figure 6.10: ΔE (left), M_{BC} (right) and the $q\bar{q}$ classifier output (bottom), for off-resonance data and MC in the control region before any MVA cuts.

We can repeat the check on on-resonance data. Figure 6.11 shows ΔE , M_{BC} and $BDT_{q\bar{q}}$, where one can see inconsistencies between data and MC on the lower spectrum, where continuum background is dominant. We see that MC is over-estimated in this region, most likely due to additional disagreements from other sources. On the other hand, data and MC seem to agree well in the upper part of the spectrum, where $B\bar{B}$ events are dominant. Overall, data and MC seem to agree well already off-the-shelf after all the pre-cuts and without any corrections. This means that the modeling of this MC

sample is very precise in this particular region of data and that there are no significant differences between data and MC for the control sample and the signal sample.

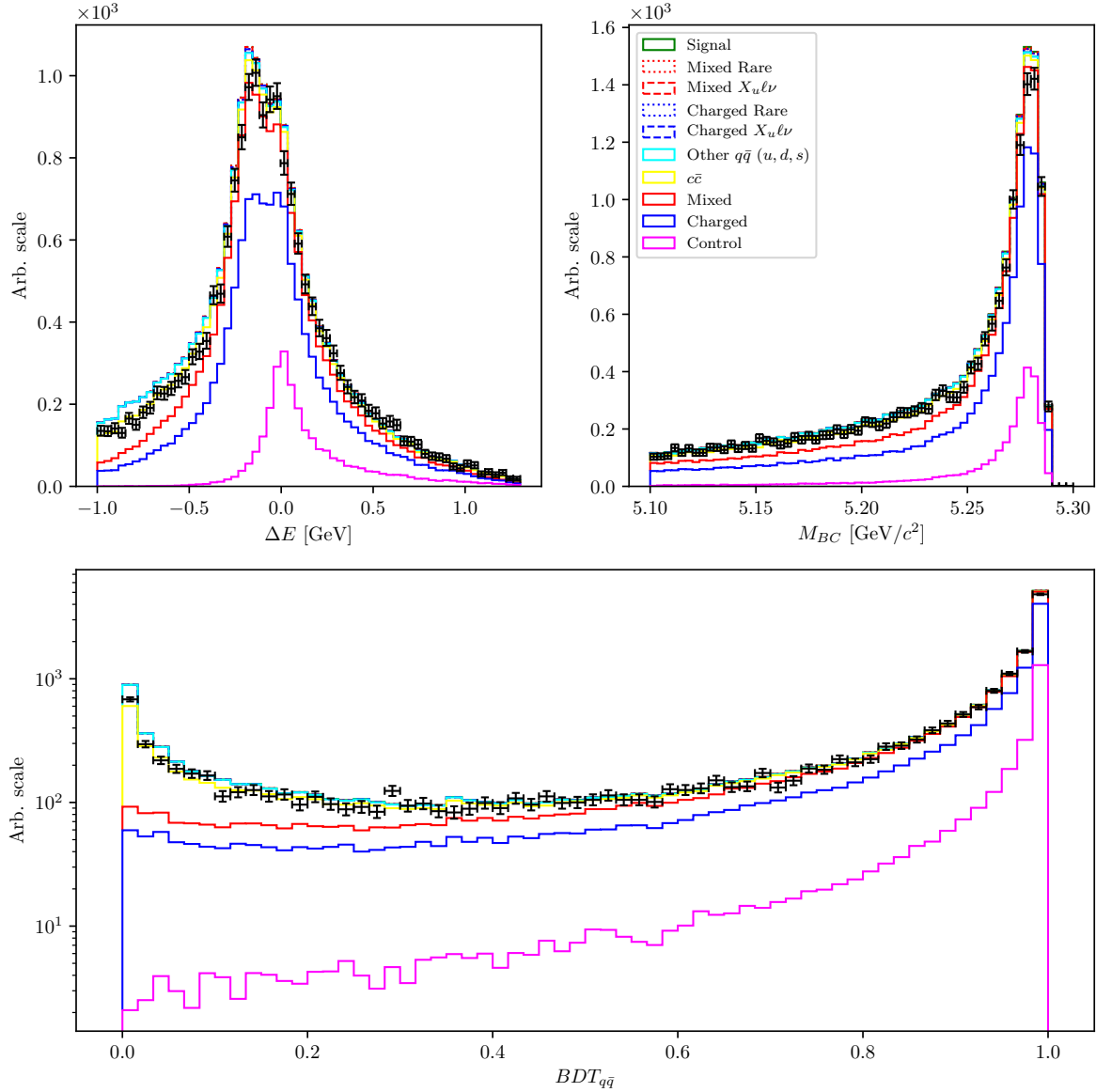


Figure 6.11: ΔE (left), M_{BC} (right) and the $q\bar{q}$ classifier output (bottom), for on-resonance data and MC in the control region before any MVA cuts.

Chapter 7

Signal extraction

In this chapter the procedure for signal yield extraction is presented. We use the framework of `RooFit` [11] where we define 2D histogram templates in ΔE and M_{BC} , based on MC, for signal and several types of background. Using these templates, the independent full sample is fitted with binned extended maximum likelihood (ML) fit, so that the individual template ratios and their sum describe the fitted sample as best as possible. In particle physics we are often dealing with low numbers of events and need to account for the Poisson nature of the data, therefore we use the likelihood fit, since it takes the Poisson errors into account, unlike the χ^2 fit, where the errors are assumed to be Gaussian. In this procedure we attempt to find the parameter values that maximize the likelihood function, given the observations.

If $P(n|\vec{\alpha})$ is the probability of measuring n candidates, where $\vec{\alpha}$ is a set of parameters on which P depends, we can define the likelihood function L for a series of such measurements (i.e., bins in histogram) n_i based on Poisson statistics as

$$L(\vec{\alpha}) = \prod_{i=1} P(n_i|\vec{\alpha}) = \prod_{i=1} \frac{\mu_i^{n_i} e^{-\mu_i}}{n_i!}, \quad (7.1)$$

where μ_i is the expected value for each measurement. It is also common to search for the minimum of the negative value of $\ln L$, or negative log-likelihood (NLL), as

$$\mathcal{L}(\vec{\alpha}) = -\ln L(\vec{\alpha}) = -\sum_i \ln \left(\frac{\mu_i^{n_i} e^{-\mu_i}}{n_i!} \right) = \sum_i \ln(n_i!) + \mu_i - n_i \ln(\mu_i). \quad (7.2)$$

Maximizing L or minimizing \mathcal{L} gives us a maximum likelihood estimate of the set of parameters $\vec{\alpha}_{ML}$ which best describe the observed data.

The ML method provides a method to estimate the fit uncertainty. This is especially useful if the log-likelihood has a non-parabolic shape, which leads to asymmetric errors. We calculate the errors using the `MINOS` algorithm from the `MINUIT` package [12], which is implemented in `RooFit`. The algorithm follows the log-likelihood function out of the minimum to find the appropriate intervals of confidence for each parameter, taking the parameter correlations into account.

To estimate the goodness of the likelihood fit, one option is to generate toy MC experiments and obtain the expected log-likelihood distribution. Likelihood fits, however, also offer another way to test the goodness of fit via the likelihood ratio (LR), where we compare the likelihood obtained under the ML parameters $\vec{\alpha}_{ML}$, to the likelihood obtained under the null hypothesis parameters $\vec{\alpha}_{H_0}$. This determines how likely the data is under one model than the other. We define the LR test as

$$\lambda = -2 \ln \left(\frac{L(\vec{\alpha}_{ML})}{L(\vec{\alpha}_{H_0})} \right) = -2 [\ln L(\vec{\alpha}_{ML}) - L(\vec{\alpha}_{H_0})] \sim \chi_q^2, \quad (7.3)$$

which asymptotically behaves as the χ_q^2 distribution with $q = m - n$ degrees of freedom, where m and n are degrees of freedom of $L(\vec{\alpha}_{ML})$ and $L(\vec{\alpha}_{H_0})$, respectively. In particle physics we usually study a specific decay and try to perform measurements of the signal yield, so the null hypothesis in this case is that we expect to observe no signal. This means that for the null hypothesis we fix the expected signal yield parameter to zero, while leaving the other parameters of $\vec{\alpha}_{H_0}$ the same as in $\vec{\alpha}_{ML}$, which results in $n = m - 1$ degrees of freedom and in their difference $q = m - n = 1$. For such a simple LR test of a single parameter the LR test then follows the χ^2 distribution with 1 degree of freedom. In this case we can define the fit significance from the χ^2 value in units of σ as

$$\text{Significance} = \sqrt{\lambda} = \sqrt{\chi^2}. \quad (7.4)$$

7.1 Fit templates

The same MC samples are used for template construction as described in Chapter 2,

- signal MC,
- 10 streams of **charged** and **mixed** $B\bar{B}$ background,
- 6 streams of $c\bar{c}$ (**charm**) and other $q\bar{q}$ (**uds**) background,
- **ulnu** sample, corresponding to $20\times$ integrated luminosity of the full Belle dataset,
- **rare** sample, corresponding to $50\times$ integrated luminosity of the full Belle dataset.

We perform 10 fits to each stream of MC, where 9 streams were used for the creation of the templates and the remaining stream was used as data. When fitting real data, all available MC was used for creating the templates. The full signal MC sample was used for the signal template definition in case of MC as well as data fits. The signal part of the **ulnu** sample was not used in template construction, it was only used as a part of the fitted sample.

7.1.1 Templates in signal fits

The following histogram templates were defined for the signal fits

- signal template,
- control template,
- $B\bar{B}$ template,
- $q\bar{q}$ template.

When fitting the signal sample, all template shapes were fixed and all template yields were left as floating parameters in the fit, except in the case of control template, where the yield was fixed to the expected MC value, since the sample size was very small and very similar to the signal template. Figures 6.8 and 6.9 show ΔE and M_{BC} distributions for the signal template for both final samples, where pronounced peaks can be seen at $\Delta E \approx 0$ GeV and $M_{BC} \approx m_B$. The remaining three templates for control, $q\bar{q}$ and $B\bar{B}$ sample all describe the background part and, with the exception of the control template, tend to be more widely distributed or even shifted from the nominal value. For the $q\bar{q}$ template the sample of $q\bar{q}$ background was used, whereas in case of the control and $B\bar{B}$ templates, they were constructed using generic $B\bar{B}$ background, along with the `rare` and `ulnu` background samples with expected relative ratios, based on MC. Figures 6.8 and 6.9 show ΔE and M_{BC} distributions for the three types of background for the final selection using the standard BDT and the $uBDT$, respectively.

The argument for merging all $B\bar{B}$ background in a single template lies in the fact that the major part of this background consists of candidates with a $K\ell$ pair from one B meson, and the remaining K from the other one. Other sources of background are present, but not very significant. All sources of $B\bar{B}$ background for the signal KK invariant mass region are shown in Figure 7.1.

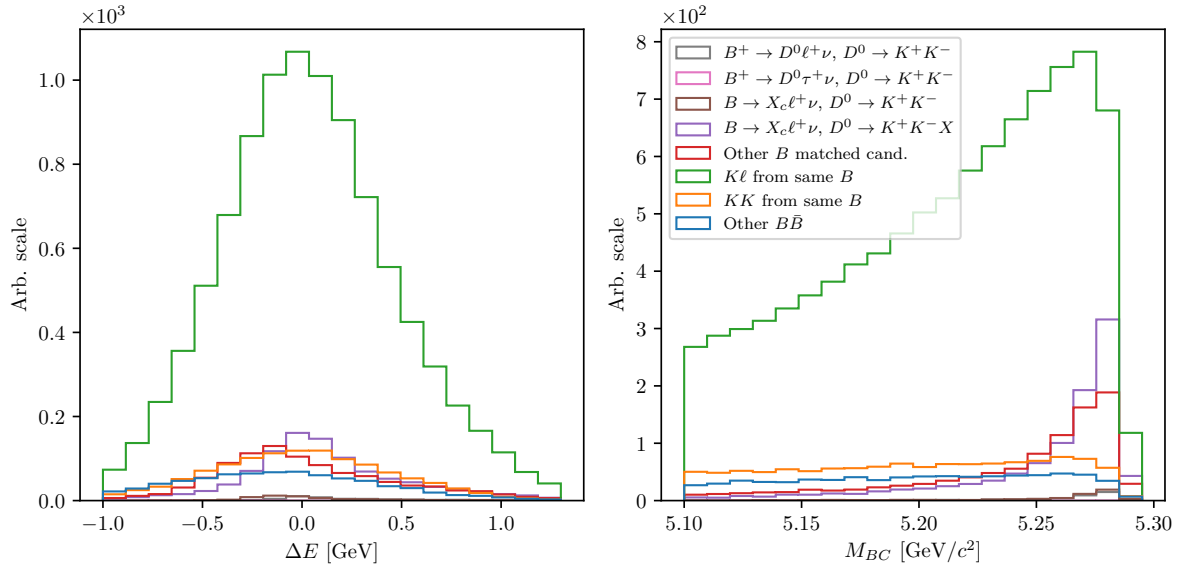


Figure 7.1: Distributions of ΔE (left) and M_{BC} (right) for various sources of the $B\bar{B}$ background after imposing the signal KK invariant mass cut. The major source of the $B\bar{B}$ background comes from candidates with a $K\ell$ pair from one B meson and the remaining K from the other one.

7.1.2 Templates in control fits

In case of control sample fits the situation is similar. The difference is that in this case the yield of the control template was left as a floating parameter, while the yield of the signal template was fixed to the expected MC value for the same reasons as mentioned before. In this case, the following fit templates are chosen

- signal template,
- control template,
- $B \rightarrow \bar{D}^* \ell^+ \nu$ template,
- other $B\bar{B}$ BKG template,
- $q\bar{q}$ template.

Since the background composition in the control region is different, we introduce a new category template for the background. All sources of $B\bar{B}$ background for the control KK invariant mass region are shown in Figure 7.2.

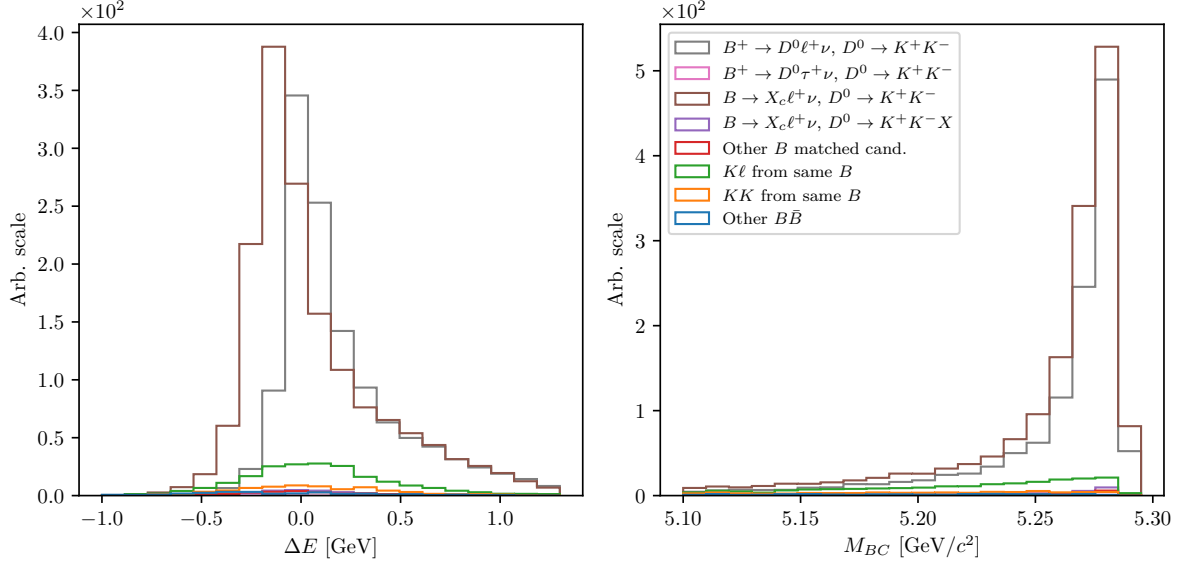


Figure 7.2: Distributions of ΔE (left) and M_{BC} (right) for various sources of the $B\bar{B}$ background after imposing the control KK invariant mass cut. The major source of the $B\bar{B}$ background comes from candidates with a $K\ell$ pair from one B meson and the remaining K from the other one.

7.2 Adaptive binning algorithm

The fit templates contain areas of low statistics, which are populated with bins with zero content. This is a direct consequence of having a finite MC sample and represent a liability in ML fits. Due to low statistic in the edge regions, the locations of these empty bins can vary for the templates and the fitted sample. A problem occurs if all templates have an empty bin where the fitted sample does not. In the scope of ML fits, this effectively means that there are entries in bins where the probability of having them is 0. We will call such bins *problematic*, because in these cases the fit does not converge.

The ideal solution for this problem would be to increase the MC statistics. Since this is not an option, we pursue other solutions, such as decreasing the number of bins. While this solves the problem, the drawback of it is a decrease in the template resolution in densely populated regions, where good resolution is most needed. The optimal solution here seems to be a choice of variable bins, with fine binning in the densely populated regions and larger bins in the regions with low statistics.

We have devised an algorithm, which compares the templates and the fitted sample, and defines a variable binning so that there are no more problematic bins in the end. Figure 7.3 shows an example of how the procedure works. The algorithm takes an argument

1149 for the initial number of uniform bins in each dimension, and does the following

- 1150 1. define uniform binning in both dimensions with the provided argument,
- 1151 2. create a 2D histogram from MC templates with expected yields,
- 1152 3. define an *optimal* region, where most of the 2D integral is contained and where all
- 1153 bins have a non-zero content (this region does not change throughout the process),
- 1154 4. compare the histograms for the expected and the fitted sample, find the problem-
- 1155 atic bins,
- 1156 5. loop until all problematic bins disappear

- 1157 a) find problematic bin, which is nearest to the maximum bin,
- 1158 b) change the binning from N to $N - 1$ from that bin and in the direction away
- 1159 from the maximum bin.

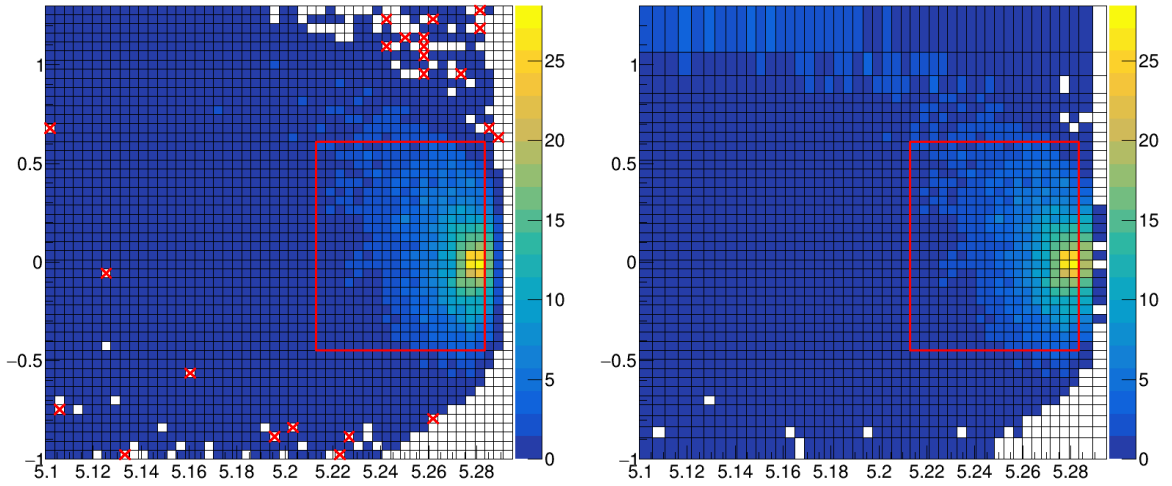


Figure 7.3: Steps taken in the adaptive binning algorithm. Left image shows the initial 2D histogram with the defined optimal region and the problematic bins, the right image shows the final binning with the unchanged optimal region, while the problematic bins are gone due to the new binning choice.

1160 An additional problem occurs in the plotting of the fitted templates and the sample with
 1161 variable binning. It would seem that RooFit does not take the bin widths into account
 1162 when plotting, while everything works as expected for the fit itself. This was bypassed
 1163 by extracting the fitted yields and applying them to templates and samples with uniform

binning, which were then used for drawing.

7.3 Signal MC fit results

The fit setup was used on the final samples obtained with both versions of the final selection (standard BDT and uBDT). The choice of the initial uniform binning is not obvious, so we perform fits to all streams of MC for each initial binning choice and the fitted and expected yield difference, pulls and fit significance for both final samples, shown in Figure 7.4. Fits to final sample, obtained with the uBDT classifier generally seem to have a lower bias, pull distributions closer to the normal distribution and better significance than the fits in the case of the standard BDT final sample. This fixes our choice of the final selection. It is also possible to determine the optimal initial binning choice to be somewhere in the region of 20 bins in each dimension, since a higher number of initial bins yields biased results, while a lower one yields results with poorer significance.

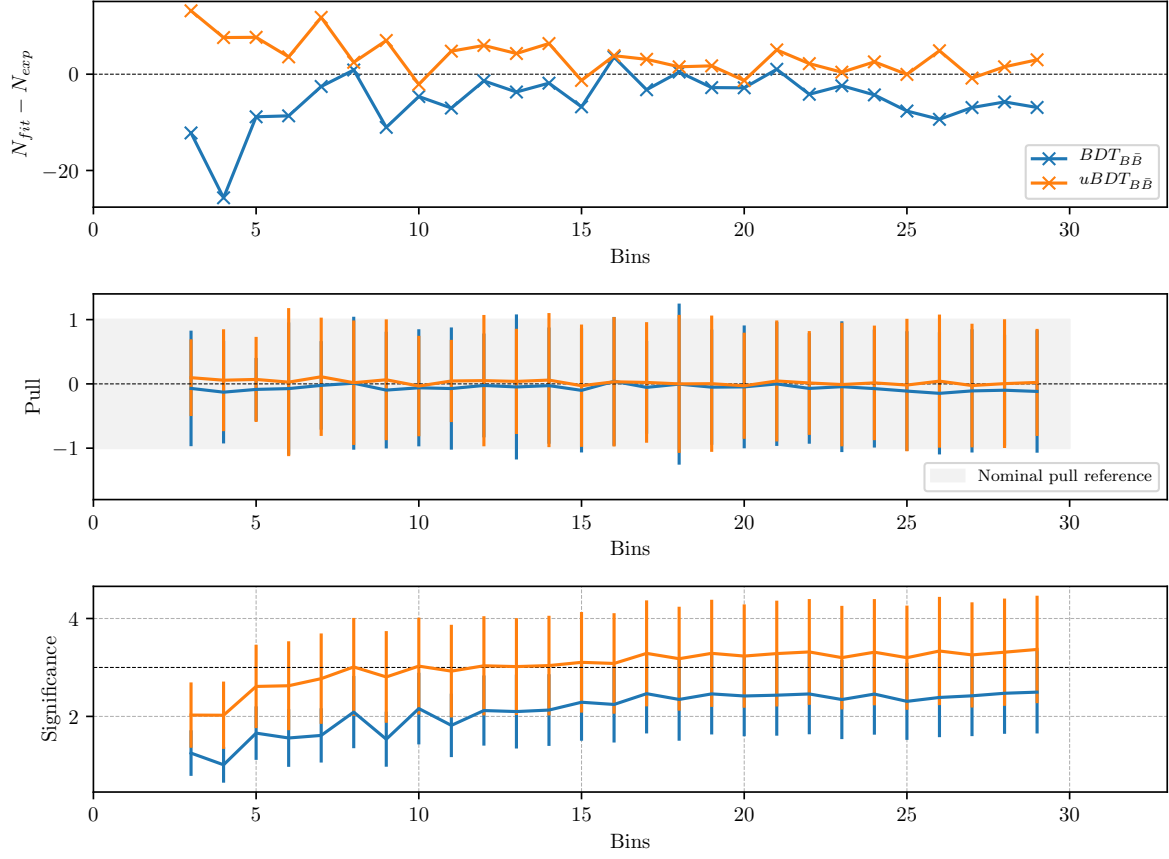


Figure 7.4: Fitted yield and expected yield difference (top), pulls (center) and fit significance (bottom) as a function of binning in ΔE and M_{BC} for the final sample, optimized with the standard BDT classifier (blue) and the uBDT classifier (orange).

Figure 7.5 shows the fit result and the fitted sample of an arbitrary stream for ΔE and M_{BC} , for the fit region and for the signal region. The fits seem stable and fit errors are under control. Fit results for all streams of MC are shown in Figure 7.6, along with the global fit of a zero degree polynomial over all streams. The results seem to describe the expected value in a precise manner, with the bias much smaller than the average statistical error. The normalized χ^2 value with $10 - 1 = 9$ degrees of freedom of the global fit is $\chi_9^2 = 0.9$, while the average significance of the fits is around 3.178σ .

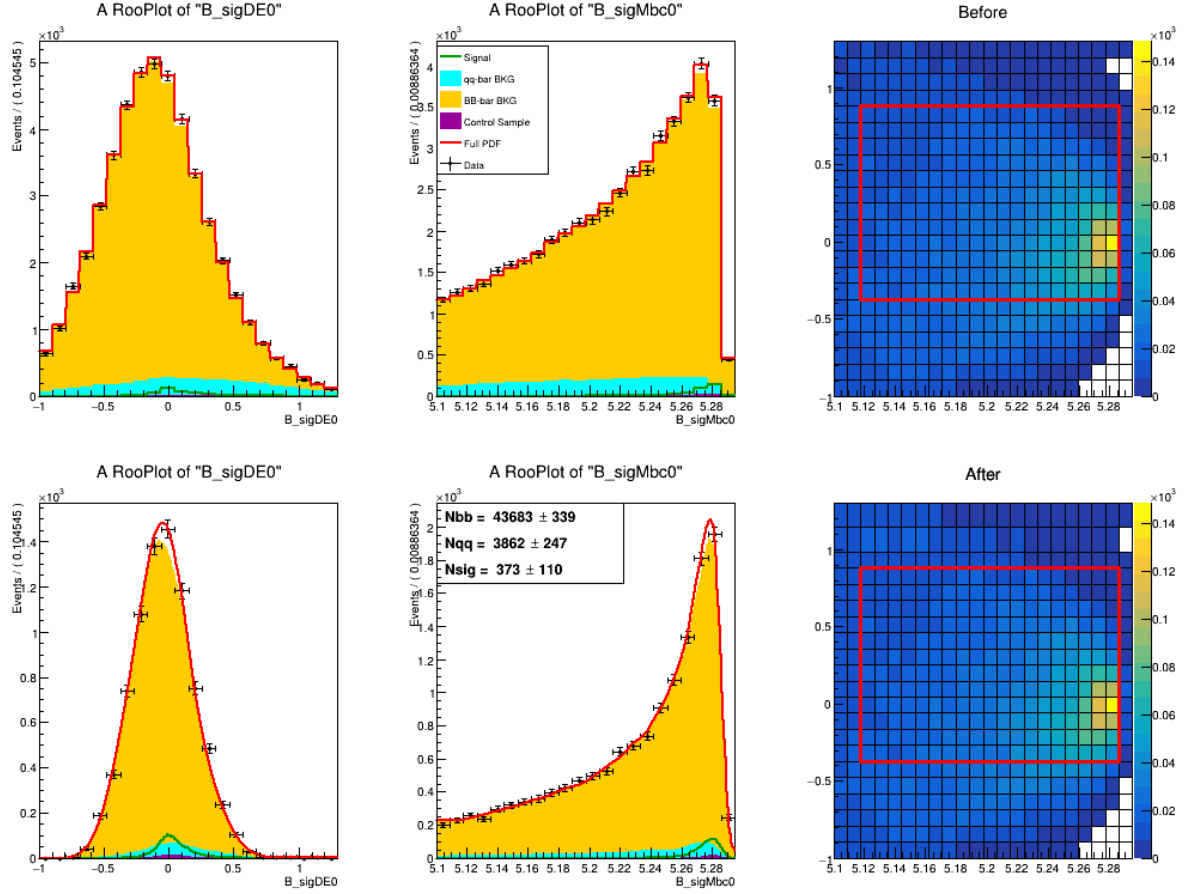


Figure 7.5: An example fit to one stream of MC. Left column shows the M_{BC} and the center column shows the ΔE distribution of the full fitted sample in the full fit region (top) and the signal region (bottom). The right column shows the expected 2D histogram in ΔE and M_{BC} with initial uniform binning (top) and the variable binning (bottom) after the binning algorithm.

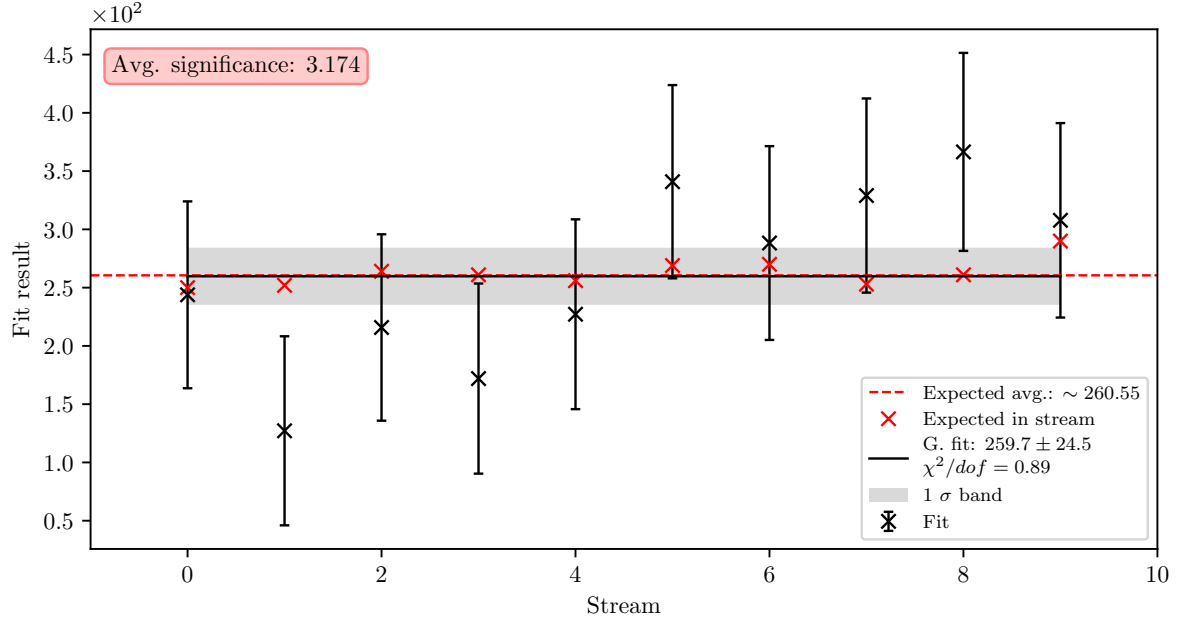


Figure 7.6: Fits to all 10 streams of MC and the global fit with a zero degree polynomial. The red like shows the mean value of the global fit and the green band shows the 1σ confidence interval. The expected value here differs slightly from the values in Section 6.4, since it is evaluated on a 10 stream sample size of the $20 \times L_0$ ulnu sample.

7.3.1 Toy MC experiment

Toy MC experiments allow us to study the yields, errors and the pulls of the signal fit by generating our own pseudo datasets, according to the MC, and not producing it in the standard way, which consumes unaffordable amounts of CPU time. In order to test the fit behavior, a toy MC study was performed where all available MC was used for template creation. We constructed 3×10^3 pseudo datasets, where each dataset was generated expected amount of each template category, distributed according to the Poisson distribution. All fits were performed with the optimal initial uniform binning of 20×20 bins in ΔE and M_{BC} .

Figure 7.7 shows distributions of the fit yields, errors and the pull distribution of all pseudo fits. The fits seem to be under control since there is not any significant bias, and the pulls follow a normal distribution with a mean of $(1.1 \pm 1.8) \times 10^{-2}$ and standard deviation of (1.013 ± 0.013) . The mean (\bar{X}) and the standard deviation (S) were calculated in the usual way, while the errors of these statistics were obtained by calculating

the standard error of the mean ($\sigma_{\bar{X}}$) and standard deviation (σ_S), taken from [13], as

$$\sigma_{\bar{X}} = \frac{S}{\sqrt{N}}, \quad \sigma_S = \frac{S}{\sqrt{2(N-1)}}, \quad (7.5)$$

where N is the number of performed measurements.

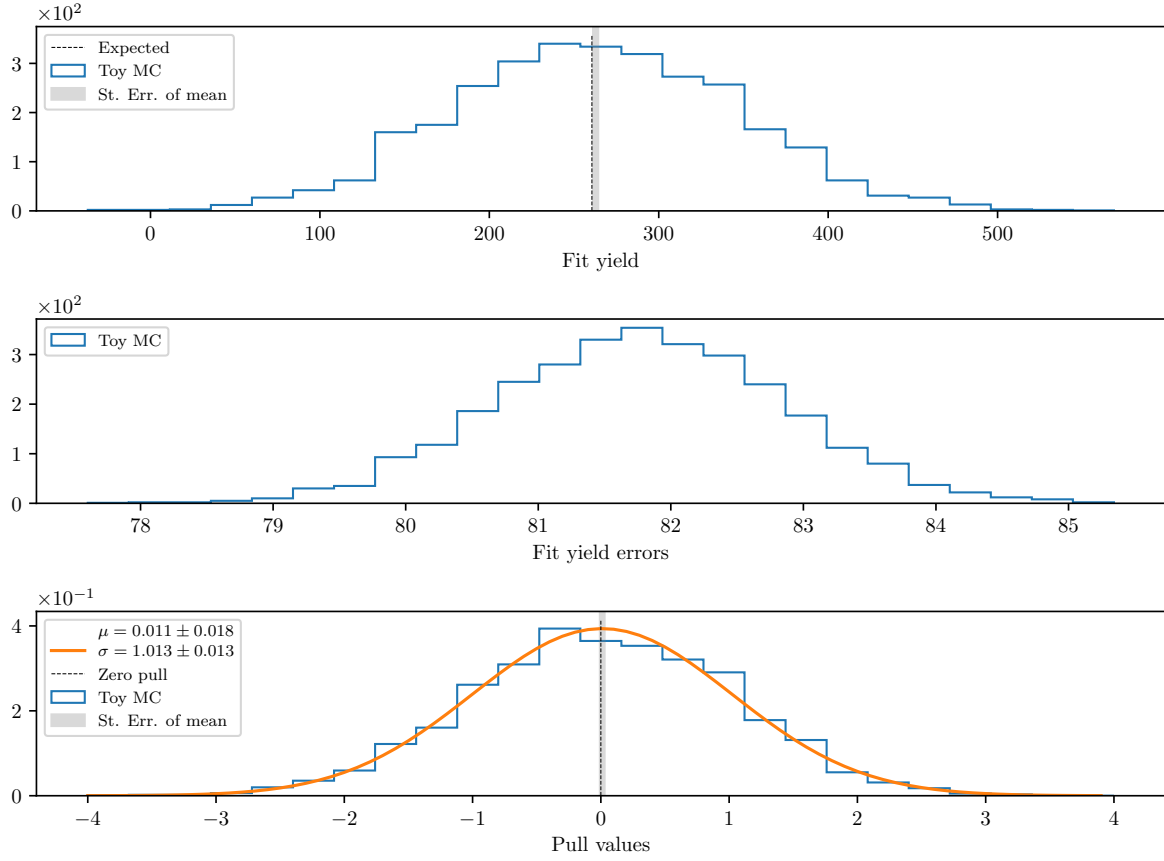


Figure 7.7: Toy MC fits of pseudo data showing the fit yield (top), fit errors (center) and the pull distribution of the fits (bottom).

7.3.2 Toy MC linearity test

Linearity test is used for determining sensitivity of the fit to the amount of signal in the fitted sample. Since this is a first measurement of this decay channel, MC modeling is not reliable and could be very different from reality, so we need to perform this test in order to determine our sensitivity to smaller, as well as larger amounts of expected signal.

1206 The pseudo datasets are generated in the same way as in the previous subsection, with
 1207 the exception of signal, which is generated with various amounts. 50 steps from [0.1, 10]
 1208 in the logarithmic scale are taken for fractions of signal amount and for each fraction we
 1209 generate 500 pseudo datasets according to Poisson statistics.

1210 Figure 7.8 shows the mean fit yield and expected yield difference, mean pull and the
 1211 mean significance at each signal fraction value. The expected MC result is shown at
 1212 fraction value 1. The plots show no significant bias with respect to the signal
 1213 fraction, while the pulls seems to be described by the normal distributions throughout
 1214 the fraction range. At expected value we are at about 3.2σ significance, as already
 1215 pointed out at the beginning of this section.

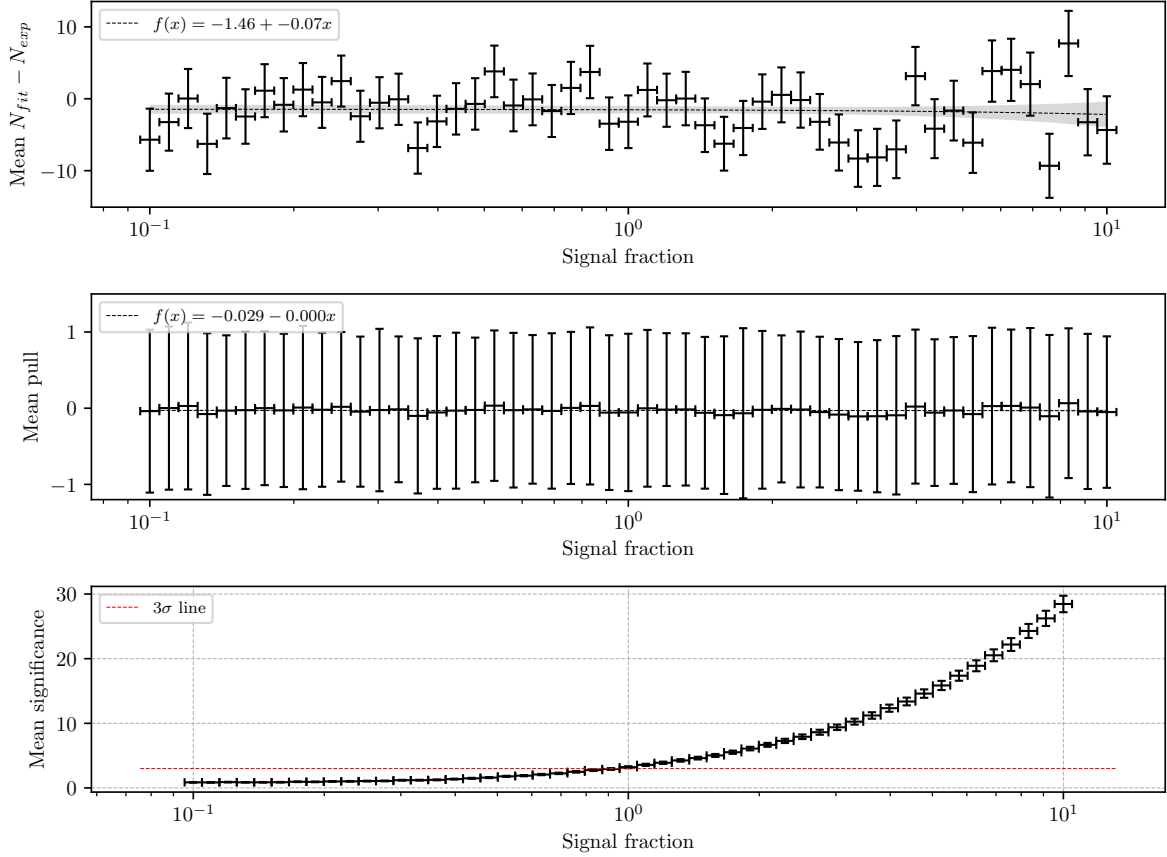


Figure 7.8: Mean fit yield and expected yield difference (top), mean pull (center) and mean significance (bottom) as a function of signal fraction.

7.4 Control fit results

A similar fit procedure as in Section 7.3 is applied in the case of the control decay on MC. In case of fits to real data, several corrections and constraints are applied before performing the fit

- a smearing factor to all MC templates,
- an offset to all MC templates

7.4.1 Smearing and offset parameters

With simulated data we are able to perform detailed studies prior to looking at measured data. However, simulated data often does not describe data perfectly. Out of variables ΔE and M_{BC} , ΔE is especially prone to a lack of precision in energy measurements. This can introduce either overestimation of resolution on MC as well as a possible shift in the measured energy in either direction. Due to this fact, we perform a scan over additional 2 parameters of offset and smearing, applied on the ΔE variable. In case of the M_{BC} variable the mentioned effects are not as prominent, so the smearing and offset for the latter variable are omitted.

Ratio constraint

Introducing a smearing and offset factor can lead to unphysical global minima in the negative log-likelihood, where we mold a single MC template to almost perfectly describe data, while other contributions are rejected by the fit. In order to bypass this problem, we fix the ratio between the $B \rightarrow \bar{D}^* \ell \nu$ sample and the control sample to the expected MC value in case of the MC fit, and to a corrected expected MC value for the data fit, where the corrections to the appropriate measured branching ratios are applied. In the latter case the constraint is applied in the form of a Gaussian function with the mean at the calculated value and with the width according to the appropriately propagated error.

The expected MC ratio and the corrected ratio are calculated as

$$\eta_{MC} = \frac{N_{B \rightarrow \bar{D}^* \ell \nu}^{MC}}{N_{\text{control}}^{MC}}, \quad (7.6)$$

$$\eta_{DATA} = \frac{N_{B^+ \rightarrow \bar{D}^{*0} \ell^+ \nu}^{MC} \times \rho_{B^+ \rightarrow \bar{D}^{*0} \ell^+ \nu} + N_{B^0 \rightarrow D^{*-} \ell^+ \nu}^{MC} \times \rho_{B^0 \rightarrow D^{*-} \ell^+ \nu}}{N_{\text{control}}^{MC} \times \rho_{B^+ \rightarrow \bar{D}^0 \ell^+ \nu}}, \quad (7.7)$$

where each ρ_X is defined as

$$\rho_X = \frac{\mathcal{B}_{PDG}(X)}{\mathcal{B}_{GEN}(X)},$$

where the appropriate branching ratio values \mathcal{B}_{PDG} and \mathcal{B}_{GEN} are values taken from the PDG [14] and values used in MC generation, respectively. Table 7.1 shows the corresponding values of all mentioned branching ratios.

Decay mode	\mathcal{B}_{PDG}	\mathcal{B}_{GEN}
1) $B^+ \rightarrow \bar{D}^{*0} \ell^+ \nu$	$(5.25 \pm 0.12) \times 10^{-2}$	5.79×10^{-2}
2) $B^0 \rightarrow D^{*-} \ell^+ \nu$	$(4.88 \pm 0.11) \times 10^{-2}$	5.33×10^{-2}
3) $B^+ \rightarrow \bar{D}^0 \ell^+ \nu$	$(2.29 \pm 0.10) \times 10^{-2}$	2.31×10^{-2}
4) $D^0 \rightarrow K^+ K^-$	$(3.97 \pm 0.07) \times 10^{-3}$	3.90×10^{-3}
Control 3) \times 4)	$(9.10 \pm 0.42) \times 10^{-5}$	9.01×10^{-5}

Table 7.1: Generated and PDG branching ratios of several decay modes.

Finally, after calculating the ratio and propagating the statistical errors and errors of the measurements, we obtain

$$\begin{aligned}\eta_{MC} &= 1.41, \\ \eta_{DATA} &= 1.29 \pm 0.06,\end{aligned}$$

where errors of all terms in Eq. (7.7) were assumed to be uncorrelated, except for errors of $\rho_{B^+ \rightarrow \bar{D}^{*0} \ell^+ \nu}$ and $\rho_{B^0 \rightarrow D^{*0} \ell^+ \nu}$, where we assumed 100% correlation, due to both values being obtained from the same measurement, assuming isospin symmetry [X].

Determination of optimal parameters

After fixing the ratio defined in previous subsection, we scan the following phase space

- smearing factor in range $[0.0, 0.08]$ GeV in steps of 8×10^{-3} ,
- offset in range $[0.0, 0.003]$ GeV in steps of 1.5×10^{-3} ,

where for each parameter pair the likelihood ratio test is performed to estimate the goodness of the fit. Figure 7.9 shows the contour plot of the likelihood test ratio λ , as defined in Eq. (7.3), for 2 d.o.f., for MC (left) and data (right). The scan over MC serves the purpose of a consistency check, where we expect the best fit to occur in the phase space where neither smearing nor offset are applied. In case of data, we see that we obtain a better fit by introducing some level of smearing and offset. The likelihood

ratio test allows us to estimate the parameter values in the 1σ confidence interval, where we obtain the optimal parameter set

- Smearing: $24 \text{ MeV} \pm X$,

- Offset: $6 \text{ MeV} \pm X$.

We apply this transformation to our MC samples in all cases when we fit real data.

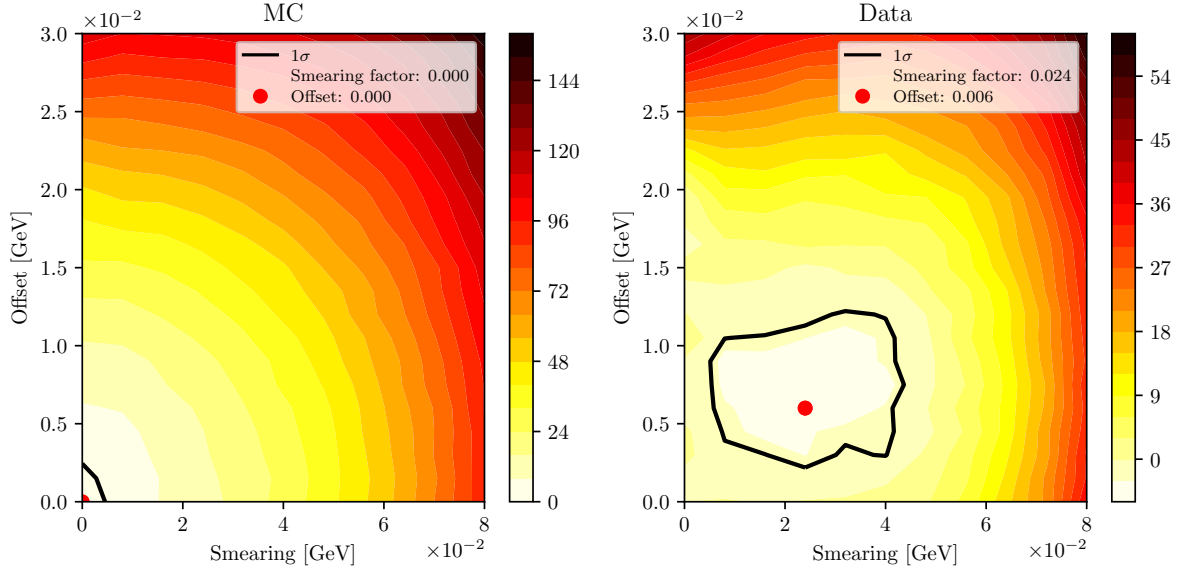


Figure 7.9: Mean fit yield and expected yield difference (top), mean pull (center) and mean significance (bottom) as a function of signal fraction.

7.4.2 Consistency of MVA cuts

Control sample fits allow us to check the behavior of optimized MVA cuts on MC as well as data and see if any of the MVA steps introduce a possible disagreement between the two. We compare control yields, their ratios and ratios of cut efficiencies (double ratios). The following cut scenarios are studied

- final selection before any MVA step,
- (a) + $BDT_{q\bar{q}}$ cut,
- (a) + $uBDT_{B\bar{B}}$ cut,
- (a) + $BDT_{q\bar{q}}$ + $uBDT_{B\bar{B}}$ cut (final selection).

1272 The same binning was chosen as in the case of signal MC fits. The results for control
 1273 fit yields, their ratios and double ratios are shown in Figure 7.10. The plot shows that
 1274 yield ratios and cut efficiency ratios are consistent with 1. This means that, for the
 1275 control sample, data and MC are in agreement before as well as after applying the final
 1276 selection cuts. This is an important check for the signal decay mode, since, this check
 1277 serves as an argument that the final selection is not over-optimized to signal MC.

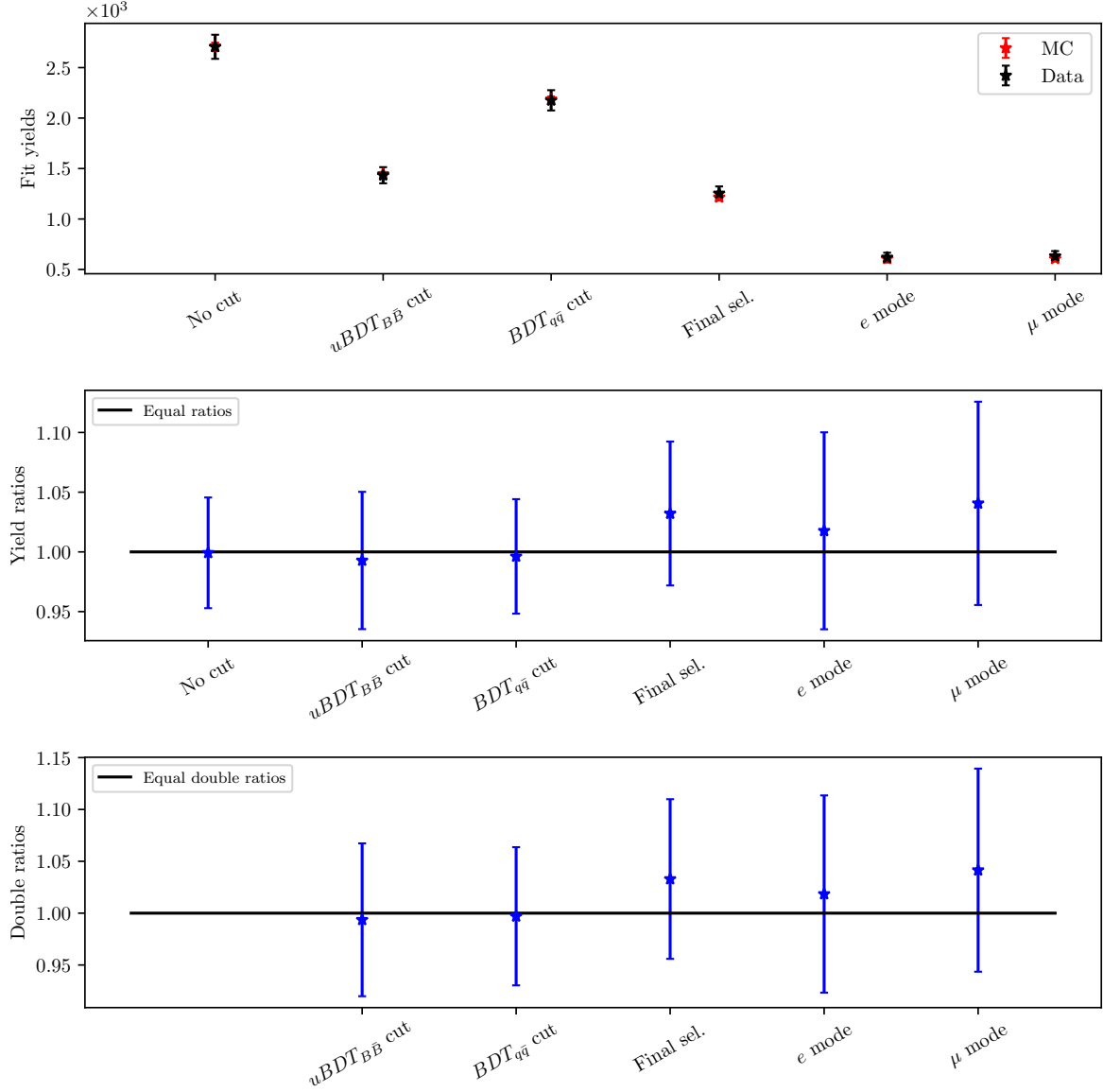


Figure 7.10: Fit yields, their ratios and ratios of cut efficiencies (double ratios) for the control sample fits to data and MC.

7.4.3 Control decay branching ratio measurement

After acquiring the fit results on MC and data we are able to determine the branching ratio of the control decay on MC and data, which are defined as

$$\mathcal{B}_{\text{control}}^{MC} = \frac{N_{\text{control}}^{\text{MC}} \times \epsilon_{MC}}{2N_{B\bar{B}}^{MC}}, \quad (7.8)$$

$$\mathcal{B}_{\text{control}} = \frac{N_{\text{control}} \times \epsilon_{MC} \times \rho_{PID}}{2N_{B\bar{B}}}, \quad (7.9)$$

where $N_{\text{control}}^{\text{MC}}$ and N_{control} are yields of the control fit on MC and data, ϵ_{MC} is the MC efficiency of the control sample, ρ_{PID} the PID correction factor, and $N_{B\bar{B}}^{MC}$ and $N_{B\bar{B}}$ are the numbers of $B\bar{B}$ meson pairs on MC and in data, respectively. The factor of 2 in the denominator comes from the fact that there are 2 B mesons in each B meson pair ($\times 1/2$), where only about 50% of the B meson pairs are charged B^+B^- meson pairs ($\times 2$), and from the fact that we are interested in the branching ratio to the lepton final state of either e or μ , and not their sum ($\times 1/2$).

The control sample efficiency was determined on a separate signal MC sample of the control decay, where we generated 5×10^6 $B^+\bar{B}^-$ pairs, with one B always decaying via $B^+ \rightarrow \bar{D}^0 \ell^+ \nu$, $D^0 \rightarrow K^+ K^-$. After applying the final selection, the full and split efficiencies with regard to the lepton final state were determined to be

$$\begin{aligned} \epsilon_{MC} &= (8.89 \pm 0.04) \times 10^{-3}, \\ \epsilon_{MC}^e &= (4.40 \pm 0.03) \times 10^{-3}, \\ \epsilon_{MC}^\mu &= (4.49 \pm 0.03) \times 10^{-3}, \end{aligned}$$

where the efficiency error was estimated based on a formula from [X]

$$\epsilon_{MC} = \frac{1}{N} \sqrt{n(1 - \frac{n}{N})},$$

where n is a subset of the full set N .

The PID correction factor is obtained by taking into account the known PID efficiency differences between data and MC. It is described in detail in X and is determined to be

$$\rho_{PID} = 0.99 \pm 0.02$$

for the e and μ mode, as well both of them together.

The number of $B\bar{B}$ meson pairs can be counted on MC and has been measured for data [X]. The values are

$$N_{B\bar{B}}^{MC} = 765.98 \times 10^6,$$

$$N_{B\bar{B}} = (771.58 \pm 10.56) \times 10^6.$$

1288 The yields of control sample candidates and their errors were taken from the fits to MC
 1289 and data. In case of MC, the fit results were averaged over 10 streams, which results in
 1290 a smaller error. The fit results after the final selection are shown in Table 7.2.

	N^{MC}	N^{data}
$\ell = e \text{ or } \mu$	1214.76 ± 22.76	1245.38 ± 69.73
$\ell = e$	607.59 ± 15.18	602.74 ± 47.32
$\ell = \mu$	607.34 ± 12.39	631.70 ± 50.06

Table 7.2: Control sample fit results for MC and data for various lepton final state modes.

1291 Finally, we can determine the branching ratios based on the calculations in Eq. (7.9).
 1292 The obtained values are shown in Table 7.3 and graphically shown in Figure X, along with
 1293 the MC generated value and the current PDG world average. Both MC and measured
 1294 determination of the control decay branching ratio are in agreement with the expected
 1295 and the world average values.

\mathcal{B}_{PDG}	$(9.10 \pm 0.42) \times 10^{-5}$	
\mathcal{B}_{GEN}	9.01×10^{-5}	
	\mathcal{B}^{MC}	$\mathcal{B}^{\text{data}}$
$\ell = e \text{ or } \mu$	$(8.92 \pm 0.17) \times 10^{-5}$	$(9.17 \pm 0.56) \times 10^{-5}$
$\ell = e$	$(9.02 \pm 0.23) \times 10^{-5}$	$(9.01 \pm 0.75) \times 10^{-5}$
$\ell = \mu$	$(8.82 \pm 0.19) \times 10^{-5}$	$(9.17 \pm 0.77) \times 10^{-5}$

Table 7.3: Control sample fit results for MC and data for various lepton final state modes.

1296 PLOT

1297 7.5 Signal fit to data

1298 Chapter 8

1299 Systematics

1300 8.1 Model uncertainty effects

1301 8.2 PID efficiency correction

1302 8.3 Bias

Bibliography

- [1] N. Cabibbo. “Unitary symmetry and leptonic decays”. In: *Physical Review L* 10.12 (1963), p. 531.
- [2] M. Kobayashi and T. Maskawa. “CP-violation in the renormalizable theory of weak interaction”. In: *Progress of Theoretical Physics* 49.2 (1973), pp. 652–657.
- [3] Y. Amhis et al. “Averages of b -hadron, c -hadron, and τ -lepton properties as of summer 2016”. In: *Eur. Phys. J. C* 77.12 (2017), p. 895. DOI: [10.1140/epjc/s10052-017-5058-4](https://doi.org/10.1140/epjc/s10052-017-5058-4). arXiv: [1612.07233](https://arxiv.org/abs/1612.07233) [hep-ex].
- [4] P. Gambino et al. “Inclusive semileptonic B decays and the determination of $|V_{ub}|$ ”. In: *JHEP* 10 (2007), p. 058. DOI: [10.1088/1126-6708/2007/10/058](https://doi.org/10.1088/1126-6708/2007/10/058). arXiv: [0707.2493](https://arxiv.org/abs/0707.2493) [hep-ph].
- [5] T. Sjöstrand, S. Mrenna, and P. Skands. “PYTHIA 6.4 physics and manual”. In: *Journal of High Energy Physics* 2006.05 (2006), p. 026.
- [6] T. Keck. “Machine learning algorithms for the Belle II experiment and their validation on Belle data”. Karlsruher Institut für Technologie, Diss., 2017. Dr. Karlsruher Institut für Technologie, 2017, 240 pages. URL: <https://ekp-invenio.physik.uni-karlsruhe.de/record/48940>.
- [7] D. Asner et al. “Search for exclusive charmless hadronic B decays”. In: *Physical Review D* 53.3 (1996), p. 1039.
- [8] A. Bevan et al. “The physics of the B factories”. In: *The European Physical Journal C* 74.11 (2014), p. 3026.
- [9] P. del Amo Sanchez et al. “Study of $B \rightarrow \pi l \nu$ and $B \rightarrow \rho l \nu$ decays and determination of $|V_{ub}|$ ”. In: *Phys. Rev. D* 83 (3 2011), p. 032007. DOI: [10.1103/PhysRevD.83.032007](https://doi.org/10.1103/PhysRevD.83.032007). URL: <https://link.aps.org/doi/10.1103/PhysRevD.83.032007>.
- [10] J. Stevens and M. Williams. “uBoost: A boosting method for producing uniform selection efficiencies from multivariate classifiers”. In: *Journal of Instrumentation* 8.12 (2013), P12013.
- [11] W. Verkerke and D. Kirkby. “The RooFit toolkit for data modeling”. In: *Statistical Problems in Particle Physics, Astrophysics and Cosmology*. World Scientific, 2006, pp. 186–189.
- [12] F. James. “MINUIT Function Minimization and Error Analysis: Reference Manual Version 94.1”. In: (1994).

- 1335 [13] S. Ahn and J. A. Fessler. “Standard errors of mean, variance, and standard de-
1336 viation estimators”. In: *EECS Department, The University of Michigan* (2003),
1337 pp. 1–2.
- 1338 [14] M Tanabashi. “Review of particle physics”. In: *Phys. Rev. D* 98 (2018), p. 030001.

A: MVA control plots

Hadronic decay MVA training

Variable importance

	Name	Alias	Importance
0	B_qpKinLepton	v_0	0.510
1	B_qpIntermediateKinLepton	v_1	0.170
2	B_nLepInROE	v_2	0.151
3	B_qpIntermediateElectron	v_3	0.031
4	B_qpMuon	v_4	0.026
5	B_ROE_PThetacms0	v_5	0.020
6	B_nROEDistTrk	v_6	0.020
7	B_qpElectron	v_7	0.019
8	B_ROECharge0	v_8	0.018
9	B_qpIntermediateMuon	v_9	0.013
10	B_nROETrk0	v_{10}	0.010
11	B_TagVPvalue	v_{11}	0.007
12	B_nKaonInROE	v_{12}	0.004

Table 8.1: Variable names, aliases and importance in the scope of hadronic decay MVA training.

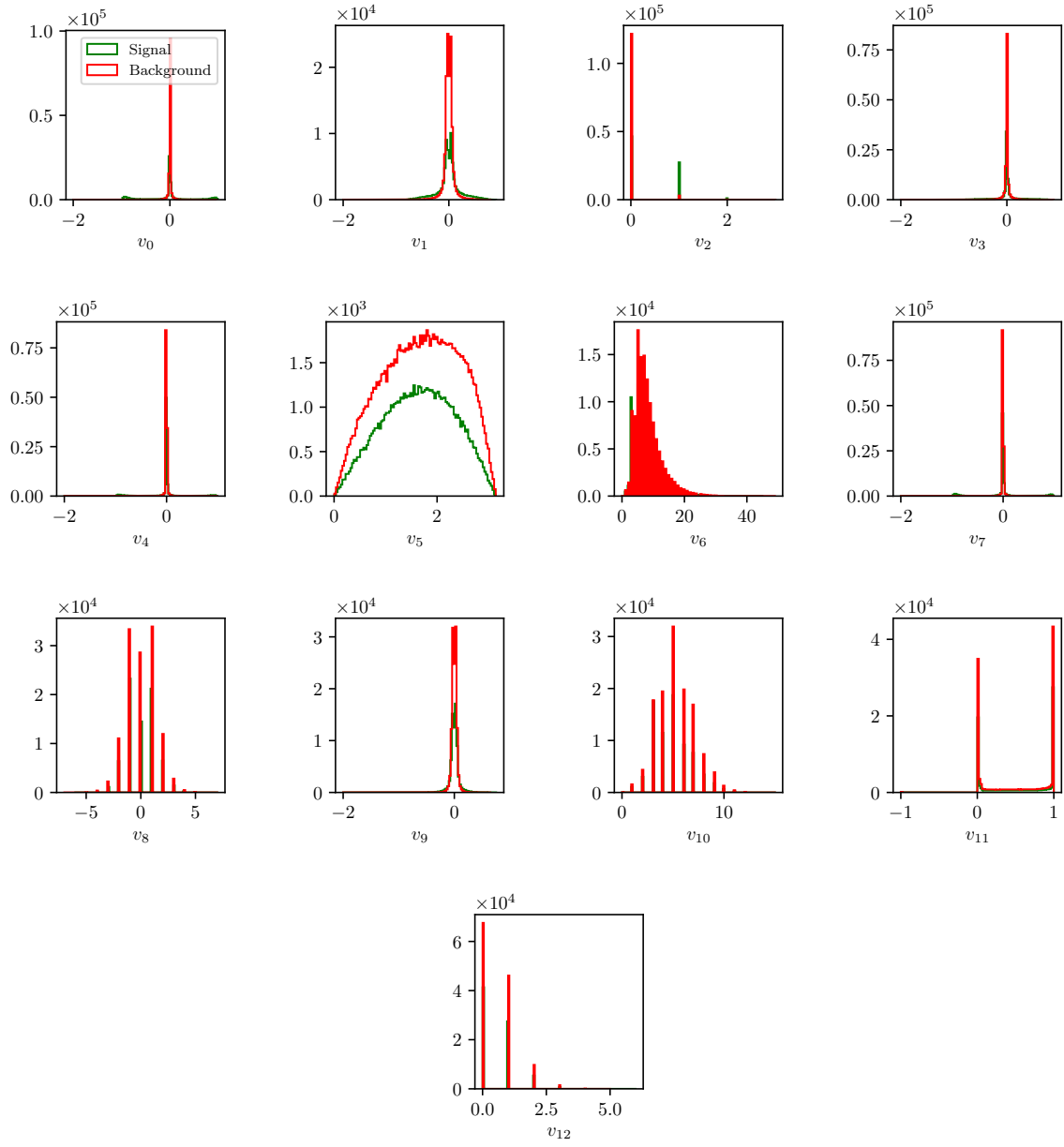


Figure 8.1: Feature distributions for MVA training of hadronically decayed candidates.

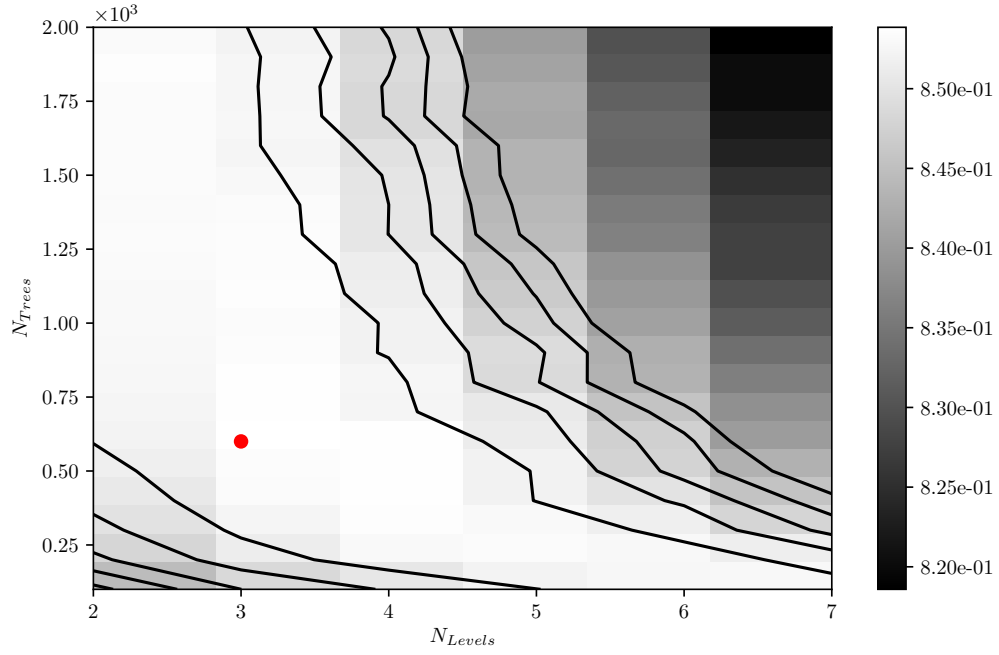


Figure 8.2: Hyper-parameter optimization of `nTrees` and `nLevels` in the BDT forest training of hadronically decayed candidates.

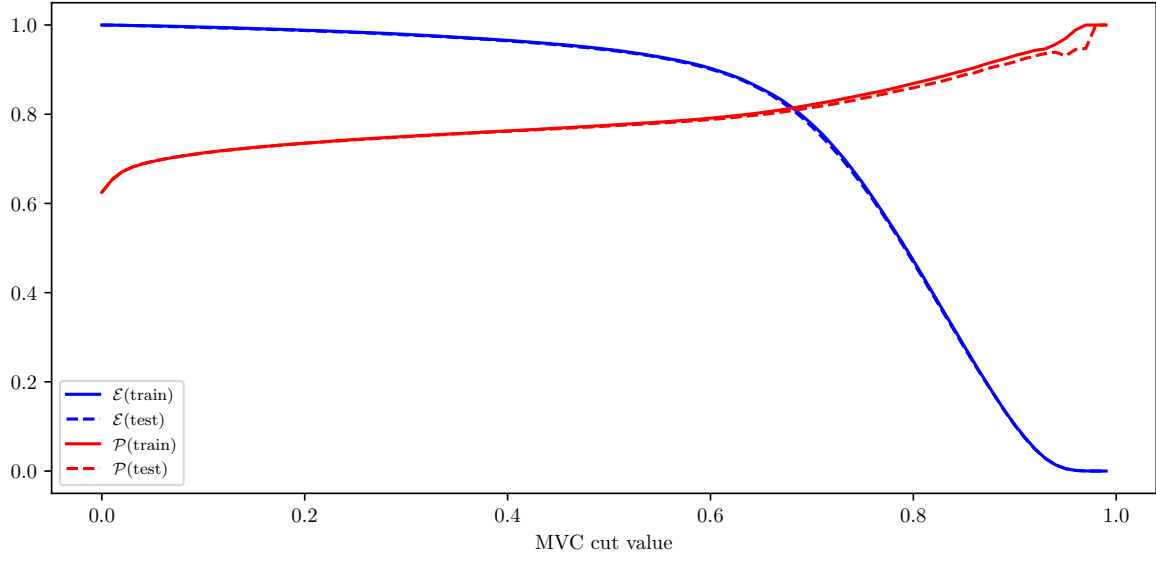


Figure 8.3: Efficiency (\mathcal{E}) and purity (\mathcal{P}) of the MVA classifier output for hadronically decayed candidates training on the train (solid) and test (dashed) samples.

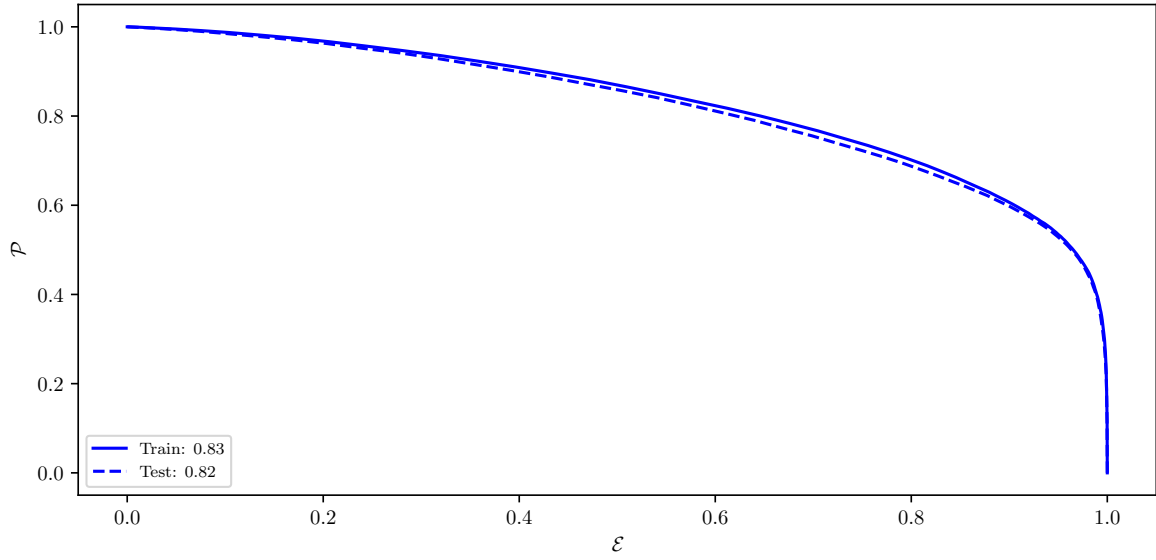


Figure 8.4: ROC curves of the MVA classifier output for hadronically decayed candidates training on the train (solid) and test (dashed) samples.

1345 **ROE clean-up π^0 training**

1346 **Variable importance**

	Name	Alias	Importance
0	chiProb	v_0	0.262
1	useCMSFrame(daughterAngleInBetween(0,1))	v_1	0.148
2	daughter(0,useCMSFrame(p))	v_2	0.079
3	InvM	v_3	0.076
4	daughter(1,clusterHighestE)	v_4	0.062
5	daughter(1,p)	v_5	0.050
6	daughter(1,clusterTheta)	v_6	0.048
7	daughter(0,clusterHighestE)	v_7	0.031
8	daughter(0,clusterTheta)	v_8	0.028
9	daughter(0,minC2HDist)	v_9	0.023
10	daughter(1,minC2HDist)	v_{10}	0.021
11	daughter(0,clusterE9E25)	v_{11}	0.021
12	daughter(1,clusterE9E25)	v_{12}	0.021
13	useRestFrame(daughterAngleInBetween(0,1))	v_{13}	0.018
14	daughter(1,clusterNHits)	v_{14}	0.013
15	SigMBF	v_{15}	0.013
16	daughter(0,clusterNHits)	v_{16}	0.013
17	useCMSFrame(p)	v_{17}	0.012
18	daughter(0,clusterErrorE)	v_{18}	0.011
19	useLabFrame(daughterAngleInBetween(0,1))	v_{19}	0.010
20	daughter(1,clusterErrorE)	v_{20}	0.010
21	daughter(1,useCMSFrame(p))	v_{21}	0.008
22	daughter(0,p)	v_{22}	0.007
23	p	v_{23}	0.007
24	SigM	v_{24}	0.007

Table 8.2: Variable names, aliases and importance in the scope of π^0 MVA training for ROE clean-up.

Variable distributions

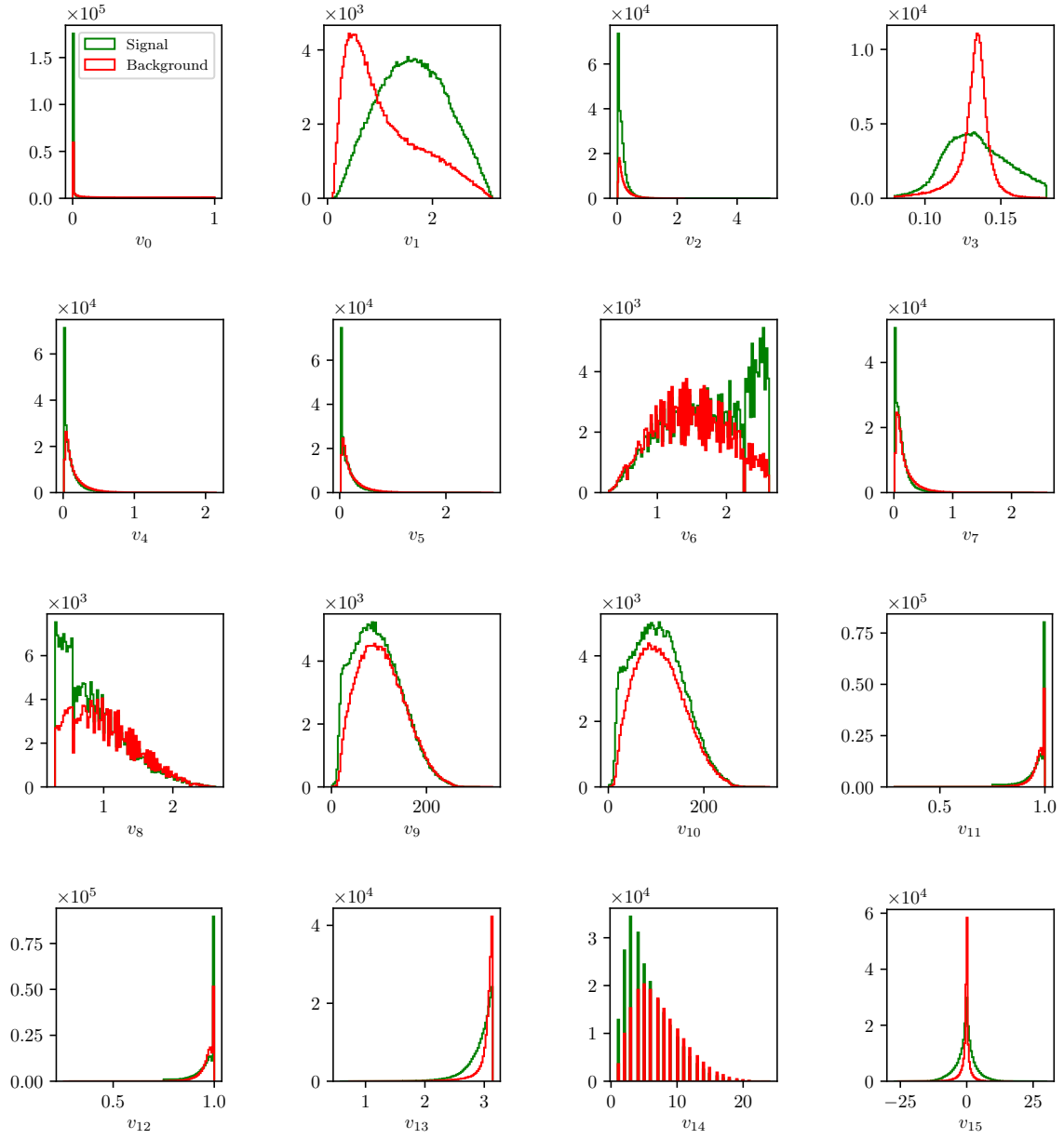


Figure 8.5: Feature distributions for MVA training of π^0 candidates in the scope of ROE clean-up.

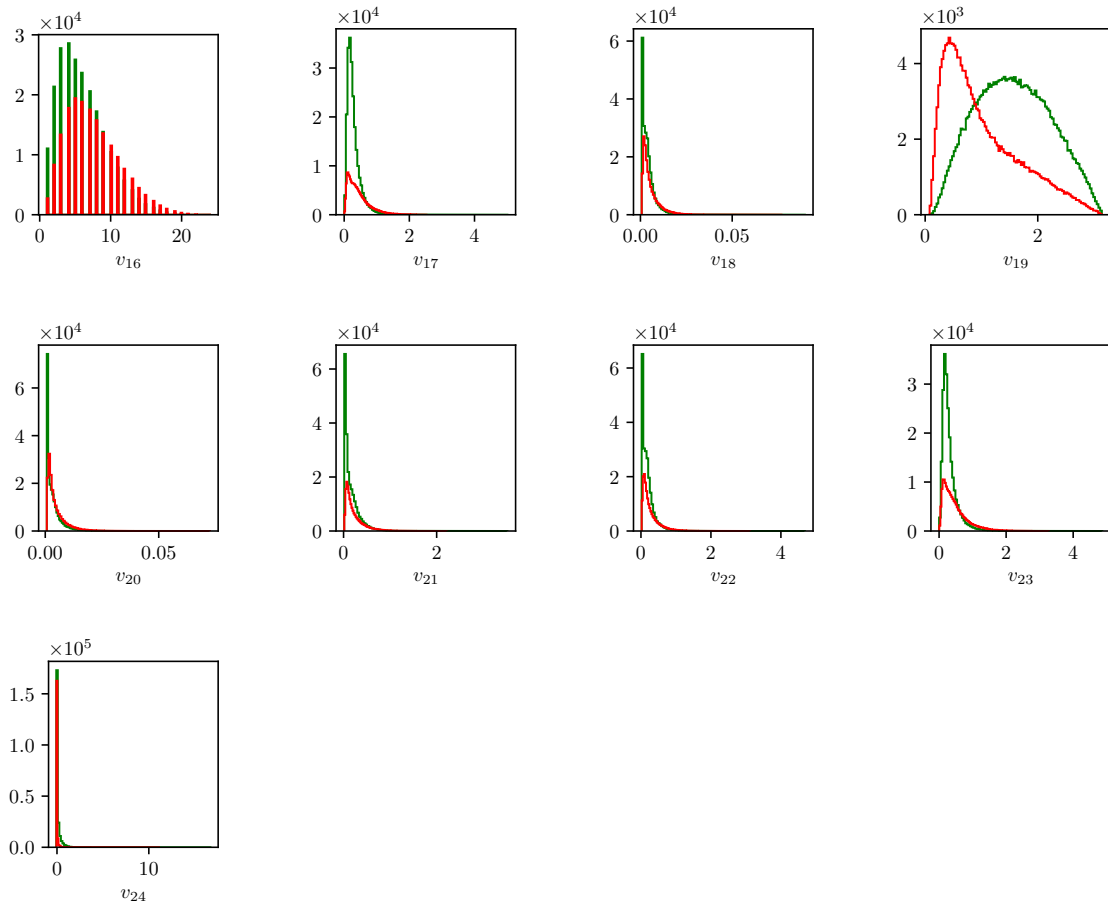


Figure 8.5: Feature distributions for MVA training of π^0 candidates in the scope of ROE clean-up.

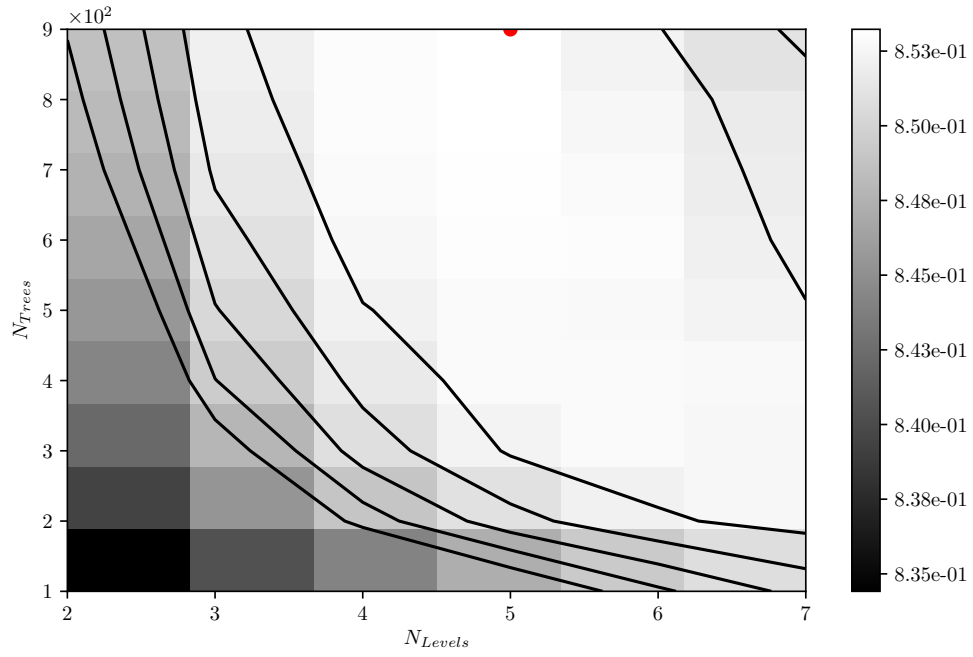


Figure 8.6: Hyper-parameter optimization of **nTrees** and **nLevels** in the BDT forest training of π^0 candidates in the scope of the ROE clean-up.

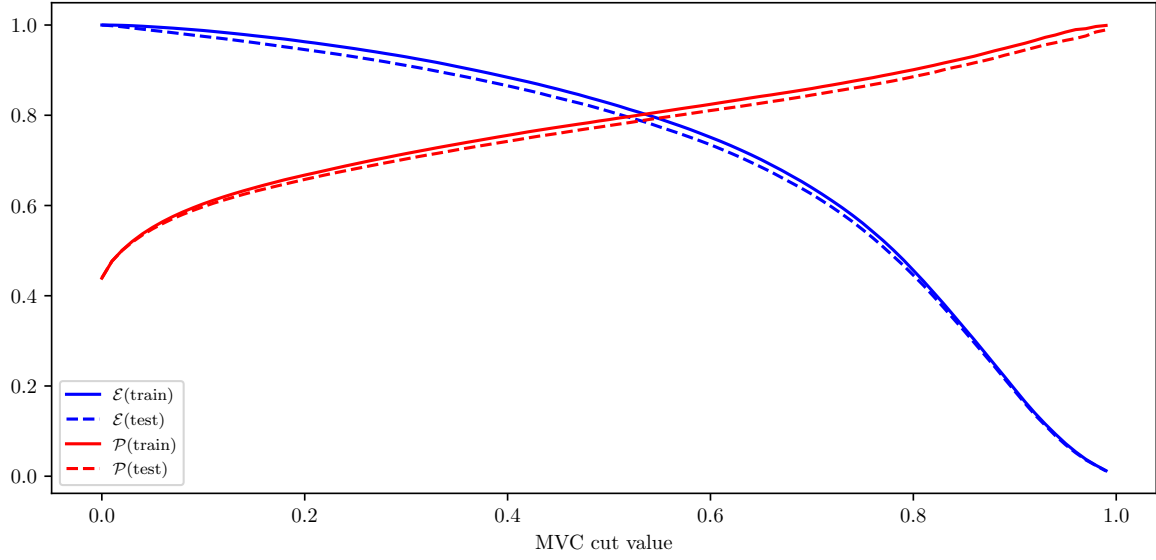


Figure 8.7: Efficiency (\mathcal{E}) and purity (\mathcal{P}) of the MVA classifier output for π^0 candidates training on the train (solid) and test (dashed) samples.

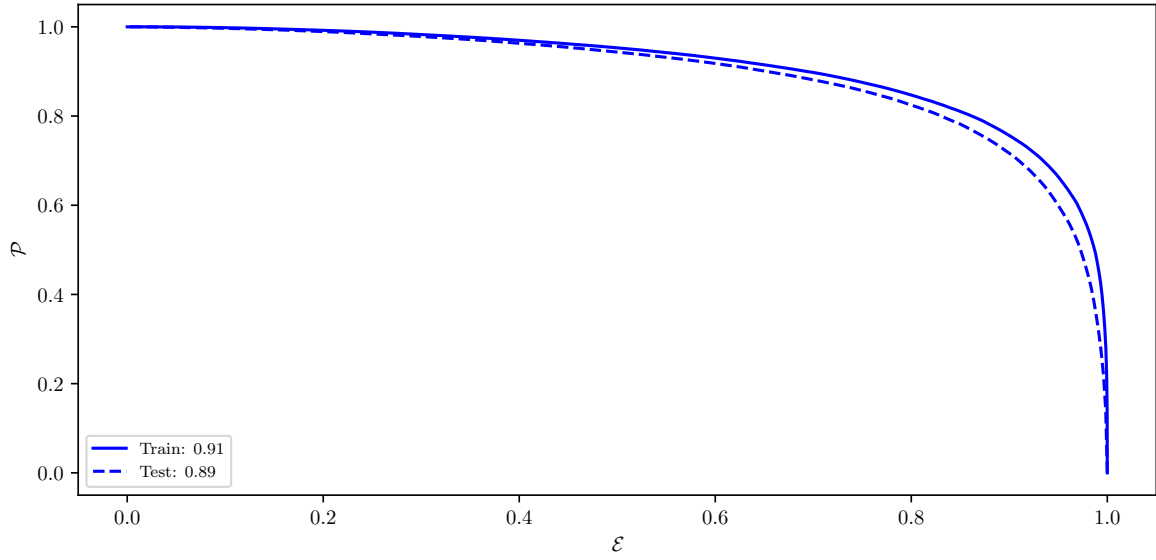


Figure 8.8: ROC curves of the MVA classifier output for π^0 candidates training on the train (solid) and test (dashed) samples.

1350

ROE clean-up γ training

1351

Variable importance

	Name	Alias	Importance
0	p	v_0	0.317
1	clusterHighestE	v_1	0.251
2	pi0p	v_2	0.183
3	minC2HDist	v_3	0.058
4	cosTheta	v_4	0.044
5	clusterNHits	v_5	0.031
6	clusterE9E25	v_6	0.030
7	useCMSFrame(p)	v_7	0.028
8	clusterUncorrE	v_8	0.023
9	clusterR	v_9	0.019
10	clusterErrorE	v_{10}	0.011
11	clusterReg	v_{11}	0.006

Table 8.3: Variable names, aliases and importance in the scope of γ MVA training for ROE clean-up.

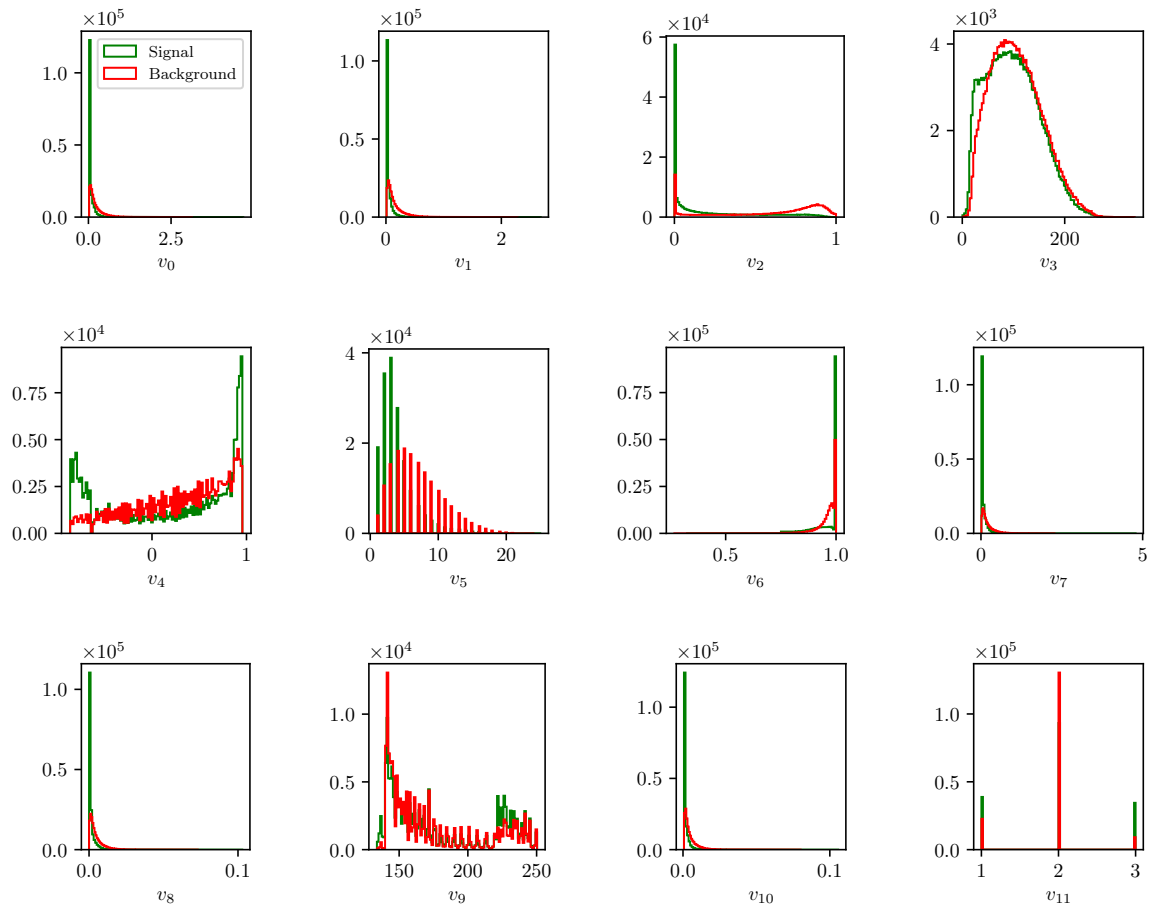


Figure 8.9: Feature distributions for MVA training of γ candidates in the scope of ROE clean-up.

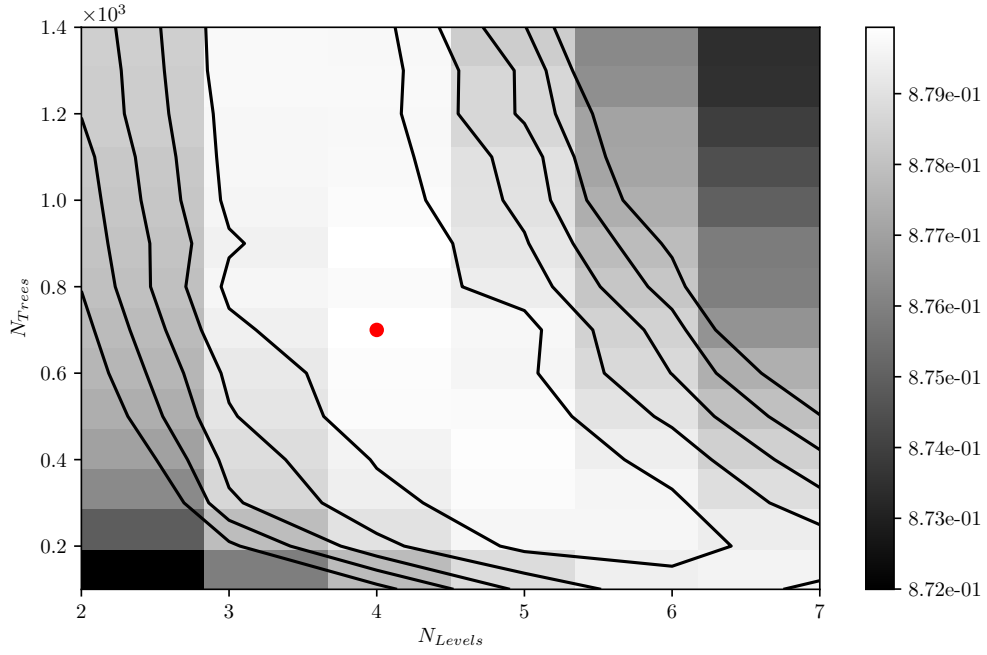


Figure 8.10: Hyper-parameter optimization of **nTrees** and **nLevels** in the BDT forest training of γ candidates in the scope of the ROE clean-up.

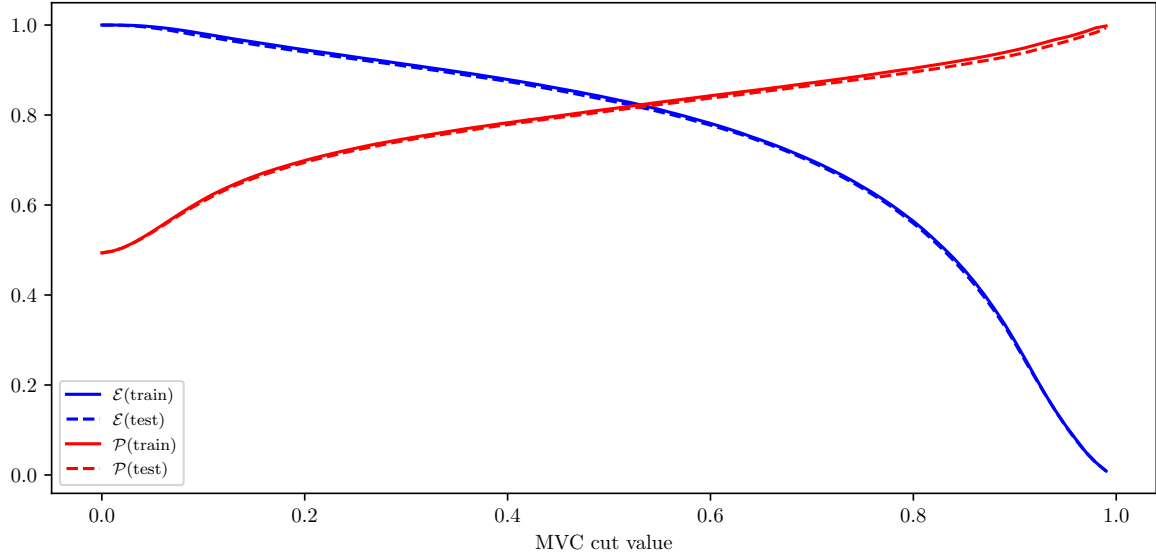


Figure 8.11: Efficiency (\mathcal{E}) and purity (\mathcal{P}) of the MVA classifier output for γ candidates training on the train (solid) and test (dashed) samples.

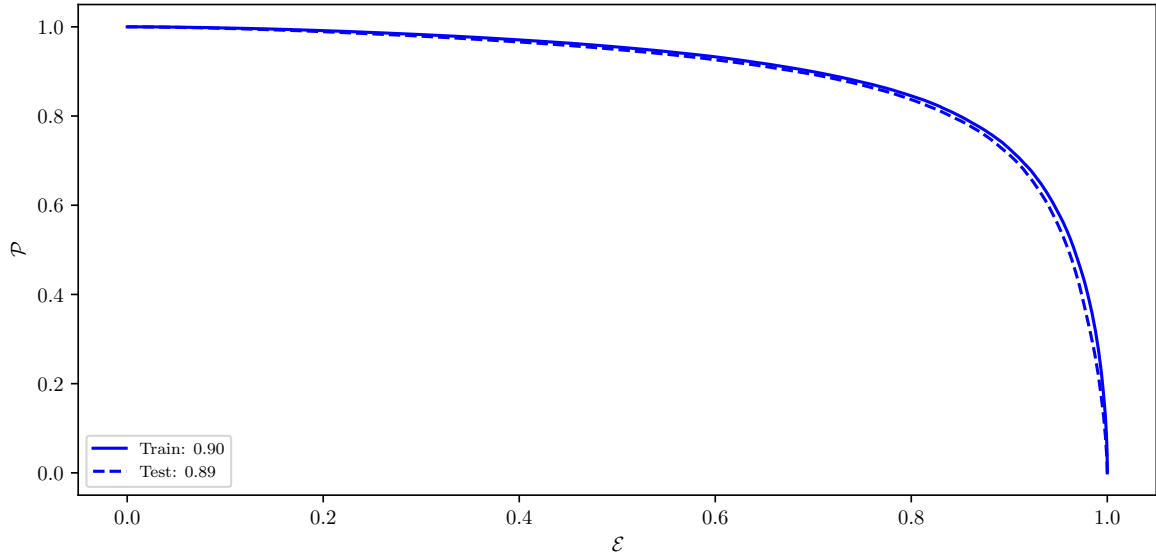


Figure 8.12: ROC curves of the MVA classifier output for γ candidates training on the train (solid) and test (dashed) samples.

ROE clean-up duplicate pair training

Variable importance

	Name	Alias	Importance
0	useCMSFrame(daughterAngleInBetween(0,1))	v_0	0.140
1	daughter(1,d0Err)	v_1	0.084
2	useLabFrame(daughterAngleInBetween(0,1))	v_2	0.056
3	daughter(1,d0)	v_3	0.048
4	daughter(0,d0)	v_4	0.047
5	daughter(0,nSVDHits)	v_5	0.045
6	daughter(1,phi0Err)	v_6	0.042
7	daughter(1,nCDCHits)	v_7	0.038
8	daughter(1,z0)	v_8	0.035
9	daughter(0,nCDCHits)	v_9	0.032
10	daughter(0,z0)	v_{10}	0.030
11	daughter(1,useCMSFrame(p))	v_{11}	0.030
12	daughter(1,pz)	v_{12}	0.026
13	extraInfo(decayModeID)	v_{13}	0.026
14	daughter(0,pz)	v_{14}	0.022
15	daughter(0,pValue)	v_{15}	0.021
16	daughter(1,tanlambda)	v_{16}	0.021
17	daughter(0,d0Err)	v_{17}	0.020
18	daughter(1,pValue)	v_{18}	0.019
19	daughter(0,phi0Err)	v_{19}	0.018
20	daughter(0,useCMSFrame(p))	v_{20}	0.018
21	daughter(0,tanlambda)	v_{21}	0.017
22	daughter(0,phi0)	v_{22}	0.017
23	daughter(1,phi0)	v_{23}	0.016
24	daughter(0,z0Err)	v_{24}	0.014
25	daughter(1,omega)	v_{25}	0.014
26	daughter(0,omega)	v_{26}	0.013
27	daughter(1,z0Err)	v_{27}	0.013
28	daughter(0,pt)	v_{28}	0.012
29	daughter(0,omegaErr)	v_{29}	0.012
30	daughter(1,pt)	v_{30}	0.011

31	daughter(1,omegaErr)	v_{31}	0.011
32	daughter(0,tanlambdaErr)	v_{32}	0.010
33	daughter(1,nSVDHits)	v_{33}	0.010
34	daughter(1,tanlambdaErr)	v_{34}	0.009
35	useRestFrame(daughterAngleInBetween(0,1))	v_{35}	0.002
36	daughter(1,charge)	v_{36}	0.000
37	daughter(0,charge)	v_{37}	0.000

Table 8.4: Variable names, aliases and importance in the scope of duplicate track pair MVA training for ROE clean-up.

Variable distributions

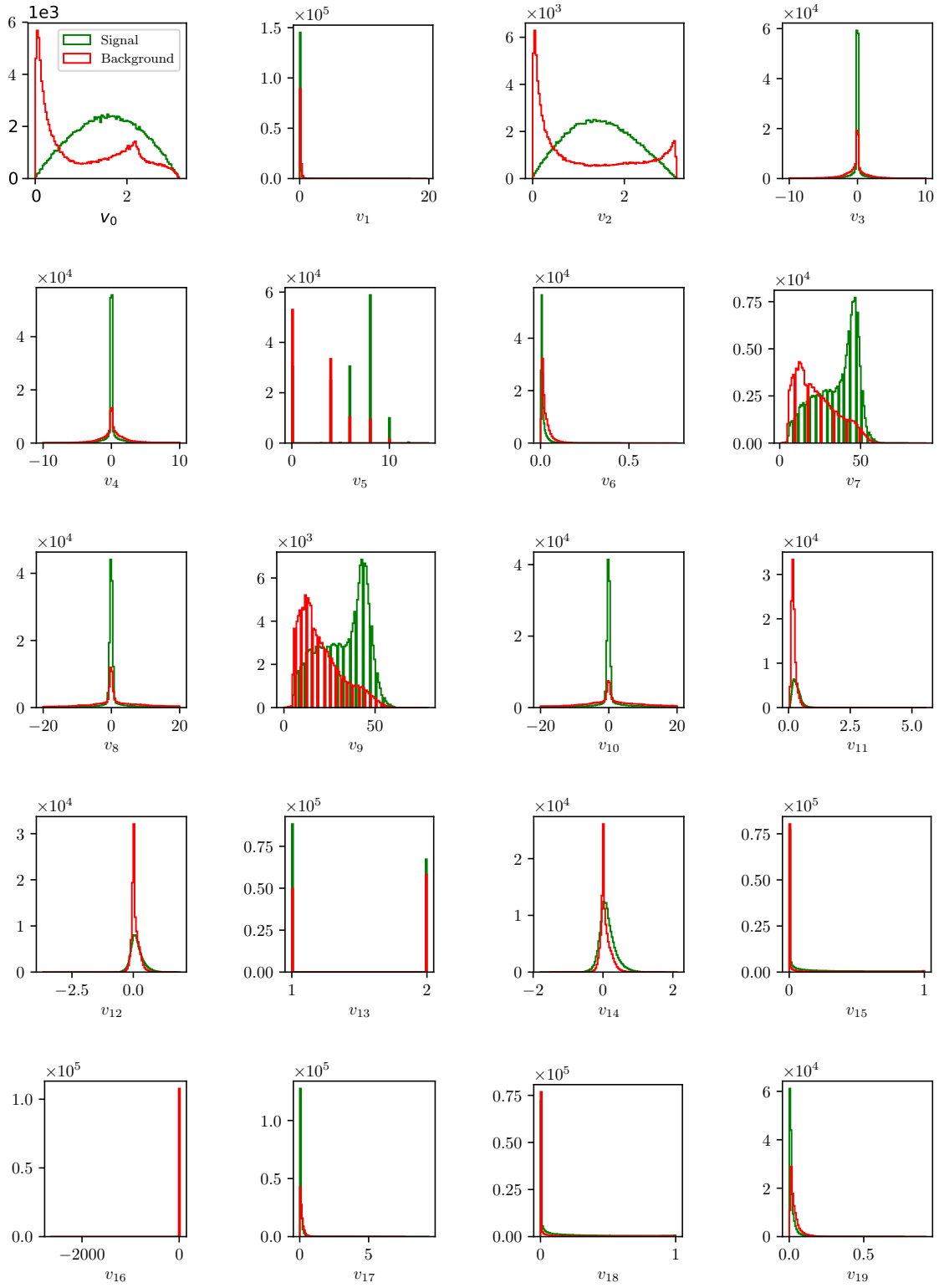


Figure 8.13: Feature distributions for MVA training of duplicate track pair candidates in the scope of ROE clean-up.

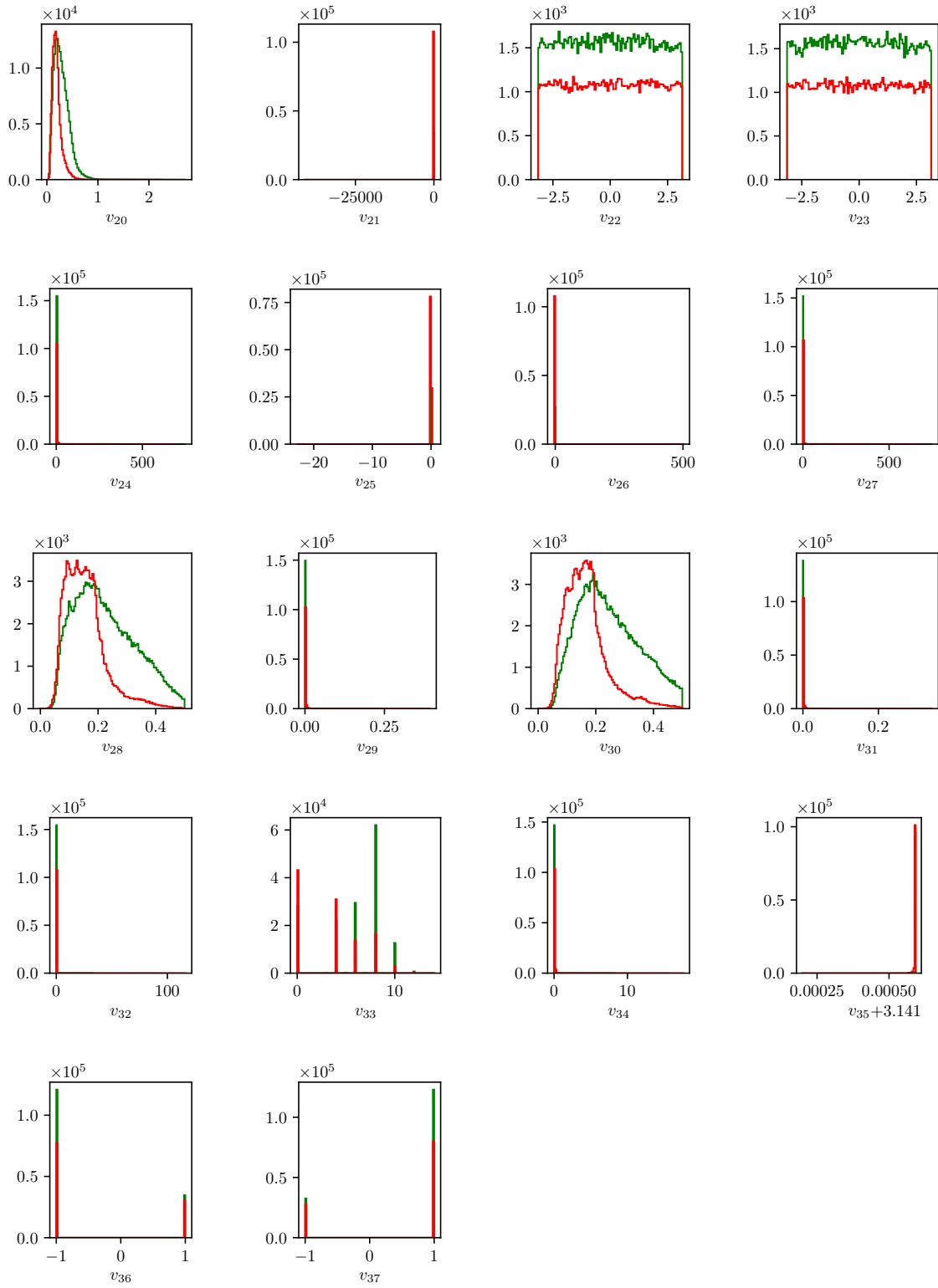


Figure 8.13: Feature distributions for MVA training of duplicate track pair candidates in the scope of ROE clean-up.

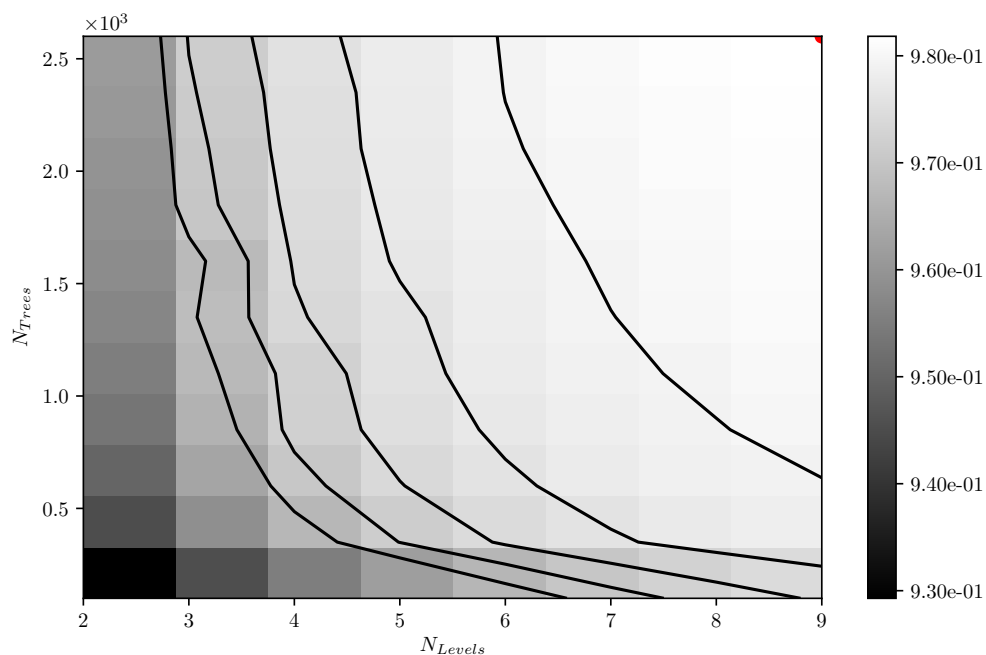


Figure 8.14: Hyper-parameter optimization of **nTrees** and **nLevels** in the BDT forest training of duplicate track pair candidates in the scope of the ROE clean-up.

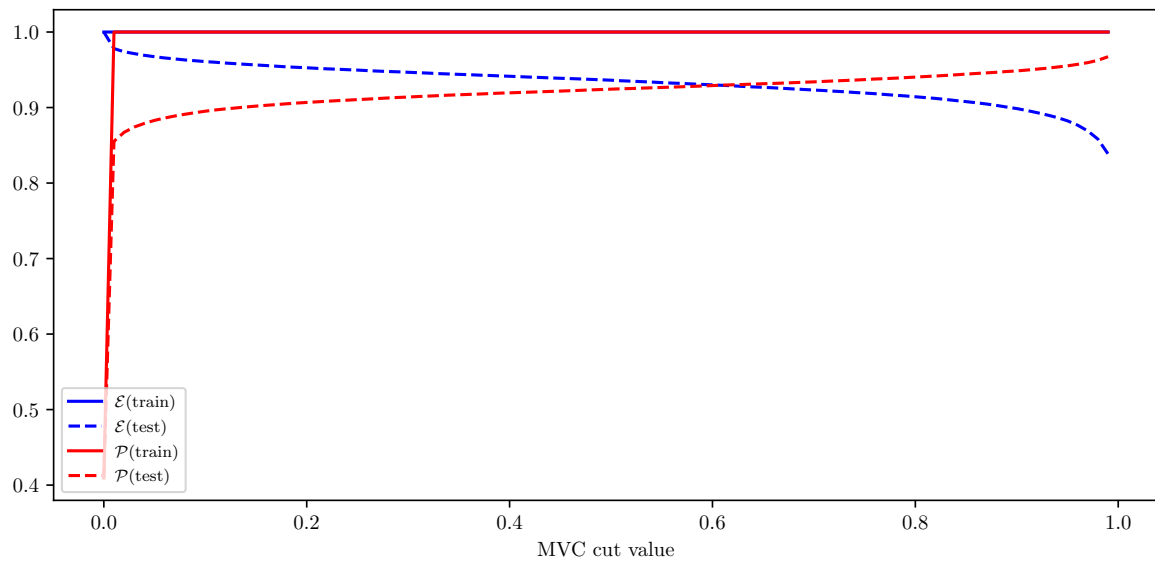


Figure 8.15: Efficiency (\mathcal{E}) and purity (\mathcal{P}) of the MVA classifier output for duplicate track pair candidates training on the train (solid) and test (dashed) samples.

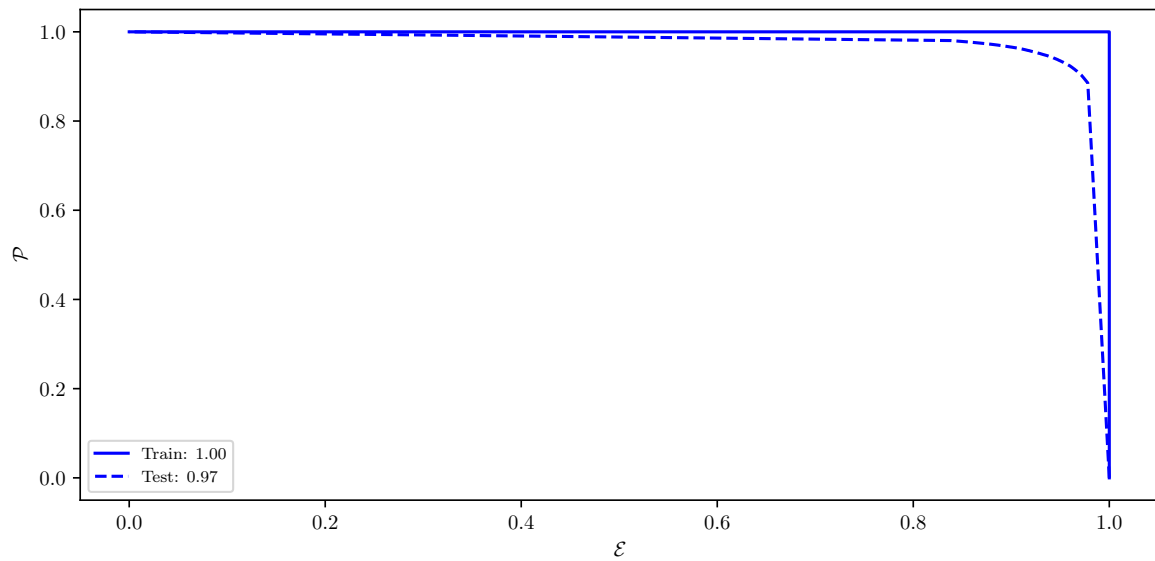


Figure 8.16: ROC curves of the MVA classifier output for duplicate track pair candidates training on the train (solid) and test (dashed) samples.

ROE clean-up duplicate track training

Variable importance

	Name	Alias	Importance
0	d0	v_0	0.093
1	extraInfo(nSVDHitsDiff)	v_1	0.089
2	z0	v_2	0.080
3	extraInfo(pValueDiff)	v_3	0.060
4	extraInfo(ptDiff)	v_4	0.059
5	extraInfo(z0Diff)	v_5	0.055
6	extraInfo(phi0Diff)	v_6	0.046
7	extraInfo(pzDiff)	v_7	0.045
8	extraInfo(nCDCHitsDiff)	v_8	0.043
9	phi0Err	v_9	0.042
10	extraInfo(tanlambdaDiff)	v_{10}	0.039
11	z0Err	v_{11}	0.035
12	pValue	v_{12}	0.030
13	extraInfo(omegaDiff)	v_{13}	0.030
14	tanlambdaErr	v_{14}	0.029
15	nCDCHits	v_{15}	0.028
16	pt	v_{16}	0.027
17	d0Err	v_{17}	0.025
18	phi0	v_{18}	0.025
19	pz	v_{19}	0.024
20	cosTheta	v_{20}	0.022
21	omegaErr	v_{21}	0.022
22	useCMSFrame(p)	v_{22}	0.021
23	omega	v_{23}	0.018
24	nSVDHits	v_{24}	0.014

Table 8.5: Variable names, aliases and importance in the scope of duplicate track MVA training for ROE clean-up.

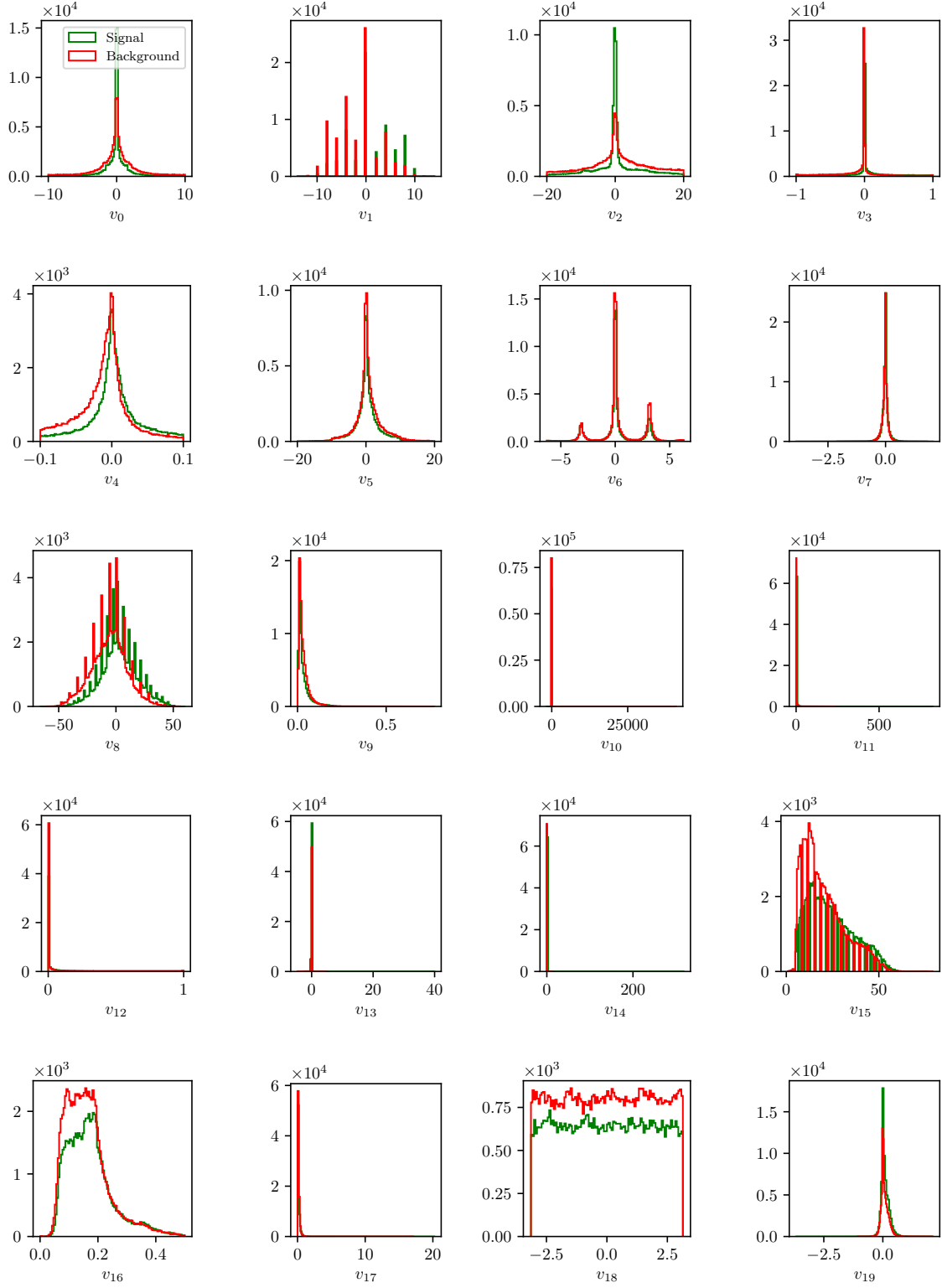


Figure 8.17: Feature distributions for MVA training of duplicate track candidates in the scope of ROE clean-up.

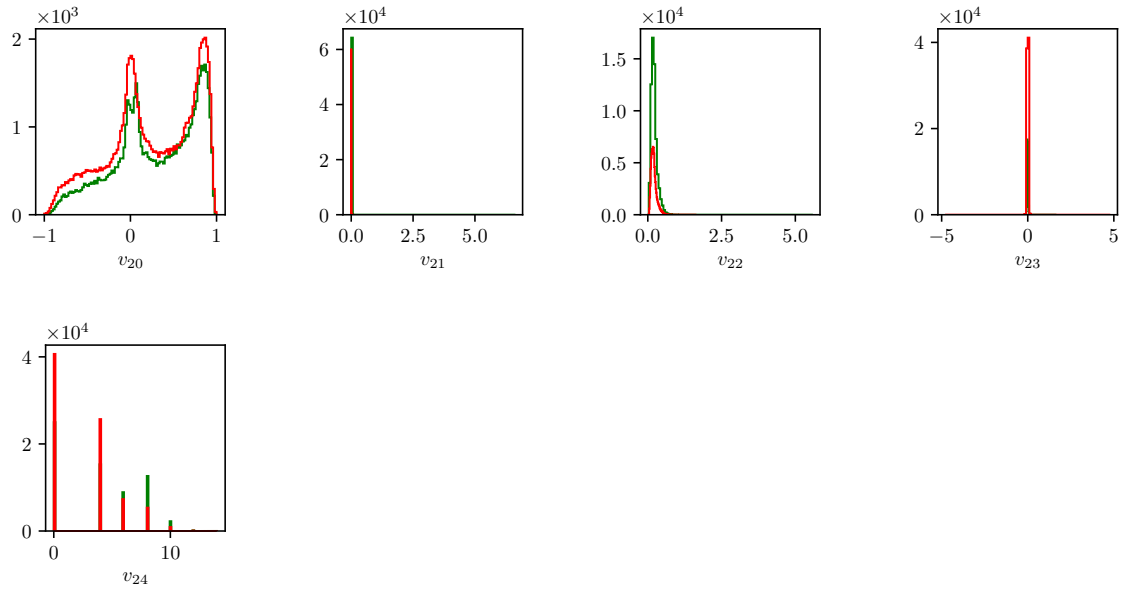


Figure 8.17: Feature distributions for MVA training of duplicate track candidates in the scope of ROE clean-up.

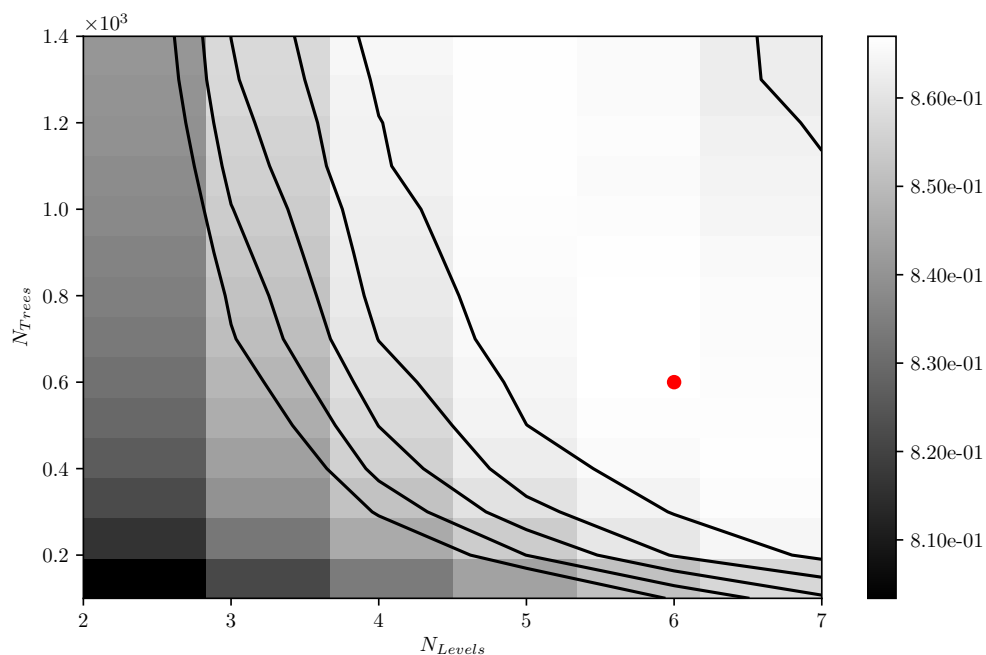


Figure 8.18: Hyper-parameter optimization of **nTrees** and **nLevels** in the BDT forest training of duplicate track candidates in the scope of the ROE clean-up.

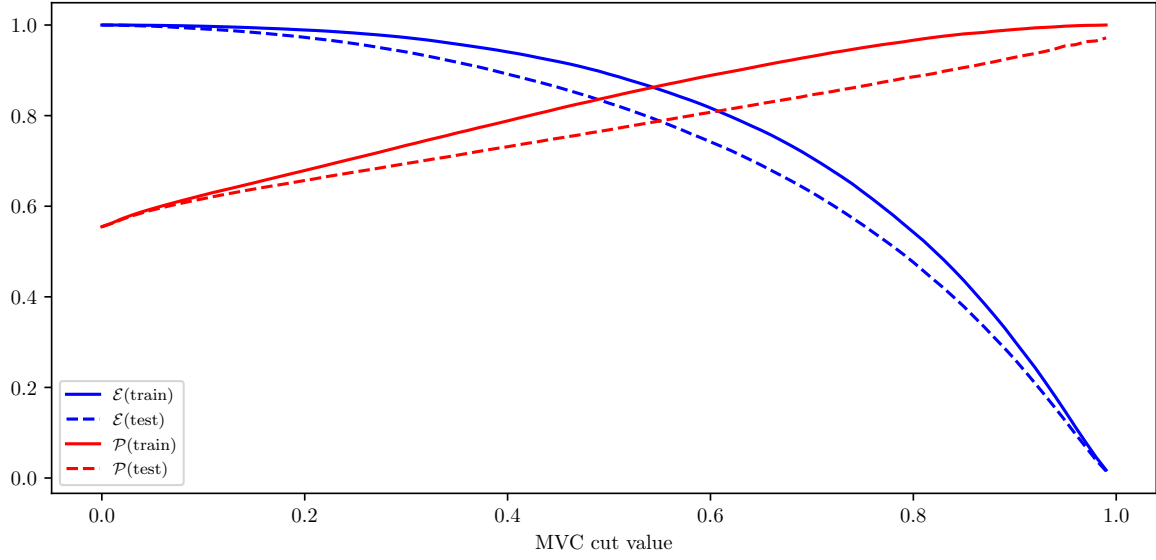


Figure 8.19: Efficiency (\mathcal{E}) and purity (\mathcal{P}) of the MVA classifier output for duplicate track candidates training on the train (solid) and test (dashed) samples.

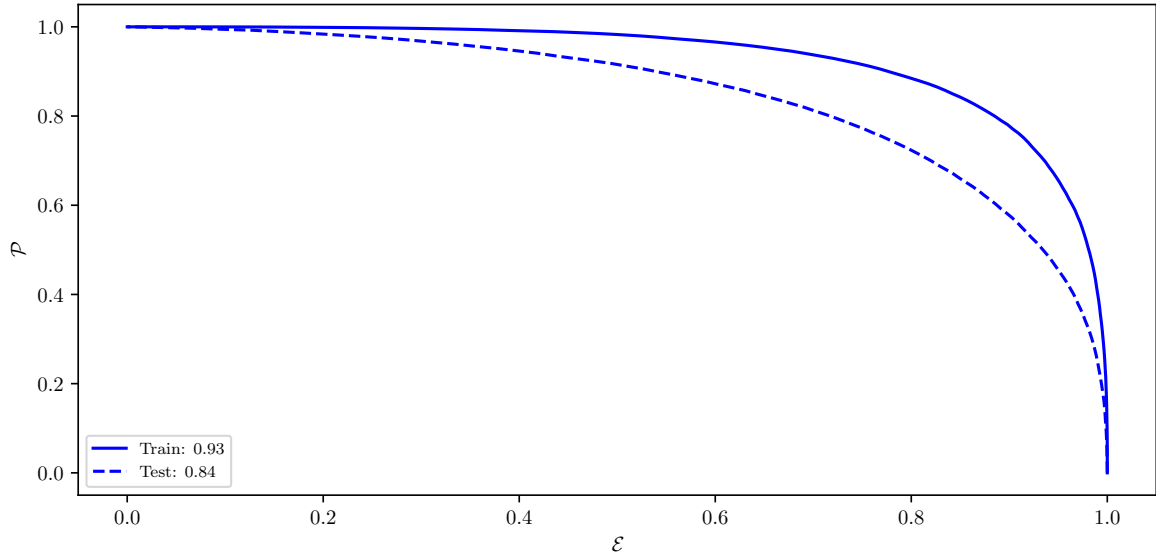


Figure 8.20: ROC curves of the MVA classifier output for duplicate track candidates training on the train (solid) and test (dashed) samples.

1365 $q\bar{q}$ suppression training

1366 Variable importance

	Name	Alias	Importance
0	B_R2	v_0	0.275
1	B_CosTBT0	v_1	0.162
2	B_ThrustB	v_2	0.066
3	B_roeFit_dz	v_3	0.056
4	B_hso02	v_4	0.056
5	B_Thrust0	v_5	0.035
6	B_hoo2	v_6	0.034
7	B_hso12	v_7	0.025
8	B_qpFastHadron	v_8	0.020
9	B_hoo0	v_9	0.018
10	B_cc2_CcROE	v_{10}	0.018
11	B_CosTBz	v_{11}	0.017
12	B_qpKaon	v_{12}	0.016
13	B_cc3_CcROE	v_{13}	0.016
14	B_hso01	v_{14}	0.016
15	B_cc4_CcROE	v_{15}	0.015
16	B_qpMaximumPstar	v_{16}	0.014
17	B_cc5_CcROE	v_{17}	0.012
18	B_cc1_CcROE	v_{18}	0.011
19	B_cc6_CcROE	v_{19}	0.011
20	B_cc7_CcROE	v_{20}	0.010
21	B_cc9_CcROE	v_{21}	0.009
22	B_qpSlowPion	v_{22}	0.009
23	B_cc8_CcROE	v_{23}	0.009
24	B_qpFSC	v_{24}	0.009
25	B_qpLambda	v_{25}	0.008
26	B_hoo1	v_{26}	0.008
27	B_qpKaonPion	v_{27}	0.008
28	B_hso10	v_{28}	0.007
29	B_hoo4	v_{29}	0.007
30	B_hso04	v_{30}	0.006

31	B_hso03	v_{31}	0.005
32	B_hoo3	v_{32}	0.005
33	B_hso14	v_{33}	0.005

Table 8.6: Variable names, aliases and importance in the scope of $q\bar{q}$ suppression MVA training.

Variable distributions

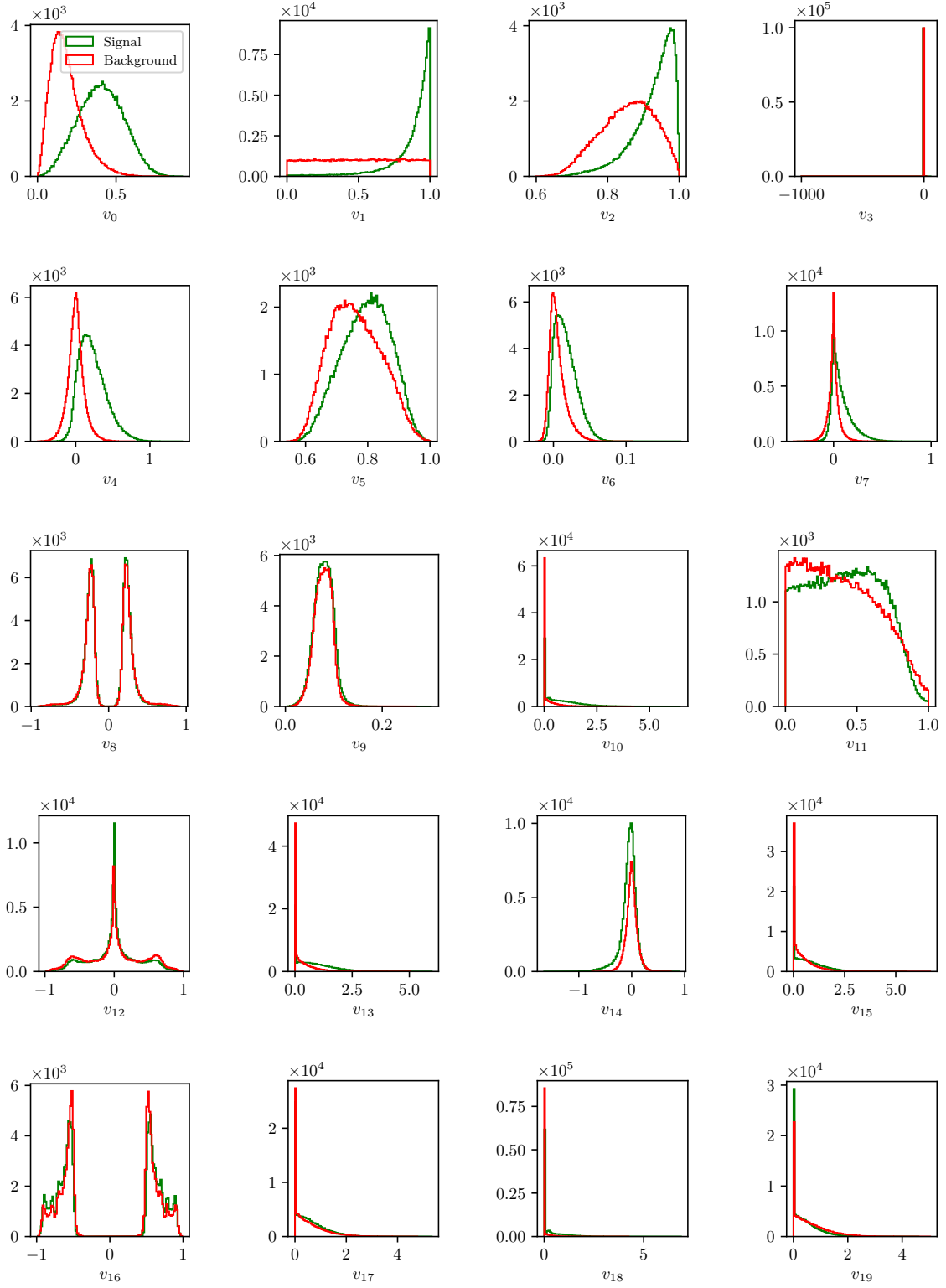


Figure 8.21: Feature distributions for MVA training of $q\bar{q}$ background suppression.

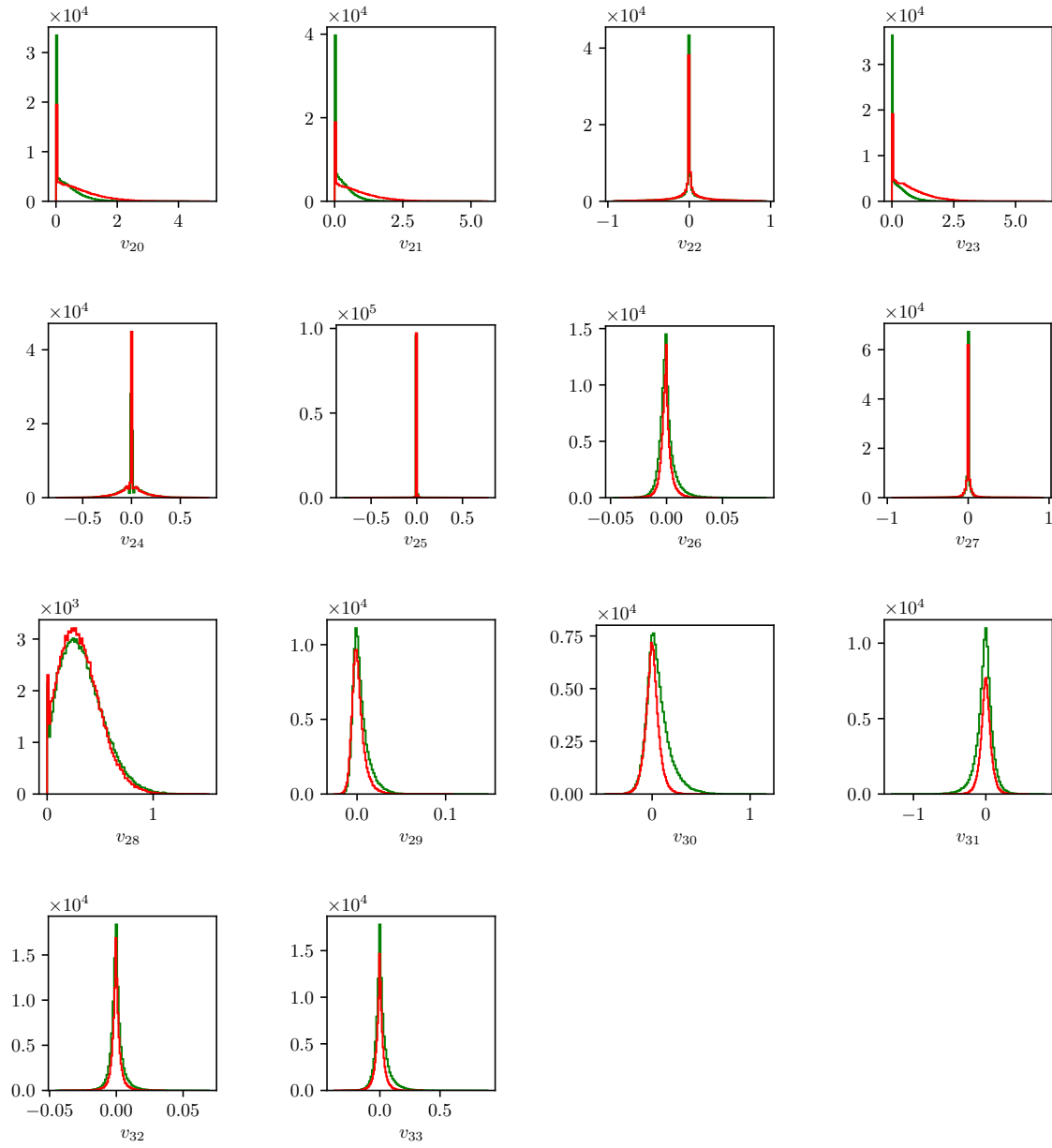


Figure 8.21: Feature distributions for MVA training of $q\bar{q}$ background suppression.

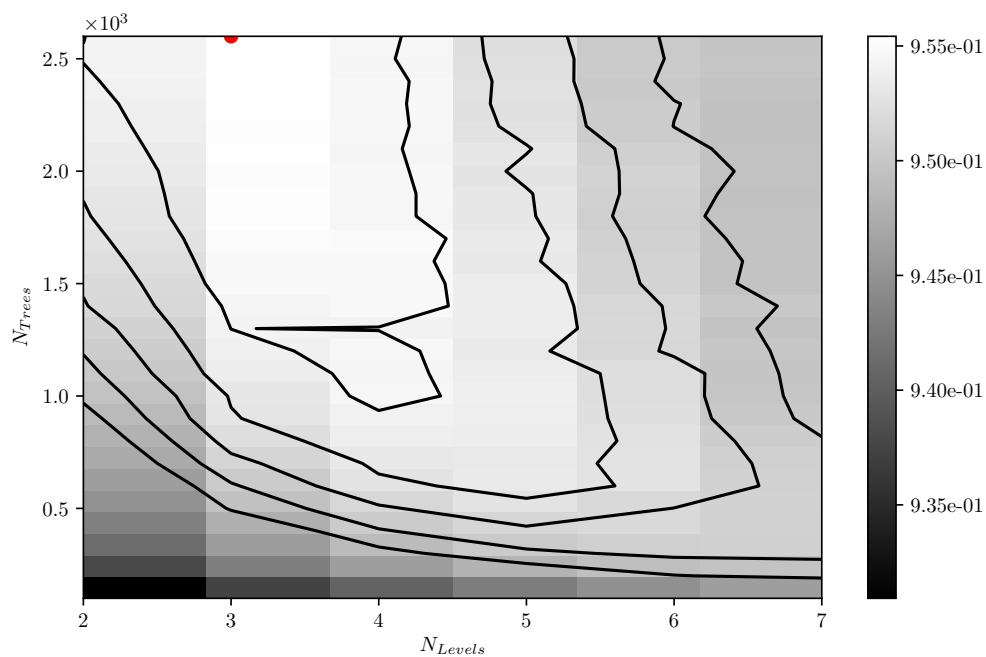


Figure 8.22: Hyper-parameter optimization of **nTrees** and **nLevels** in the BDT forest training of $q\bar{q}$ background suppression.

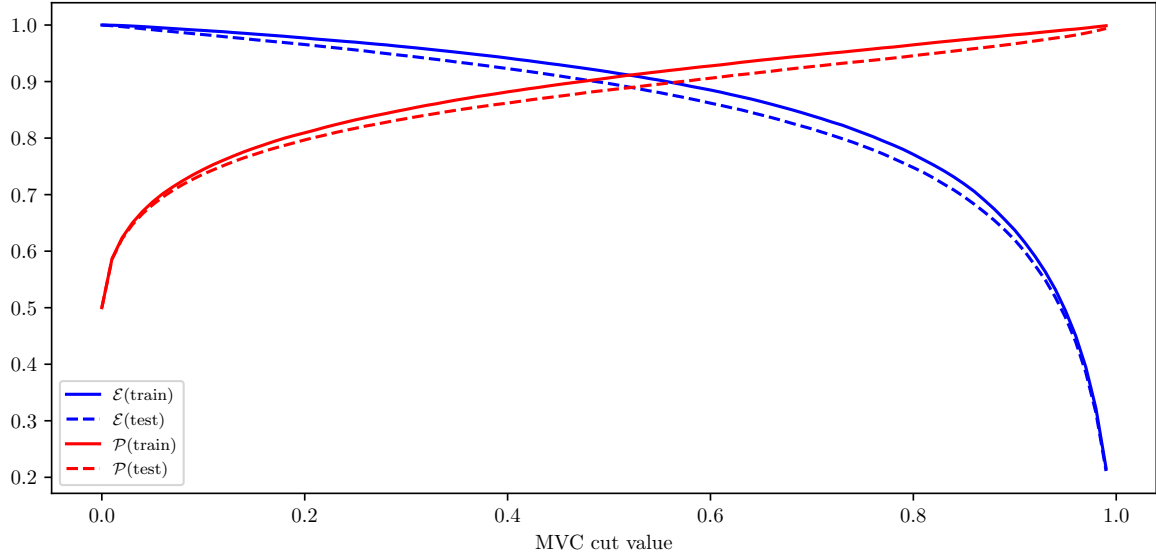


Figure 8.23: Efficiency (\mathcal{E}) and purity (\mathcal{P}) of the MVA classifier output for $q\bar{q}$ background suppression training on the train (solid) and test (dashed) samples.

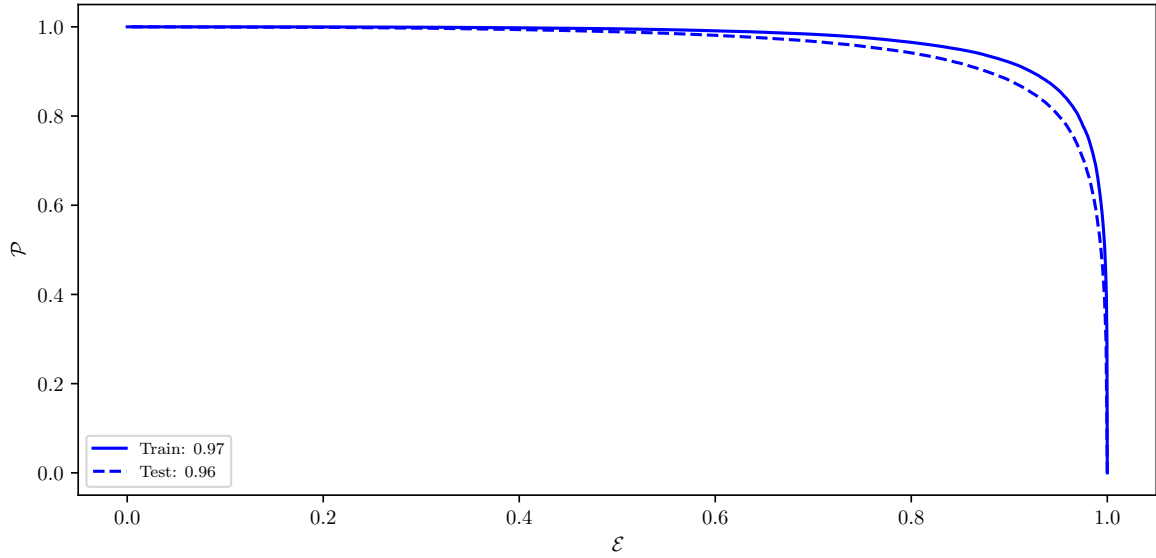


Figure 8.24: ROC curves of the MVA classifier output for $q\bar{q}$ background suppression training on the train (solid) and test (dashed) samples.

1370 **Standard $B\bar{B}$ suppression training**

1371 **Variable importance**

	Name	Alias	Importance
0	B_cosMomVtxKKlnu	v_0	0.412
1	B_ROE_PThetacms0	v_1	0.101
2	B_nROETrk0	v_2	0.067
3	B_K1FT	v_3	0.056
4	B_nROEDistTrk	v_4	0.055
5	B_cosBY	v_5	0.042
6	B_xiZ0	v_6	0.038
7	B_roeFit_dz	v_7	0.034
8	B_cosMomVtx	v_8	0.033
9	B_missM2Veto1	v_9	0.030
10	B_nKaonInROE	v_{10}	0.021
11	B_QVeto1	v_{11}	0.020
12	B_chiProb	v_{12}	0.017
13	B_K0FT	v_{13}	0.016
14	B_TagVPvalue	v_{14}	0.015
15	B_cosMomVtxKK	v_{15}	0.014
16	B_missM20	v_{16}	0.014
17	B_missM2Veto2	v_{17}	0.007
18	B_QVeto2	v_{18}	0.006

Table 8.7: Variable names, aliases and importance in the scope of $B\bar{B}$ background suppression.

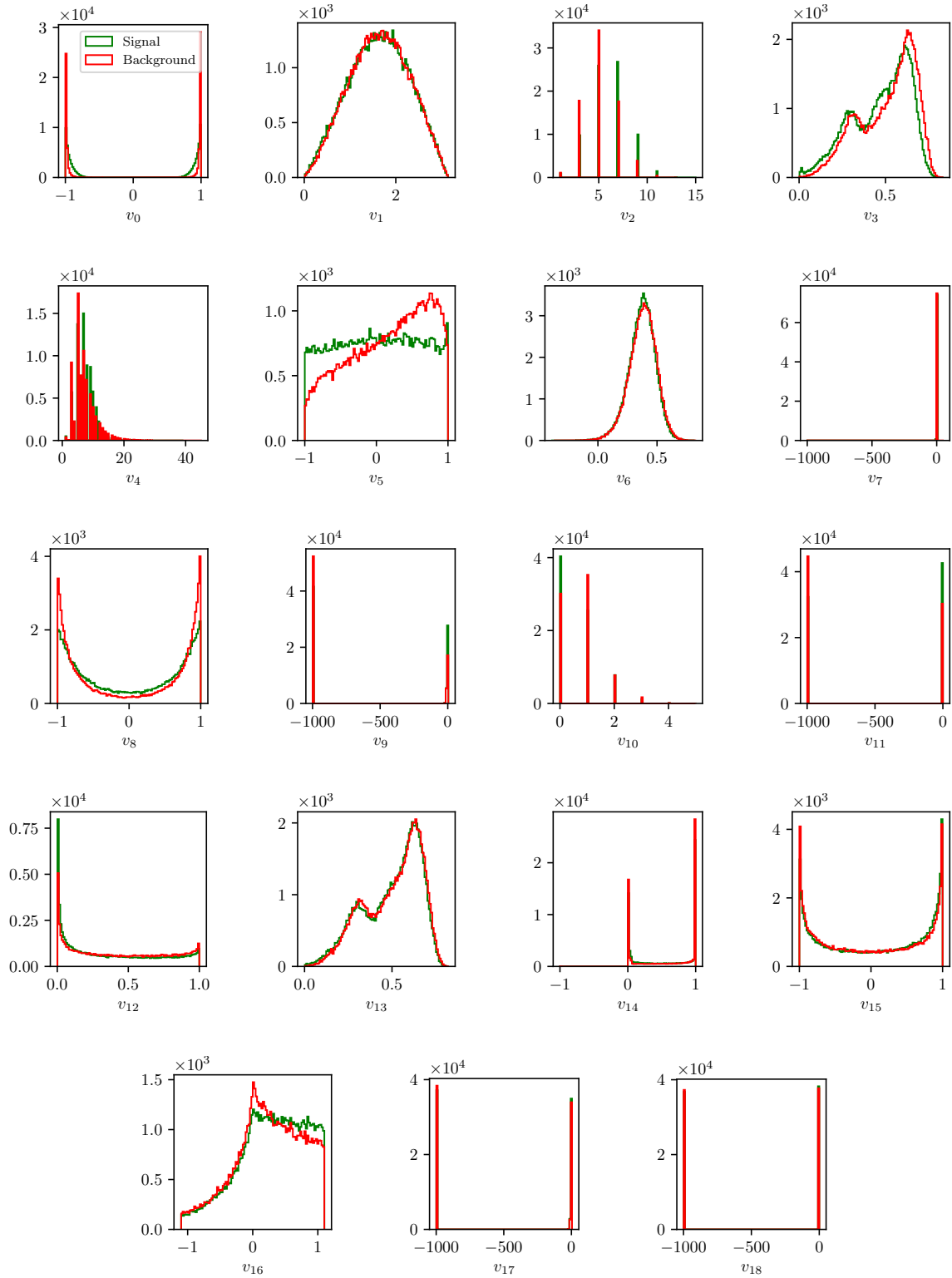


Figure 8.25: Feature distributions for MVA training of $B\bar{B}$ background suppression.

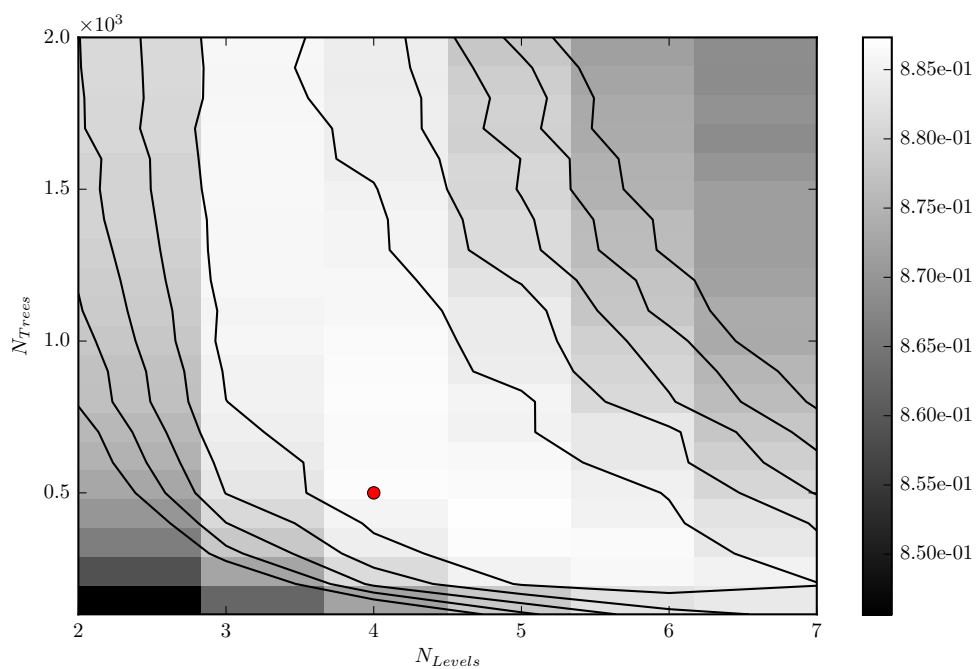


Figure 8.26: Hyper-parameter optimization of **nTrees** and **nLevels** in the BDT forest training of $B\bar{B}$ background suppression.

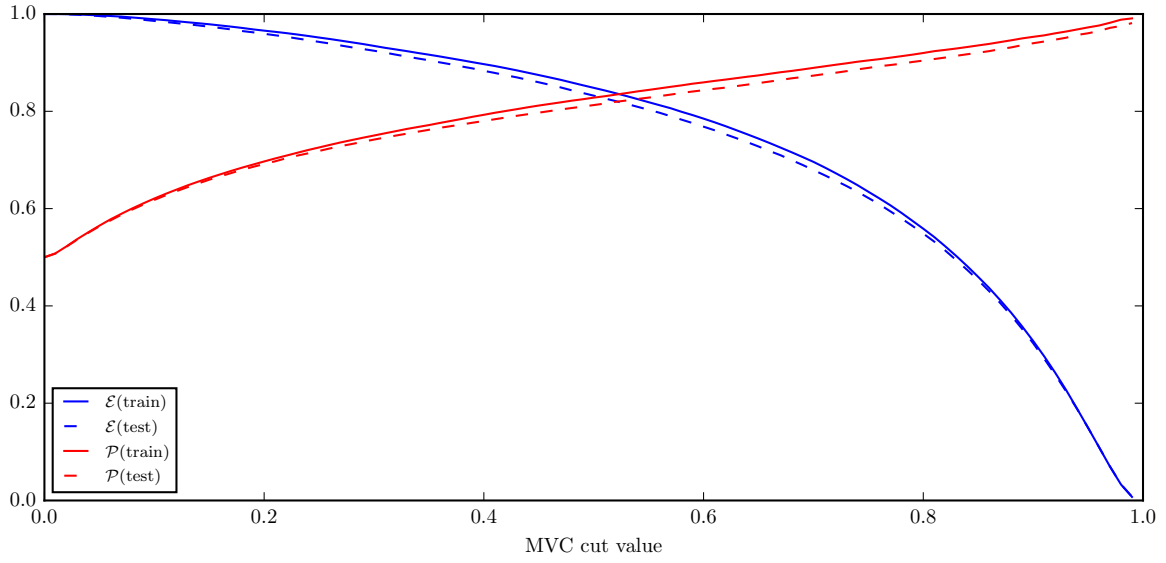


Figure 8.27: Efficiency (\mathcal{E}) and purity (\mathcal{P}) of the MVA classifier output for $B\bar{B}$ background suppression training on the train (solid) and test (dashed) samples.

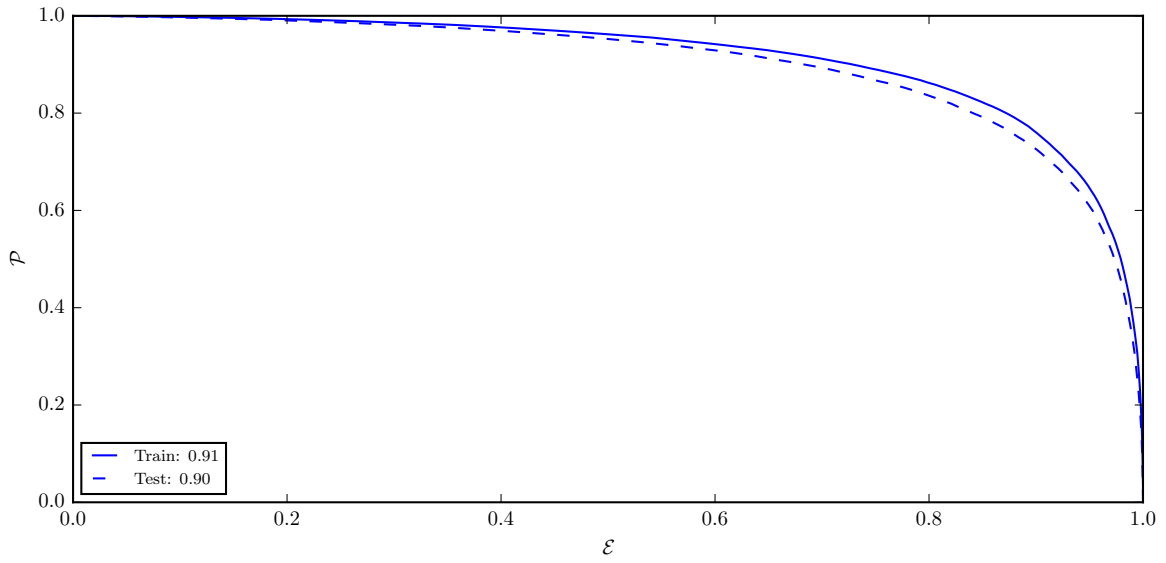


Figure 8.28: ROC curves of the MVA classifier output for $B\bar{B}$ background suppression training on the train (solid) and test (dashed) samples.

Uniformity boosted $B\bar{B}$ suppression training

Hyper-parameter optimization

Hyper-parameters were not optimized due to the large CPU time consumption of the algorithm. The following set up of the hyper-parameters was chosen

- nTrees: 300

- nLevels: 4

Results

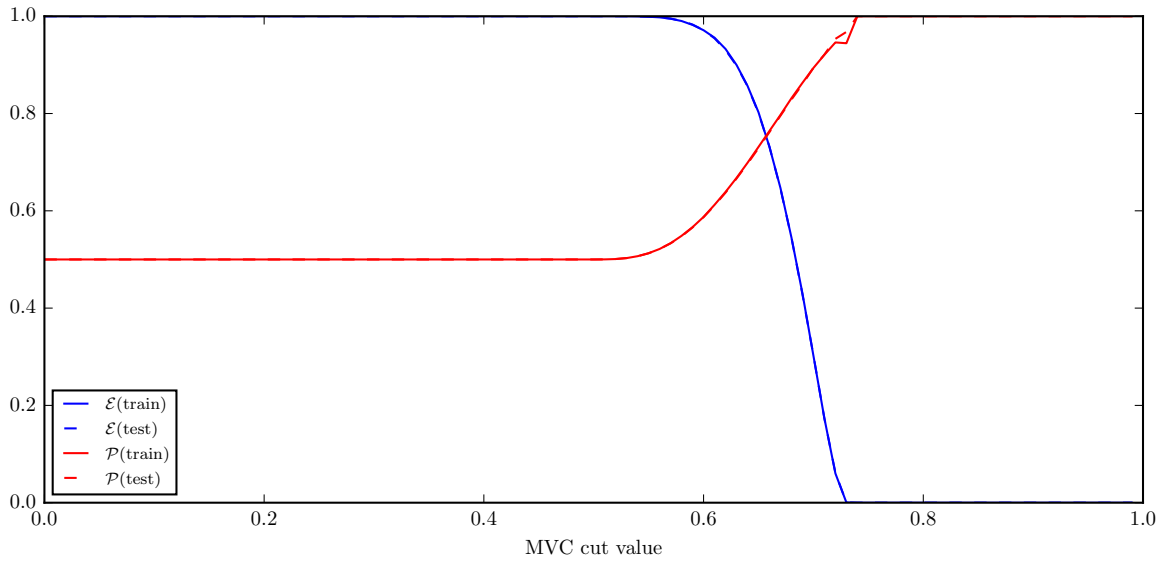


Figure 8.29: Efficiency (\mathcal{E}) and purity (\mathcal{P}) of the uniformity boosted MVA classifier output for $B\bar{B}$ background suppression training on the train (solid) and test (dashed) samples.

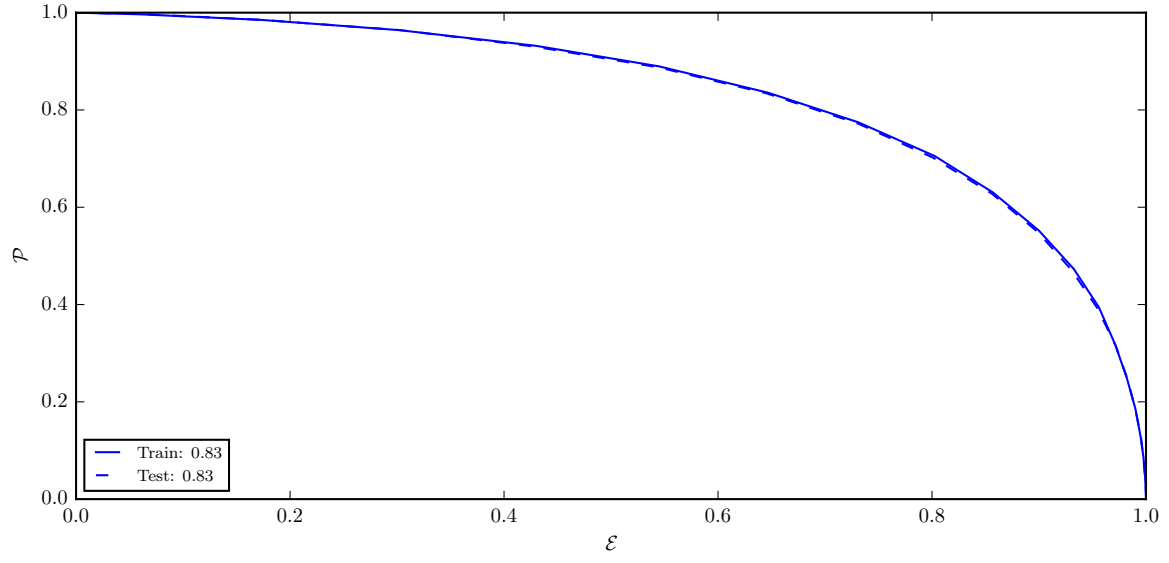


Figure 8.30: ROC curves of the uniformity boosted MVA classifier output for $B\bar{B}$ background suppression training on the train (solid) and test (dashed) samples.